Electronic spectroscopy and computational studies of glutathionylcobalamin, aquocobalamin, and methylcobalamin

By

Iya Likhtina

A dissertation submitted to the Graduate Faculty in Chemistry in partial fulfillment of the requirements of Doctor of Philosophy, The City University of New York

2011

This manuscript has been read and accepted for the Graduate Faculty in Chemistry in satisfaction of the dissertation requirement for the degree of Doctor Philosophy.

Prof. Ronald Birke_____

_____ _____
Date Chair of Examining Committee

Prof. Maria Tamargo_____

_____ _____
Date Executive Officer

Prof. Malgorzata Ciszkowska_____

Prof. John Lombardi _____

Prof. Michael Green _____
Supervisory Committee

THE CITY UNIVERSITY OF NEW YORK

Abstract

Electronic spectroscopy and computational studies of glutathionylcobalamin, aquocobalamin, and methylcobalamin

By

Iya Likhtina
Advisor: Ronald L. Birke

We have studied glutathionylcobalamin, GSCbl, aquocobalamin, H_2OCbl, and methylcobalamin, MeCbl, by optical spectroscopy both with the UV-VIS and electronic CD methods and with DFT electronic structure methods of truncated geometric models. We examined the geometric structure of the models by comparison of DFT calculations with recent high resolution experimental X-ray structure data for the compounds, and we examined the TD-DFT excitation simulations by comparison of the models with measured optical spectra. The DFT (TD-DFT) calculations were used for structural models with the full corrin ring with side-chains replaced with hydrogens and either imidazole, Im, or 5, 6-dimethylbenzimidazole, Bz, as the lower axial base and GS-, H_2O, and CH_3- as the upper axial ligand to Co(III). The calculations employed the B3LYP hybrid functional or the non-hybrid BP86 functional in both in vacuum and water (CPCM) with the 6-311G(d,p) basis set. The optimized geometric structure for six truncated models of GSCbl was made by varying the chemical structure, solvent model, and the two DFT functionals. All show similar geometry for the Co coordination sphere with the average RMDS of the bond distances for six models of 0.02147Å with a standard deviation of 0.00317Å and the average RMSD for the angles of 1.55^o with a standard deviation of 0.20^o both with respect to the experimental X-ray data. Extended charge decomposition analysis, ECDA, shows a CT of 0.717e from the GS^- ligand to the

Co ion with a Mayer bond order of 0.72 between the GS^- fragment and the Co ion fragment, a CT of 0.761e from the Me^- ligand to the Co ion with a Mayer bond order of 0.90 between the Me^- fragment and the Co ion fragment, and a CT of 0.137e from the H_2O ligand to the Co ion with a Mayer bond order of 0.25 between the H_2O fragment and the Co ion fragment. An Energy decomposition analysis, EDA, for a GSCbl model shows E_{int} = -202.24 kcal/mol, E_{prep} = +36.22 kcal/mol, E_{orb} = -108.0 kcal/mol, and E_{steric} = -94.24 kcal/mol. These calculations are for a GS-Co-corrin-Im^+ model at the B3LYP/6-311G(d,p) level in vacuum. EDA of Me-Co-corrin-Im^+ model shows E_{int} = -266.53 kcal/mol, E_{prep} = +19.92 kcal/mol, E_{orb} = -152.6 kcal/mol, and E_{steric} = -113.93 kcal/mol. EDA of H_2O-Co-corrin-Im^+ model shows E_{int} = -22.72 kcal/mol, E_{prep} = +4.52 kcal/mol, E_{orb} = -28.2 kcal/mol, and E_{steric} = +5.48 kcal/mol. An NBO analysis shows that the bonding can be interpreted in terms of 3c/4e ω hypervalent bonds across two collinear N_{eq}-Co-N_{eq} ω bonds in the corrin ring and one collinear S_{ax}-Co-N_{ax} (C_{ax}-Co-N_{ax}) ω bond above and below the Co for GS-Co-corrin-Im^+ (Me-Co-corrin-Im^+) model. For H_2O-Co-corrin-Im^+ model an NBO analysis shows one collinear O_{ax}-Co-N_{ax} ω bond above and below the Co. Absolute optical spectral simulations from TD-DFT excitation calculations for GS-Co-corrin-Im^+ model were compared with the experimental UV-VIS extinction spectrum and the electronic CD differential extinction spectrum. The best fit was found for a GS-Co-corrin-Bz model at the BP86/6-311G(d,p) level with a water cpcm solvent model. The excited state transitions were investigated with Martin's natural transition orbitals. The BP86 calculations also showed π bonding interactions between Co and the axial S of the GS- ligand. Finally, cyclic voltametry experiments were performed for GSCbl and a 1-electron reduction mechanism was assigned for the reaction.

Acknowledgements

I am grateful to my research advisor, Prof. Ronald Birke, for his guidance and care. Prof. Ronald Birke has been extremely supportive and constantly encouraged me to challenge myself during the four and half past years.

I would like to thank Prof. Malgorzata Ciszkowska, Prof. John Lombardi, and Prof. Michael Green, and Prof. Lakshman for their guidance and interest in my education.

The assistance in using AOMix program and data reduction programming from my coworker, Azaria Eisenberg, not only helped me to solve technical problems for my research but also was immense source of learning. Azaria's confidence and assertiveness are exemplary.

Finally I would like to express my gratitude to my parents, close relatives and friends for their love and support.

Table of contents

List of figures

Chapter 1

Chapter 2

Chapter 3

List of tables

Chapter 2

Electronic spectroscopy and computational studies of GSCbl, H2OCbl, and MeCbl

Chapter I.

1.1 Introduction and background

Biological importance.

We first consider the relationship of glutathionyl-cobalamin to biologically active cobalamins. Alkylcorrinoids function as cofactors in a number of mammalian and prokaryotic enzyme systems, the most well studied being the cobalamin (Cbl)-dependent enzymes with cofactors of methylco(III)balamin (Me-Cbl(III)) and adenosylco(III)balamin (Ado-Cbl(III)), the so-called coenzymes of vitamin B_{12}. These cofactors contain a cobalt-carbon bond which is cleaved during the enzymatic reaction and are found in humans in the B_{12} –dependent enzymes: methionine synthase (MetH) which binds Me-Cbl and methylmalonmyl-coenzyne A mutase (MMCA) which binds Ado-Cbl. On the other hand, the tripeptide γ-glutamylcysteinylglycine or glutathione (GSH) is a major intracellular reducing agent present in almost all biological tissues and acts to mitigate oxidative stress. The thiolato derivatives of cobalamins were first investigated in 1964 (1) and 1966 (2) including glutathionylcob(III)alamin, GS-Cbl(III). Jacobsen and coworkers in a series of studies (3) considered GS-Cbl (III) to be a natural precursor to the two cobalamin coenzymes and they also considered it likely that GS-Cbl(III) is the predominant form of vitamin B_{12} in mammalian cells (4).

Reports by Brasch, Finke, and coworkers (5) show that glutathionylcobalamin has a unique stability in comparison with other thiolatocobalamins. Considering the fact that

glutathione is present in most biological tissues at much higher concentration (1-10mM) (6) than cobalamin and that it has a high binding affinity for replacing H_2O in H_2O-Cbl(III)$^+$ (5c), GS-Cbl(III) may well be the reservoir for cob(III)alamin in mammalian biological systems. This evidence suggests that GS-Cbl(III) is an important intermediate for biological processes involving vitamin B_{12} species.

The structural chemistry of GS-Cbl has been well studied including NMR spectra (6) and X-ray analysis by EXAFS (7) and X-ray diffraction (8, 9, 10) giving Co-N and Co-S bond distances in thiolatocobalamins. A complete X-ray crystal structure of a thiolatocobalamin, γ–glutamylcysteinylcobalamin, has been obtained that of GS-Cbl (γ–glutamylcysteinylglycinylcobalamin) (8) and very recently that with of GS-Cbl has also been obtained (9). In addition, the synthesis of thiolatocobalamins has been given considerable attention (10, 11). Also, the cyclic voltammetry of adsorbed GS-Cbl has been investigated (12).

The high binding constant of glutathione for aquocob(III)alamin at physiological pH has a number of chemical consequences included the fact that the redox potential for reduction of the Co^{3+} in cobalamin is moved about 0.9 V negative when ligated by glutathionyl, i.e., on going from H_2O-Cbl(III)$^+$ to GS-Cbl(III). This means that the Co^{2+} form, cob(II)alamin, will not form from GS-Cbl by NADPH reduction so that this reduced form of cobalamin would not be available to react with xenobiotic epoxides in mammalian metabolism (13). It was shown that NO reacts directly with GS-Cbl(III) (14) to give nitrosylcobalamin which is the Co^{2+} reduced NO-Cbl(II) species. Also of importance is that NO reacts directly with Cbl(II) with a high binding constant ($\approx 10^9$) but does not react directly with H_2O-Cbl(III) (15). This fact may imply that GS-Cbl(III) could protect

biological systems against the effects of excess NO (14). On the other hand, it has been suggested that GS-Cbl might regulate NO production by nitric oxide synthase (NOS) by promoting all three isoforms of NOS and by inhibiting the iNOS and eNOS isoforms (16). Subsequently, it was found experimentally that various corrinoids can indeed inhibit NOS and molecular modeling showed that it was possible for corrinoids to access the large heme and substrate binding pocket of NO (17). Unfortunately, GS-Cbl was not tested in this study. NO-Cbl(II) does not appear to have been identified *in vivo*, and this is probably because it is rapidly oxidized to nitritocob(III)alamin, NO_2-Cbl(III) (15).

As mentioned above, GS-Cbl may have an important roll to play in human biology as an intermediate in the formation of the Me-Cbl coenzyme. In this role, it appears that GS-Cbl is more active than other forms of cobalamin in promoting methionine synthase (MetH) activity (3a). The mechanistic details of this enzymatic reaction involves direct methyl transfer from the Me-Cbl cofactor to homocysteine, Hcy, producing methionine and cob(I)alamin which is recycled to Me-Cbl(III). In fact, there is a complicated metabolic web involving various forms of cobalamin, GSH, and GS-Cbl, since the transsulfuration pathway takes homocysteine $\rightarrow$ cystathionine $\rightarrow$ cysteine $\rightarrow$ glutathione (GSH). Thus this source of glutathione can reacts enzymatically with H_2O-Cbl(III) to make GS-Cbl which then can promote MetH enzyme activity.

An additional biological role for GS-Cbl is as an agent which could modulate oxidative stress. Elevated levels of Hcy and low serum level of vitamin B_{12} and folate are associated with cardiovascular disease and neurological dysfunction such as found in patients with Alzheimer's disease, AD, (18) which is also associated with oxidative stress (19). Furthermore, impaired MetH activity in the brain has been suggested to be associated

with AD (19), and for this reason, it was suggested that GS-Cbl may have value in treating neurological disease especially AD because it would be a substrate for the eventual biosynthesis of Me-Cbl. (19) In fact, it was recently found that pretreatment of Sk-Hep-1 cells with GS-Cbl or N-acetyl-L-cysteinyl-Cbl have antioxidation effects protecting the cells from the ‘ pro-oxidants ‘ Hcy and H_2O_2 (20).

In the present study we are interested in the electronic and geometric structure of GS-Cbl and the chemical nature of its Co(III)-S bond in comparison with aquo- and methyl- axial ligand bonds to Co(III) in cobalamins. We examine the structures with DFT calculations of truncated models of the entire molecule. Furthermore, we compare the electronic spectroscopy (UV-VIS and CD) of GS-Cbl(III) with H_2O-Cbl(III) and CH_3-Cbl(III) using both experimental spectra and TD-DFT calculated spectra. Activation of the Co^{3+}-C or Co^{3+}-S bond breaking is an important property of the enzyme mechanisms involving Me-Cbl, Ado-Cbl, and GS-Cbl, the latter compound in the putative enzymatic biosynthesis of the former compounds.

The general structure of an R-axial-substituted hexa-coordinated cobalamin is shown in Figure 1.1. In cobalamins the Co ion is axially coordinated by four pyrrole nitrogens from the macrocyle corrin ring which contains four pyrrole groups (A-D) with a negative charge residing in the corrin ring and with seven side-chains. There are several methyl groups on the ring, and six side-chains (a-e, g) are ethyl or propyl amides and a seventh (f) contains a nucleotide with a negatively charged phosphate group, ribose and a 5, 6-dimethylbenzimadazole coordinating base which acts as a lower axial ligand. For Co^{3+} cobalamins, the upper R-axial ligand can be either non-charged as with a H_2O ligand giving an overall +1 charge in aquoco(III)balamin, H_2OCbl^+, or negatively

charged as in CH_3- or GS- giving an overall neutral molecule as in methylco(III)balamin (Me-Cbl) and glutathionylco(III)balamin (GS-Cbl). The R group above the plane of the corrin ring is said to be in the β-axial position, and the 5, 6-dimethylbenzimidazole (DBz) base below the plane is said to be binding in the α-axial position. In most of the truncated model compounds used for electronic structure calculations, the side-chains are replaced by H and this includes the f side-chain so that there is only one full negative charge coming from the corrin ring. Then the models of Me-Cbl(III) and GS-Cbl(III) have a charge of +1, but the model for H_2O-Cbl(III)$^+$ has +2 charge.

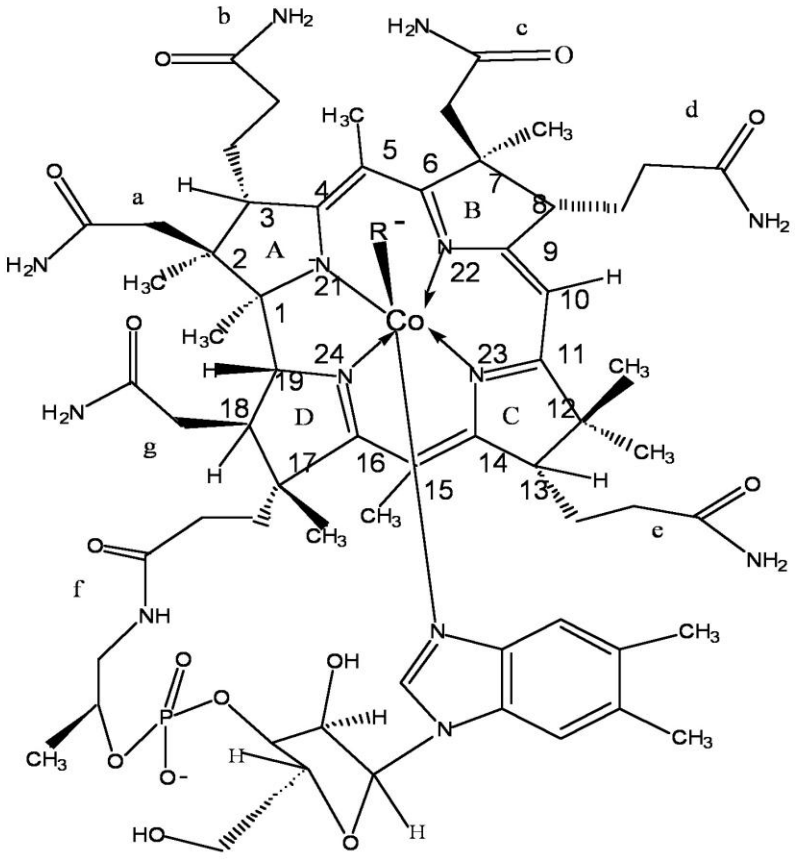

Figure 1.1 Molecular structure of neutral R-Co(III)balamins with rings A-D and side chains a-g.

The glutathionyl ligand, GS^-, is formed when a proton is lost from the sulfur atom of glutathione

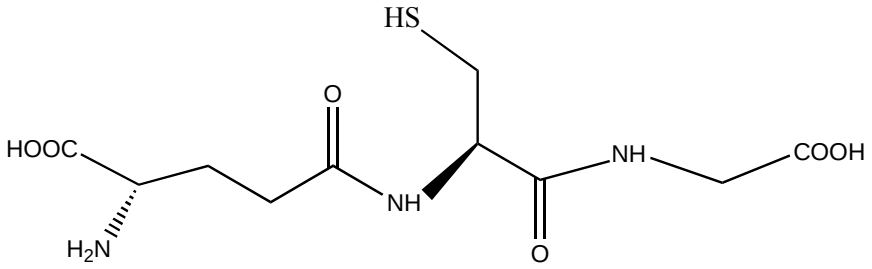

The UV-VIS absorption spectrum of cobalamins has been used to differentiate between various types of cobalamins. The organo-metallic Me-Cbl and Ado-Cbl and other carbanion-cobalamins were designated in a group called "anomalous" or "atypical" compared with the H_2O-Cbl^+ and CN-Cbl as representing the "normal" or "typical" group (21, 22, 23). Five bands were originally singled out (21, 22) as manifested in the H_2O-Cbl+ spectrum (Fig. 1.2 A), two prominent bands in the 500- 600 nm region called α (long wavelength) and β (short wavelength), two low intensity bands around 400 nm called the D (short wavelength) and E (long wavelength), and the intense γ band around 350 nm. These band positions are quite sensitive to the β-axial ligand and the solvent (21, 22). The so-called atypical cobalamins have the γ band shifted to longer wavelength (Fig. 1.2 C). An interesting question is how to explain the spectral differences. It was pointed out some time ago (7) that the spectrum of GS-Cbl (Fig. 1.2 B) was very similar in

position and shape to that of Me-Cbl (Fig. 1.2 B) in the γ -band region.

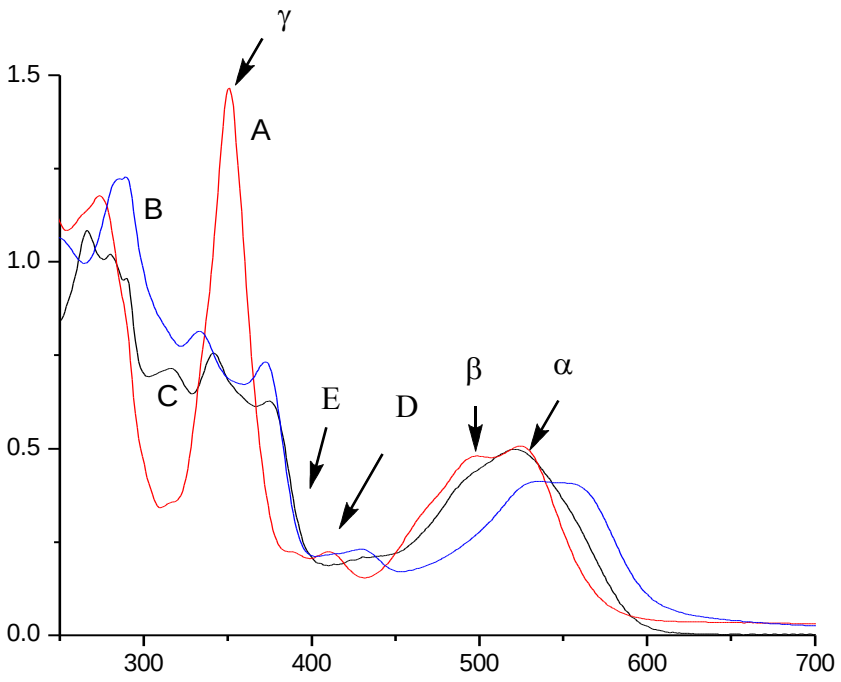

Figure 1.2. UV-VIS spectra of R-Cobalamins. A. Aquo-Cbl(III), B. Glutathionyl-Cbl(III), C. Methyl-Cbl(III) all at pH 5.

The shift of the γ -band in cobalamins is related to the σ-donor strength of the β-axial ligands (22) and this has been explicitly shown experimentally for Co-S bonded cobalamins (7). A large number of common β-axial ligands give cobalamins in the typical group such as H_2O, CN^-, OCN^-, NH_3, Br^-, Cl^-, OH^-, NO_2^-, N_3^-, pyridine, $CH_3CO_2^-$ (21, 22); however, there are also a large number of β-axial ligand giving cobalamins in the so-called atypical group including the cobalamins: Me-Cbl, Ado-Cbl, CH_2=CH-Cbl, $S_2O_3^=$-Cbl, Cysteinyl-Cbl, as-well-as GS-Cbl (22, 24).

In the later group, the ligand not only shifts the γ -band to longer wavelength but causes the band to split into at least two bands on either side of the γ band and shifts the

α/β region to the red. Brunold and coworkers recently concluded that there is an increase in the density of molecular orbitals (MOs) near the HOMO-LUMO gap and extensive mixing between Co 3d and corrin π oribitals for the atypical Me-Cbl and Ado-Cbl compounds which explains the shift in the spectra. (25) It is also seen in Fig, 2 that the α/β region in GS-Cbl is markedly shifted to longer wavelengths and a similar shift is observed in cysteinyl-Cbl. (24) This shift is evidently related to the thiolato ligand. Thus, the features of the thiolato-Cbl spectra will strongly depend on Co(III)-S ligand bond and how this coordination communicates with the corrin ring. In fact the M-$S_{thiolate}$ bond can be quite covalent and involve both a σ and π nature (26).

Another interesting question related to cobalamin electronic spectra is whether there is a vibronic progression in the α/β region of the UV-VIS spectrum. Firth el al. (21) suggested that this occurred for Me-Cbl and this suggestion was repeated in Pratt's review chapter (23). However, in a more detailed consideration made by comparing deconvoluted experimental UV-VIS peaks with DFT calculated electronic transitions, it was concluded that a vibrational progression of the long axis excited state corrin ring vibration (ca. 1250 cm^{-1}) occurs in H_2O-Cbl^+ but not in Me-Cbl since the deconvoluted peaks show different energy splitting in this region for the latter. We will further consider this question for H_2O-$Cbl^{+,}$ Me-Cbl and GS-Cbl. Of considerable interest is how including the solvent in the DFT simulations influences the spectral simulations and whether the transitions suggested to be vibronic can in fact be pure electronic transitions.

There have been a large number of electronic structure calculations for cobalamins. Very early studies of the UV-VIS electronic spectra were made using the semiempirical Hückel and Pariser-Parr-Pople methods (27, 28, 29). More recently many

investigations have been made with density functional theory, DFT, and time-dependent density functional theory, TD-DFT; however, mostly for molecules with the Co-C bond. DFT calculations were used for structure optimization of various alkylcobalamin models and for analyzing the bond distances connected with their bond dissociation enthalpies, BDE (30, 31). Also studies have been made of many different effects which might influence the Co-axial ligand bonding such as the effect of different DFT functionals on BDE (32) and on structure (33), trans-axial ligand effects on the Co-C bond (34) and the influence of electric field on the Co-C bond (31, 35). Other DFT calculation were made for a coenzyme protein bound model (36), the vibrational frequency analysis of Me-Cbl (37) and Ado-Cbl, (38), and the electronic properties of the Co^{2+} reduced form of the cobalamin molecule (39, 40) and the Co^{1+} reduced form. (41, 34 b, 42, 43) Most calculations have been made with DFT but a multiconfigurational (MCSCF) study with CASPT2 was used for a Co^{+}, cob(I)alamin, reduced model (42). It was found that CASPT2 does better than DFT, but the latter gives reasonable results. It has also been concluded by theoretical means (35, 34) that the lower axial N-base does not have a large effect on Co-C bond distance of the upper axial ligand. A MO model which explains this anomalous effect was proposed in a study which used molecular dynamics within the Carr-Parrinello approach and the Becke-Perdew DFT-LSD theory (44). The nature of the axial Co-S and Co-C bond with respect to the Co-Naxial bond has been considered with DFT calculations, EXAFS data and X-Ray crystal structures (45). Here DFT calculations of bond distances in truncated models SO_3Cbl and $(NH_2)_2$CSCbl were compared with X-ray crystal structures. Starting from a highly resolved crystal structures electronic structures of MeCbl (46), CNCbl (47), and AdoCbl (48) have been calculated by the

orthogonalized linear combination of atomic orbitals, OLCAO, DFT method. These were single point calculations but used the entire R-Cbl without truncation. On the other hand, excitation calculation to obtain the electronic transitions was not performed. All of the above electronic structure calculations of cobalamins have been done for the vacuum state.

Characterization by TD-DFT calculations of the nature of the excited states and of the excited state transition for cobalamins have also been of much interest since the UV-VIS and CD spectra show so many features of cobalamins which depend on the type of axial ligands, the oxidation state and coordination number of Co, and the solvent and enzyme environment. The semiempirical calculations of Day (27), based on a 13 atom, 14 π electron, conjugated equatorial ligand model of the corrin ring, show that the α and γ bands shift to lower energy with the donor power of the axial ligands in agreement with experiment. The first extensive TD-DFT exited state study and simulated UV-VIS spectra were calculated by Kozlowski and coworkers with the popular Becke three parameter hybrid exchange functional with the Lee-Yang-Parr correlation functional (B3LYP) for truncated cobalamin models designated CN-Co(III)-corrin-CN and CN-Co(III)-Imidazole (49). The TD-DFT calculations show a shift of HOMO $\rightarrow$LUMO transition to higher energy when -CN was replaced by imidazole which mirrors the α band experimental results on going from CN-Cbl-CN to CN-Cbl in the UV-VIS spectra. An excited state calculation has been made for Co(I)-corrin with both an all electron and an effective core potential (ECP) basis set (41). The assignments for the higher energy states were found to be better with the all electron calculation than with the ECP calculation.

A number of very detailed excited state studies and comparisons with experimental results have been made by Brunold and coworkers. The previously discussed investigation for models of H_2O-Cbl(III)$^+$, Me-Cbl(III), CN-Cbl(III), and Ado-Cbl(III) was made with DFT optimizations of truncated models based on crystal structures. Only the axial ligands and Co were optimized using the Vosko-Wilk-Nusair Local Density Approximation (VWN-LDA) functional with nonlocal gradient correction and basis sets with frozen core orbitals 1s (O, N, C) and 3p (Co). For the TD-DFT excitation calculations, the Perdew-Wang (PW-LDA) functional with gradient correction and also the B3LYP functional were both used with various double-ζ and triple-ζ basis sets. This work again showed that TD-DFT could predict the shifts with change in upper axial ligand in the α and γ bands. TD-DFT simulated absorption spectra of Me-Cbl have also been calculated as a function of different axial ligand bond lengths (Co-C and Co-N_{ax}) and corrin ring distortions in order to simulate spectral effects of the enzyme (MMCA) interaction with the cofactor (50). Electron density difference maps (EDDM) were calculated in the above study and in other studies of a Co^{1+}corrin (43) and Co^{2+}corrin (40) models to examine the nature of the major absorption bands. In the former case (50), the α band shows that electron density is removed from the Co-C bond in addition to the $\pi \rightarrow \pi^*$ corrin ring based transition while the D/E and γ bands are characterized as a metal-to-ligand charge-transfer, MLCT, excitations (50).

Similar calculations were used to simulate the optical spectra of Co^{2+} cobalamin, vitamin B_{12r}, and Co^{2+} cobinamides (39). In cobinamides the nucleotide base loop is cleaved from side chain f in Fig 1.1. It was found that the PW-LDA functional reproduced features in the spectra better than the B3LYP functional with a chemical

model taken from X-ray data. More recently (40) similar calculations have been used to simulate five and four coordinated base-off forms of cob(II)alamin species. The five coordinate form had a water molecule at 2.3 Å replacing the lower axial ligand. For these radical species, the unrestricted pure Kohn-Sham optimization calculations used a VWN-5 and Perdew-Burke-Ernzerhof (PBE) GGA functional with a TZP small core basis set, while the TD-DFT calculations used PW91 and PBE functionals with a TZVP basis set for Co and ligating atoms and the SVP basis set for all other atoms. The results from the TD-DFT excitation calculations reproduce the spectral features of the UV-VIS spectra of the 5-coordinated and 4-coordinated Co^{2+} cobalamins including a small blue shift in the α/β region on going from the five to four coordinated species. The authors found that for a better description of the Co d $\rightarrow$d transitions from the ground state to four ligand field, LF, excited states, it was necessary to use a multireference method, the Spectroscopy ORiented CI, SORCI (43). This method showed that the first two LF excited states differed from the TD-DFT calculations because of extensive CI mixing of 3d electron configurations. All of the above studies that we have discussed so far were gas phase calculations.

Recently after geometry optimization, TD-DFT was used simulated electronic absorption spectra of the excited states of Me-Cbl(III) (51) and Me-Cbl(III) and Ethyl-Cbl(III) (52) truncated models. In the former study either Imidazole or water was used in the truncated structure and the hybrid B3LYP exchange correlation functional was compared with the B86 gradient corrected functional with a 6-31G (d) basis set for all atoms, except Co where a VTZ basis set was employed. TD-DFT over-estimates the excited state energies and usually a simple shift of all lines in the simulated spectra is

used for comparison to experimental results. However, in this study (51) a two parameter fit was used to improve the scaling of the calculated to the experimental spectrum of MeCbl(III) at pH 7. It was found that B3LYP is better at describing corrin $\pi \rightarrow \pi^*$ excitations while B86 did a better job at describing metal-to-ligand excitations. It was found that in the α/β band region, the BP86 calculation gives three transitions whereas in B3LYP only one intense transition is found. In the follow-up study (52) both singlet and triplet excited states were calculated at the BP86/G-31G(d) level as a function of the Co-C bond distance. A mechanism for photodissociation of the Co-C bond in Me-Cbl and Et-Cbl is proposed based on excitation to the first excited state singlet, S_1, followed by intersystem crossing to a repulsive σ^* (Co-C) triplet state. Electron density difference plots show that in the S_0 to S_1 transition, charge density flows from both the Co ion and from the axial σ bond region to the corrin ring. This is somewhat similar but not the exactly the same as found with a B3LYP electron density difference map where the α/β band transition is described as electron density loss from the Co-C bond region and alternating gain and loss from the conjugated portion of the corrin ring (50).

In the present work we characterize the geometry and electronic structure of GS-Cbl, H_2O-Cbl^+, Me-Cbl and examine the effect of water solvent and lower axial base on the electronic spectra of H_2O-Cbl^+, Me-Cbl, as-well-as on and electronic spectra of GS-Cbl.

Chapter 2.

Ground State Computational Studies of GS-Cbl, H_2O-Cbl^+, Me-Cbl

2.1 Computational Methodology

A full geometry optimization was made of the ground state (DFT) for the R-Cbl models followed by calculation of the excited state (TD-DFT) transitions. All calculations were made using the Gaussian 03 (1) or Gaussian 09 (2) package of programs to the default convergence criteria of Gaussian code- 1.00D-08 on RMS density matrix within 128 cycles, 1.00D-06 on MAX density matrix, and 1.00D-06 on energy. The cobalamin systems were calculated both in the gas phase and for a solvent (water) environment with the Conductor Polarized Continuum Model (cpcm) (3). With G03 and G09 the calculations were made with the 6-311G (d,p) basis set (4). For the GS-Cbl model we compared the B3LYP (5, 6) hybrid exchange correlation functional with the BP86 functional, the Becke-Perdew (7, 8) XC-potential, with generalized gradient approximation (GGA), utilizing G09 with the above basis set.

The AOMIX program (9) was used to analyze molecular orbital, MO, compositions, partial density of states, DOS, between molecular fragments, and generalized Wiberg and Mayer bond orders, Charge Decomposition Analysis, CDA, and Energy Decomposition Analysis, EDA. Natural Bond Order (NBO) analysis as implement in G03 and G09 was made on gas phase and aqueous ground state structures.

We have made DFT electronic structure calculations for R-cobalamins with a truncated model which includes the full corrin ring but with all side chain groups replaced by hydrogen atoms and with the 5,6-dimethylbenzimidazole or imidazole as the lower axial base, B, ligand as shown in Figure 2.1. These models can be denoted R-Co(III)-corrin-Bz or R-Co(III)-corrin-Im.

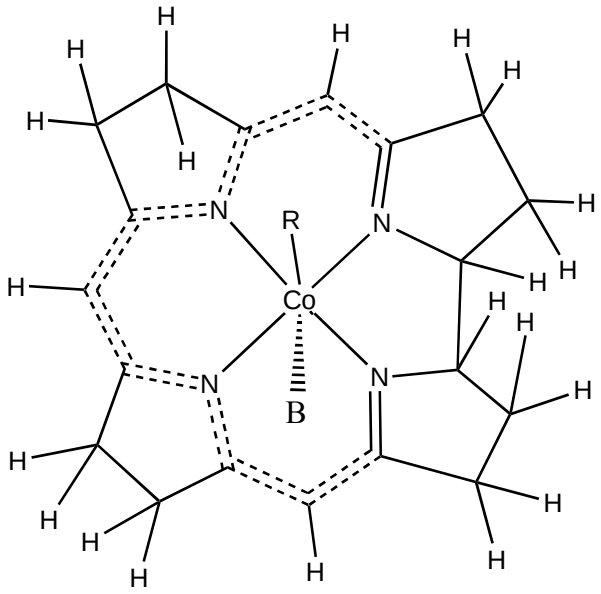

Figure 2.1 Truncated model for the axial substituted cobalamins with all side chains replaced by hydrogen atoms. The thirteen atom conjugated chain in the corrin ring is shown with dotted lines.

The geometry optimized ground state calculations with the water environment converged for H_2O-Cbl(III) and Me-Cbl(III) truncated models with G03; however, for GS-Cbl(III) models they would not converge with G03 but convergence was achieved with G09. We have utilized only one calculation with solvent which did not completely converge with G03, since its structure was found to be an adequate match to X-ray data. This was for the GS-Co(III)-corrin-Im model in water where the geometry structure had

converged for RMS Force, Maximum Displacement and RMS Displacement but not for the Maximum Force which was 0.001123 with a 0.00045 convergence criterion and a predicted change in energy=-2.953641D-05 was found. All other calculations for all truncated models converged completely.

2.2. Results and Discussion

2.2.1. Comparison of bond distances and angles with X-Ray Data

2.2.1.1. Geometry of GS-Cbl(III) Models

We have optimized the geometry of six truncated models of GS-Cbl(III). These models are GS-Co(III)-corrin-imidazole (GS-CblIm$^+$) and GS-Co(III)-corrin-dimethylbenzimidazole (GS-CblBz$^+$) in the gas phase and in water solvent all at the B3LYP level, GS-CblBz$^+$ in water solvent at the BP86 level, and a model where the GS-ligand of GS-CblBz is in the zwitter ion form. In most calculations, the glutathionyl ligand was considered to have both carboxylate groups protonated with a single negative charge on the sulfur so that the calculation is for a singly positively charged cobalamin molecule. In the zwitterionic form the ligand is now considered to have two negative charges since both carboxylate groups are ionized and the amine group on the glutamate moiety is protonated and the sulfur is negative so the GS(zwiiter)-Co(III)-corrin-Bz is neutral. The zwitter ionic form is the major form of GSH in solution between pH 5-9. (10) We compare these optimized structures with the known X-ray crystal structure of GSCbl (11) We also optimized a model, Glu-Cys-Co(III)-corrin-Bz (GluCysCblBz), with

the γ–glutamylcysteinyl axial ligand for comparison with X-ray structure of γ–glutamylcysteinylcob(III)alamin (12). Thus we have six optimized truncated chemical models which can be compared with the known X-ray structures of GS-Cbl and one optimized model for comparison with the X-Ray structure of γ–GluCys-Cbl. For GSCbl a few bond distances are available from EXAFS data (13).

Figure 2.1 shows a geometry optimized ball and stick structure of the GS-CblBz model in water solvent (cpcm). In this structure, as

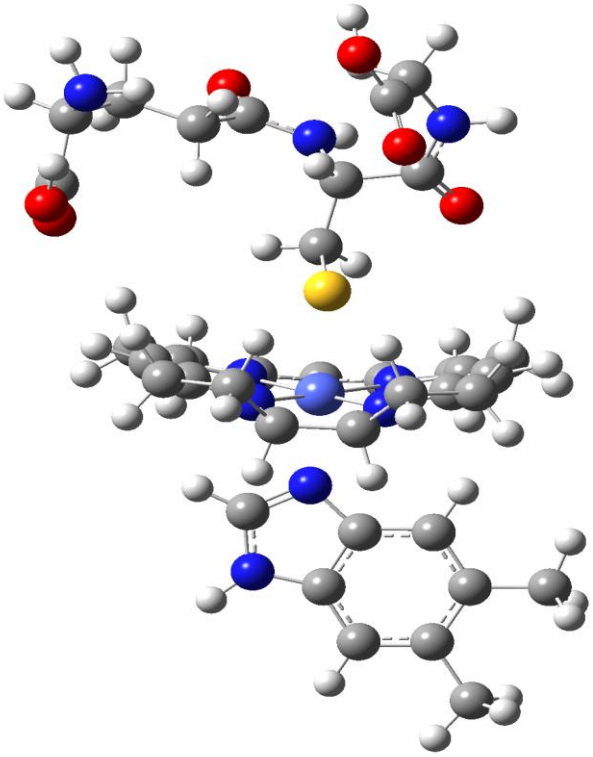

Figure 2.2 Optimized geometry of GS-Co(III)-corrin-Bz at the B3LYP/6-311G(d,p) level with CPCM solvent model.

is true for all seven optimized structures, the four pyrrole N_{eq} equatorial atoms and the S_{ax} and N_{ax} axial ligands form a distorted octahedral structure with the central Co(III) ion. The truncated corrin macrocycle has C_2 symmetry along the short axis (SA) of the ring

formed by the line from C10 and the bisector of the C1 and C19 bond (Fig. 1.1). The long axis (LA) of the corrin ring is the distance between C5 and C15 and approximately bisects the two six membered rings involving Co-N21-C4-C5-C6-N22 and Co-N24-C16-C15-C14-N23 (Fig. 1.1). The imidazole ligand has been used in two of the structures because, of course, it requires less computational effort and is similar to dimethylbenzimdazole but more importantly because in the two mammalian B_{12} dependent enzymes, a histidine (containing imidazole as a base) binds the Co ion in the α-position. (14, 15) This ligand comes from a protein residue and replaces the 5, 6-dimethylbenzimdazole in the active site with the nucleotide tail folded back into a pocket of the protein.

A comparison of selected bond distances, bond angles and dihedral angles of the seven optimized geometries and the X-ray structures of GSCbl (11) and GluCys-Cbl(12) is given in Table 2.1. First it can be pointed out that it is well known from X-ray structures that the axial ligands do not have much of an affect on the bond distances and angles in the corrin ring for the substituted cobalalamins (15). The EXAFS data for GS-Cbl are not highly accurate when compared with the X-ray structure data but give bond distances values of 2.28±0.05 Å for the Co-S, 2.15±0.03 Å for Co-Nax, and 1.89±0.01 Å for Co-Neq. This Co-Nax bond distance is too long by 0.08 Å (11). Both X-ray structures (Table 2.1), however, show a Co-S bond length about .02 Å shorter than any of our theoretical GSCbl models. We note that the EXAFS does not differentiate between the Co-N_{eq} equatorial bond distances in the 5-membered and 6-memembered rings; whereas, all our calculations show the well characterized longer bond distances for the 6-

membered rings over the 5-membered rings (11, 12, 15) These distance are about 0.01Å larger than the X-ray data in our calculations.

The third row from the bottom in Table 2.1 shows the root mean square deviation, RMSD, of the six bond distances for the six models from the GSCbl X-ray data and one model from the GluCys-Cbl X-ray data, where $RMSD = \sqrt{\frac{\sum (RX_{theor} - RX_{x-ray})^2}{N-1}}$. The two models which gives the closest RMSD bond distances to the X-ray data are for GS-CblIm (0.0161 Å) and GS-CblBz (0.0198 Å) with the B3LYP/ 6-311G(d,p) calculations in gas phase, while the next best was for GS-CblBz in water (0.0224 Å) at the BP86/6-311G(d,p) level. The average RMDS of the bond distance for the first six models is 0.02147 with a standard deviation of 0.00317. The average RMSD across the seven models is not much different with an average of 0.0226 RMSD. Comparing the average value of the standard deviation RMSDs between the six models (0.00317) with the average value of standard deviation from the average deviation within the six models (0.0112) in an ANOVA strongly indicates that there is no significant statistical difference between these RMS deviations for the various models.

The angle data in Table 2.1 are mainly taken from the angles involving the Co ion and the equatorial N atoms from the corrin ring and the Co ion and the S and N atoms from the axial ligands. The N_{eq}-Co-N_{eq}, N_{eq}-Co-N_{ax}, N_{eq}-Co-S_{ax} angles, are again very close to X-ray data varying by less than 1^o to 2^o from the X-ray structure data showing the distorted octahedral structure. The angle between the Co and the first two thiolate ligand atoms, C_{Me}-S-Co, for all calculation models is somewhat less, by 1-3 degrees, than the $111.3(2)^o$ of the X-ray data and shows the typically C-S-M angle of metal thiolates which is in the range $100\text{-}120^o$ (16). The fact that the angle is greater than 90^o indicates a

pseudo σ bond where the electron density is shifted off the M-S bond (16). The RMSDs for the eight angles in the second row from the bottom of Table 1 is around 1.65^{o} with the B3LYP calculation of GS-CblBz model in vacuum being the smallest (1.33^{o}). The BP86 calculation of GS-CblBz model in water has the second smallest (1.47^{o}) deviation. The average RMDS of the angles for the first six models is 1.55^{o} with a standard deviation of 0.19^{o}. Again the RMSD of the angles across the six models do not much variation and the ANOVA analysis comparing average standard deviation between models (0.185) and average standard deviation with-in models (0.990) shows there is no significant difference between the various RMSDs of the models . Because all the models have very similar geometry, we have used results from both the vacuum and water environment geometric optimization to examine the bonding and electronic structure of the glutathionylcob(III)alamin molecule.

The final row in Table 2.1 is the fold angle φ defined as 180^{o}- Ang(C15CoC5) which is the fold angle across the C5$^{\cdots}$C15 vector (17). This is similar to the upward fold angle for the X-ray data for both γ–GluCys-Cbl and GSCbl which is defined as dihedral angle between two planes formed from atoms (N21C4C5C6N22C9C10) and from atoms C10C11N23C14C15C16N24 (11, 12). The average value of φ of 22.8^{o} for the seven models is close to the value of 24.7^{o} from the X-ray data for GSCbl which is the largest fold found for twenty-six cobalamins (11). Out of twenty-six cobalamins only NCS-Cbl (22.4^{o}) and γ–GluCys-Cbl (24.2^{o}) have experimental fold angles larger than 19^{o} (Table 1, ref.15). Thus our calculations reproduce rather closely the large fold angle for thiolatocobalamins. Also the calculations show that the models with benzimidazole have a larger fold angle than those with imidazole. Thus the gas phase models, GS-CblBz

(23.8^{o}) and GluCys-CblBz (23.7^{o}), with B3LYP and the solution model of GSCblBz (23.3^{o}) with BP86 calculation have the closest values to the experimental result. X-ray structures for cobalamins where benzimidazole was replaced with imidazole also show a smaller fold angle which has been attributed to the smaller bulk of imidazole with respect to the benzimidazole (15). Finally some selected dihedral angles (six) have been compared for the calculation models in Table 2.1. Here the variability across models for the dihedral angles is larger than for bond distances and bond angles.

Table 2.1 Comparison of Bond Distances (Å), Angles (^{o}), and Dihedral Angles (^{o}) for Different Truncated Models with EXAFS and X-Ray Data

	GS-Cbl Zwitterion, Bz cpcm b3lyp	GS-Cbl, Bz cpcm b3lyp	GS-Cbl Bz cpcm, BP86	GS-Cbl, Im cpcm b3lyp	GS-Cbl, Im gas b3lyp	GS-Cbl Bz gas b3lyp	GluCys-Cbl Bz gas b3lyp	GS-Cbl X-ray Diff, Å Ref. 11	GluCys-Cbl X-ray Diff, Å Ref. 12
Co - S	2.3374	2.3373	2.32047	2.33722	2.29584	2.32440	2.31168	2.295(1)	2.267(2)
Co - Nax	2.06676	2.05949	2.04397	2.02319	2.06845	2.08853	2.08663	2.074(3)	2.049(6)
Co – N21eq (5-mem)	1.89783	1.89673	1.88120	1.89793	1.90219	1.90313	1.90512	1.883(3)	1.885(5)
Co – N24eq (5-mem)	1.89494	1.89681	1.88060	1.89209	1.89878	1.89403	1.89546	1.887(3)	1.891(5)
Co – N23eq (6-mem)	1.93324	1.93105	1.92453	1.93221	1.93645	1.92953	1.93712	1.911(3)	1.902(6)
Co – N22eq (6-mem)	1.93374	1.93462	1.92281	1.93414	1.93341	1.93569	1.93382	1.914(3)	1.914(6)
N21CoN24	82.645	82.532	82.546	82.611	82.734	82.599	82.735	82.83(11)	83.2(2)
N22CoN23	94.271	94.293	94.385	94.156	94.286	94.288	94.099	96.30(12)	96.9(3)
N24CoN22	173.749	173.683	173.522	173.845	173.911	173.663	173.720	171.27(13	171.5(3)
N21CoN23	173.808	173.597	173.371	173.937	173.806	173.617	173.674	172.98(12	173.1(2)
N21CoNax	89.872	89.952	90.368	91.266	91.216	90.024	90.027	92.07(12)	92.0(2)
N21CoS	88.168	87.828	87.857	88.693	88.382	86.000	87.854	88.78(9)	87.4(2)
NaxCoS	177.712	177.780	178.209	177.989	178.017	175.929	177.542	177.29(9)	178.1
CMe-S-Co	110.392	108.79	108.225	108.211	109.423	110.321	108.243	111.3(2)	109.7(3)
C15CoC5	157.376	157.785	156.661	158.065	157.785	156.184	156.266		
N21C1C19N24	1.231	0.102	0.793	2.157	0.619	7.912	4.755		
N21CoN24C19	11.373	11.392	13.84	11.765	9.217	13.839	11.079		
C6C7C8C9	-11.036	-9.661	-12.201	-11.907	-12.848	-12.372	-8.025		
C11C12C13C14	12.380	14.545	15.049	14.557	13.700	12.271	15.367		
C16C17C18C19	30.498	30.738	31.228	31.063	31.004	26.508	29.987		
C1C2C3C4	-30.398	-30.591	-31.416	-30.824	-29.986	-31.617	-30.756		
RMSD R-X (Å)	0.0224	0.0227	0.0224	0.0254	0.0161	0.0198	0.0295		
RMSD Ang deg	1.47	1.67	1.47	1.52	1.33	1.85	1.58		
Fold Ang *	22.6	22.2	23.3	21.9	22.2	23.8	23.7	24.7	24.2

*Fold angle defined as 180^o-Ang(C15CoC5)

2.2.1.2. Geometry of H2O-Cbl(III) Models

We have optimized the geometry of three truncated models of H2O-Cbl(III). These models are H2O-Co(III)-corrin-imidazole (H2O-CblIm) in the gas phase, H2O-Co(III)-corrin-dimethylbenzimidazole (H2O-CblBz) in water solvent all at the B3LYP level, and H2O-CblBz in water solvent at the BP86 level. Thus we have 3 optimized truncated models which can be compared with the closest known X-ray structure to H2O-Cbl (18). Figure 5 shows a geometry optimized ball and stick structure of the H2O-CblBz model in water solvent (cpcm).

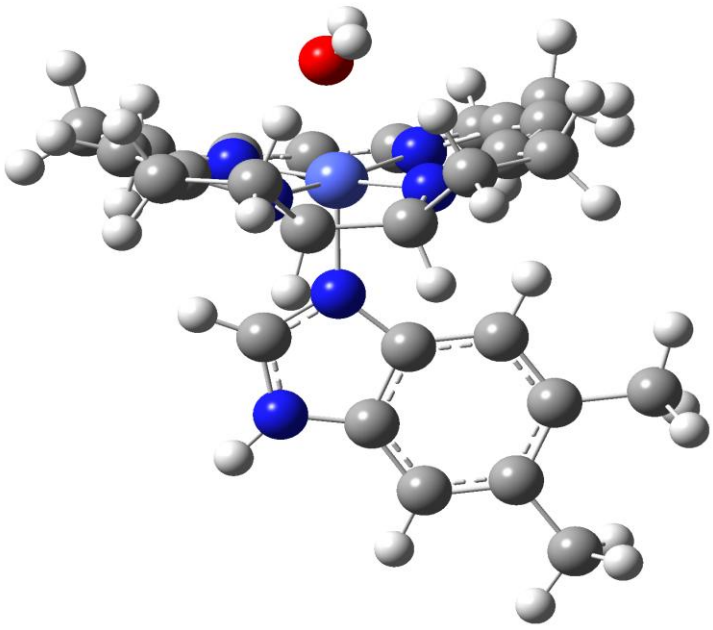

Figure 2.3 Optimized geometry of H2O-Co(III)-corrin-Bz at the B3LYP/6-311G(d,p) level with CPCM solvent model.

Kratky et al. have investigated both the X-Ray diffraction crystal structure and XAFS absorption spectra of both crystalline and aqueous solution of aquocobalamin perchlorate (18). The crystal unit cell has a hundred solvent water molecules in it and the XAFS results are the same for the solid and solution. A comparison of selected bond distances, bond angles and dihedral angles of the three optimized geometries and the X-ray structure of H2O-Cbl perchlorate is given in Table 2.2. Again it can be pointed out that it is well known from X-ray structures that the axial ligands do not have much of an affect on the bond distances and angles in the corrin ring for the substituted cobalalamins (15) First we note that the theoretical corrin models shows a Co-O bond length about 0.10 Å greater than the experimental structure. Also, the X-Ray data differentiates between the Co-N_{eq} equatorial bond distances in the 5-membered and 6-memembered rings as does all the calculations which show the well characterized longer bond distances for the 6-membered rings over the 5-membered rings. These distances for 5-membered rings are about 0.01Å larger and for the 6-membered rings about 0.03Å larger than the X-ray data. The third row from the bottom in Table I shows the root-mean-square deviation, RMSD, of the six bond distances for the three models. The model which gives the closest bond distances to the X-ray data is the BP86/G-311G(d,p) calculation for H2O-Co(III)-corrin-Im (H2O-CblIm cpcm) in water solvent (RMSD = 0.06905), while the second best is the B3LYP/ G-311G(d,p) calculation in water model (RMSD =0.0549071) for the H2O-Co(III)-corrin-Bz (H2O-CblBz cpcm). The individual RMSD across the three models are not much different with an average of 0.052 RMSD. Again comparing the average with the individual RMSD, seems to indicate that there is no significant statistical difference between these calculations results for the various models. These RMSDs are greater than

for GS-Cbl models. The fact that the calculations with a water environment agree better with the X-Ray results is consistent with solvent water being in the unit cell.

The angle data in Table 2.2 is mainly taken from the angles involving the Co ion and the equatorial N atoms from the corrin ring and the Co ion and the S and N atoms from the axial ligands. The N_{eq}-Co-N_{eq}, N_{eq}-Co-N_{ax}, N_{eq}-Co-O_{ax} angles, are again very close to X-ray data varying by less than 1^o to 2^o from the X-ray structure data showing the distorted octahedral structure.

The final row in Table 2.2 is the fold angle φ defined as 180^o- Ang(C15CoC5) which is the fold angle across the C5···C15 vector (17). This is similar to the upward fold angle for the X-ray data for H2O-Cbl perchlorate defined as dihedral angle between two planes formed from atoms (N21C4C5C6N22C9C10) and from atoms C10C11N23C14C15C16N24).(10) The average value of φ of 25.8^o for the three models is not very close to the value of 18.71^o from the X-ray data for H2O-Cbl perchlorate. Thus our calculations deviate from X-Ray data by 7.09^o. Also the calculations show that the models with benzimidazole have a larger fold angle than those with imidazole with the calculation at the BPV86 level of H2O-CblIm in water model (24.76^o) having the closest value to the experimental result. X-ray structures for cobalamins where benzimidazole was replaced with imidazole also show a smaller fold angle which has been attributed to the smaller bulk of imidazole with respect to the benzimidazole (17). Finally some selected dihedral angles (six) have been compared for the calculation models in Table 2.2. Again the variability across models for the dihedral angles is larger than for bond distances and bond angles.

Table 2.2 Comparison of Bond Distances (Å), Angles (^{o}), and Dihedral Angles (^{o}) for Truncated Model with X-Ray Data

	H2O-Cbl, Bz cpcm b3lyp	H2O-Cbl, Im gas b3lyp	H2O-Cbl Im cpcm BPV86	H2O-Cbl X-ray Diff, Å Ref. 18
Co - O	2.064	2.064	2.044	1.952(2)
Co - Nax	1.93514	1.91781	1.893	1.925(2)
Co – N21eq (5-mem)	1.89001	1.89042	1.87649	1.881(2)
Co – N24eq (5-mem)	1.89135	1.89664	1.87914	1.880(2)
Co – N23eq (6-mem)	1.93406	1.93954	1.92783	1.904(2)
Co – N22eq (6-mem)	1.93438	1.94204	1.92810	1.897(2)
N21CoN24	81.913	82.077	81.766	83.03(7)
N22CoN23	93.209	93.332	93.629	95.36(7)
N24CoN22	171.929	172.381	172.274	170.91(6)
N21CoN23	171.732	171.636	172.181	173.88(6)
N21CoNax	91.534	93.046	92.789	91.90(7)
N21CoOax	86.920	87.573	89.259	89.04(7)
NaxCoOax	176.176	179.261	177.908	178.82(6)
C15CoC5	152.335	155.016	155.239	
N21C1C19N24	0.883	-4.375	-2.714	-44.9(2)
N21CoN24C19	15.856	12.517	16.022	
C6C7C8C9	-11.969	-11.303	-13.372	
C11C12C13C14	13.289	10.825	12.898	-25.5(2)
C16C17C18C19	29.624	31.306	31.625	
C1C2C3C4	-30.617	-29.996	-30.496	
RMSD R-X	0.041748	0.04205	0.021672	
RMSD Ang	1.9146	0.736	0.636	
Fold Ang *	27.665	24.984	24.761	

*Fold angle defined as 180^o-Ang(C15CoC5)

2.2.1.3. Geometry of Me-Cbl(III) Models

We have optimized the geometry of three truncated models of Me-Cbl(III). These models are Me-Co(III)-corrin-imidazole (Me-CblIm) in the gas phase and Me-Co(III)-corrin-dimethylbenzimidazole (Me-CblBz) in water solvent at the B3LYP level, and Me-CblBz in water solvent at the BP86 level. Thus we have 3 optimized truncated models which can be compared with a few bond distances obtained from X-Ray data for Me-Cbl (19a), and for ethylcobalamin (Et-Cbl) (19b) as an additional reference. Figure 2.3 shows a geometry optimized ball and stick structure of the Me-CblBz model in water solvent (cpcm).

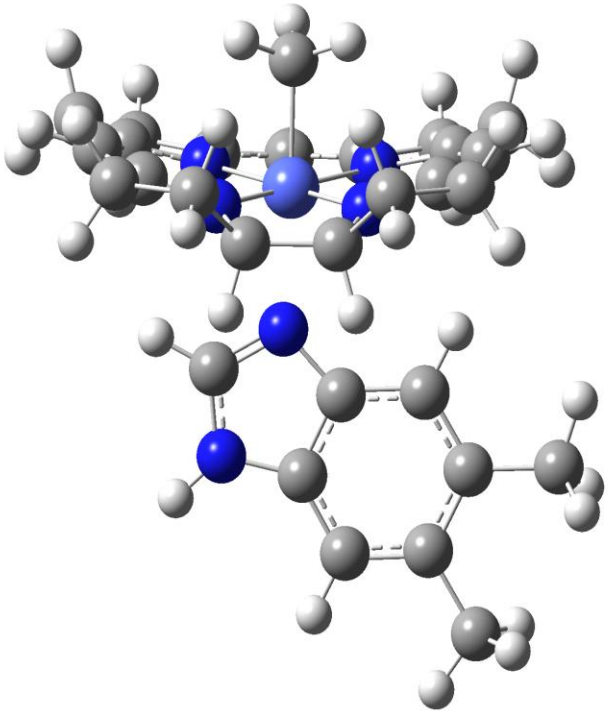

Figure 2.4. Optimized geometry of Me-Co(III)-corrin-Bz at the B3LYP/6-311G(d,p) level with CPCM solvent model.

The X-Ray diffraction data for an early study (1985) of Me-Cbl and the more recent study of Et-Cbl are given in Table 2.3. As seen in the table the earlier study was only accurate to 2-3 significant figures. Thus we have compared our calculations to these earlier results and to the more accurate Et-Cbl X-Ray results. A comparison of calculated selected bond distances, bond angles and dihedral angles of the three optimized geometries with the X-Ray data of Me-Cbl and Et-Cbl is given in Table 2.3. The experimental structures show a Co-Cax bond length which is about 0.01 Å longer for Me-Cbl structure and about 0.05 Å longer for Et-Cbl structure than any of the theoretical corrin models. Again, the X-Ray data differentiates between the Co-N_{eq} equatorial bond distances in the 5-membered and 6-mememembered rings as do as all the calculations which show the well characterized longer bond distances for the 6-membered rings over the 5-membered rings (15). These distances for 5-membered ring are about 0.01Å larger and for the 6-membered rings and about 0.03Å larger than the X-Ray data. The fifth row from the bottom in Table 2.3 shows the root-mean-square deviation from the Me-Cbl X-Ray data, RMSD, of the six bond distances for the three models. The model which gives the closest bond distances to the X-Ray data of Me-Cbl data is the B3LYP/G-311G(d,p) calculation for Me-Co(III)-corr-Im in gas phase (RMSD = 0.0188), while the second best is the B3LYP/ 6-311G(d,p) calculation (RMSD =0.0196) for the Me-Co(III)-corr-Bz in water (Me-CblBz cpcm). The individual RMSD across the three models are not much different with an average of 0.02 RMSD. Comparison of the calculations with the Et-Cbl X-Ray data shows an average root-mean-squared deviation of 0.034. This indicates that the calculations are closer to the X-Ray data of Me-Cbl.

The angle data in Table 2.3 is mainly taken from the angles involving the Co ion and the equatorial N atoms from the corrin ring and the Co ion and the S and N atoms from the axial ligands. The N_{eq}-Co-N_{eq}, N_{eq}-Co-N_{ax}, N_{eq}-Co-C_{ax} angles, are again very close to X-ray data varying by less than 1^o to 6^o from the X-ray structure data showing the distorted octahedral structure.

The final row in Table 2.3 is the fold angle φ. The average value of φ of 22.3^o for the three models deviates from the value of 15.8^o from the X-ray data for Me-Cbl and from the value of 14.7^o from the X-ray data for Et-Cbl. Thus our calculations deviate from X-Ray data by 6.5^o and 7.6^o. Also the calculations again show that the models with benzimidazole have a larger fold angle than those with imidazole with the gas phase at B3LYP level model Me-CblIm (21.50^o) having the closest value to the experimental result. X-ray structures for cobalamins where benzimidazole was replaced with imidazole also show a smaller fold angle which has been attributed to the smaller bulk of imidazole with respect to the benzimidazole. Finally some selected dihedral angles (six) have been compared for the calculation models in Table 2.3. Again the variability across models for the dihedral angles is larger than for bond distances and bond angles.

One can conclude from the large deviations of our calculated fold angles from the X-Ray results for both H2O-Cbl and Me-Cbl that our the definition of φ is not the same as measured fold angles.

Table 2.3 Comparison of Bond Distances (Å), Angles (^{o}), and Dihedral Angles (^{o}) for Different Truncated Models with EXAFS and X-Ray Data

	Me-Cbl, Bz cpcm b3lyp	Me-Cbl, Im gas b3lyp	Me-Cbl Bz cpcm BPV86	Me-Cbl X-ray Diff, Å Ref. 19a	Eth-Cbl X-ray Diff, Å Ref. 19b	But-Cbl X-ray Diff, Å Ref. 19b
Co - Cax	1.97445	1.97371	1.98061	1.99	2.0232	2.032
Co - Nax	2.20707	2.18510	2.16513	2.19	2.232218	2.2439
Co – N21eq (5-mem)	1.89221	1.89423	1.87055	1.88	1.89319	1.864917
Co – N24eq (5-mem)	1.89244	1.89517	1.87022	1.89	1.881317	1.880818
Co – N23eq (6-mem)	1.93313	1.93606	1.92190	1.93	1.906719	1.913017
Co – N22eq (6-mem)	1.93504	1.93508	1.92360	1.97	1.913717	1.909617
N21CoN24	82.588	82.588	82.641	81	83.488	83.447
N22CoN23	94.640	94.706	94.691	95	96.0818	96.037
N24CoN22	173.711	173.773	173.548	173	172.808	172.827
N21CoN23	173.764	173.736	173.579	93	172.707	172.398
N21CoNax	89.488	90.559	89.877	95	90.267	91.24
N21CoC	90.849	91.054	90.538	171	89.399	92.14
NaxCoC	177.072	177.541	176.963			
C15CoC5	157.712	158.499	156.776			
N21C1C19N24	-0.893	-0.338	-0.778			
N21CoN24C19	11.349	10.565	14.144			
C6C7C8C9	-11.715	-11.492	-13.405			
C11C12C13C14	11.575	11.574	13.475			
C16C17C18C19	30.877	30.976	31.353			
C1C2C3C4	-30.693	-30.837	-31.221			
RMSD R-X (Met)	0.01959	0.01884	0.026099			
RMSD R-X (Eth)	0.02927	0.035156	0.038154			
RMSD Ang (Met)	3.48096	3.428641	3.435158			
RMSD Ang (Eth)	1.22725	1.226147	1.0401			
Fold Ang *	22.288	21.501	23.224			

*Fold angle defined as 180^o-Ang(C15CoC5)

2.2.2 Electronic Structure and Molecular Orbitals of GS-Cbl

Figure 2.4 is a stacked bar graph made with AOMIX (9) which shows the orbital electron energy around the HOMO-LUMO gap as a function of the % fragment composition in each MO based on a Mulliken population analysis of the GS-CblIm in gas model calculated at the B3LYP/6-311G(d,p) level. The fragments are the Co ion, S in the GS- ligand, the corrin ring, the imidazole (Im) ligand, and the rest of the structure, i.e., the rest of the glutathione without the sulfur. The HOMO is at -7.401 eV and the LUMO is at -4.626 eV giving a HOMO-LUMO gap of 2.78 eV. If the calculation is done on the other models with benzimidazole replacing imidazole and in water solvent, the HOMO is pushed up (destabilized) about 1.8 eV and the LUMO pushed up by about 2.5 eV giving a HOMO-LUMO gap of about 3.1 eV. The partial % fragments show that the HOMO is dominated by a S atomic orbital ($p\pi$) with small contributions from the Co and corrin ring fragments; whereas, the LUMO is dominated by the corrin ring antibonding orbital. The HOMO-1 energy level has a contributions from the corrin ring but contains the bonding orbital contribution from the GS-Co(III)-Im metal axial ligand structure. This is seen in the isosurface of the orbital in Fig. 2.7.

A plot of the partial density of states, PDOS, made with Gaussian broadening for the same fragments is shown in Figure 2.5. Here it is clear that the DOS at slightly below the HOMO are dominated by the S atom from the GS- ligand and by the corrin ring. The S fragment DOS shows three peaks below the HOMO at -7.40, -9.07, and -10.8 eV and the corrin ring also shows three peaks in this region at -7.86, -8.47, and -9.26 eV. The imidazole, Im, DOS peaks at -9.56 eV and the Co atom DOS peaks at -10.13 eV.

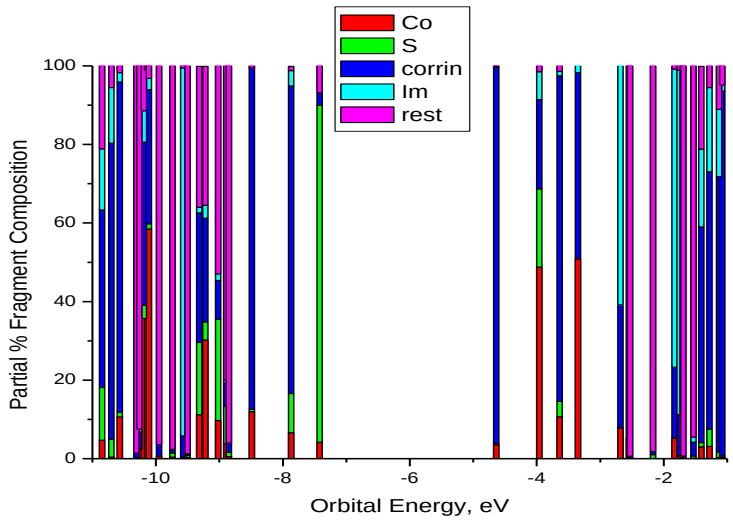

Figure 2.5. Orbital Energies as a Function of Fragment for the GS-CblIm in gas model. Made with AOMix-CDA for B3LYP/6-311G(d,p) SCF=Tight. The fragments are the Co ion, S of the thiolate, the entire corrin ring with all side-chains replaced with H, Imidazole (Im) ligand, and the rest of the molecule.

At and above LUMO, the DOS is completely dominated by π* coring ring orbitals and, in fact, the band for the total DOS which peaks at -4.65 eV coincides exactly with the vacant orbital corrin ring DOS . There is a second DOS band for the vacant corrin ring at -3.56 eV which is in the same region as the double peaks of Co atom virtual DOS (-3.93 and -3.38 eV) .

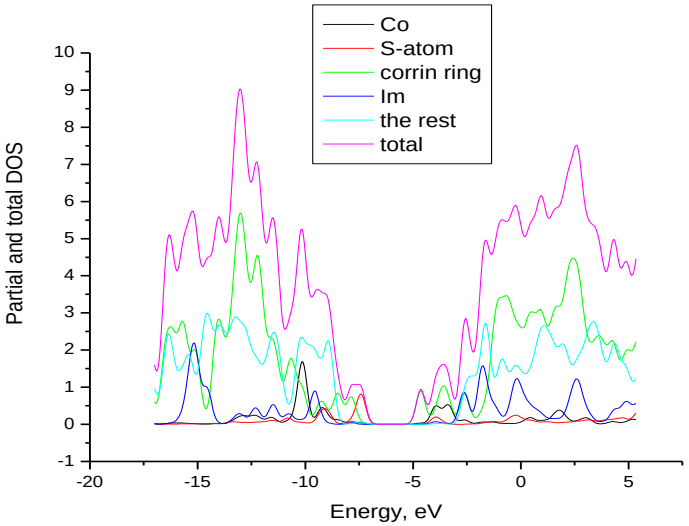

Figure 2.6. Partial and Total DOS for Fragments as a Function of Orbital Energy for the GS-CblIm in gas model. Made with AOMix-CDA for B3LYP/6-311G(d,p).

More detail is seen in the molecular orbital isosurfaces in Figure 2.6 for the filled orbitals which show both bonding and anti-bonding interactions. Also the isosurfaces for 30 molecular orbitals from HOMO-19 to LUMO+9 for GS-Co-corrBz+ at BP86/6-G311(d,p) level are shown in Appendix I.

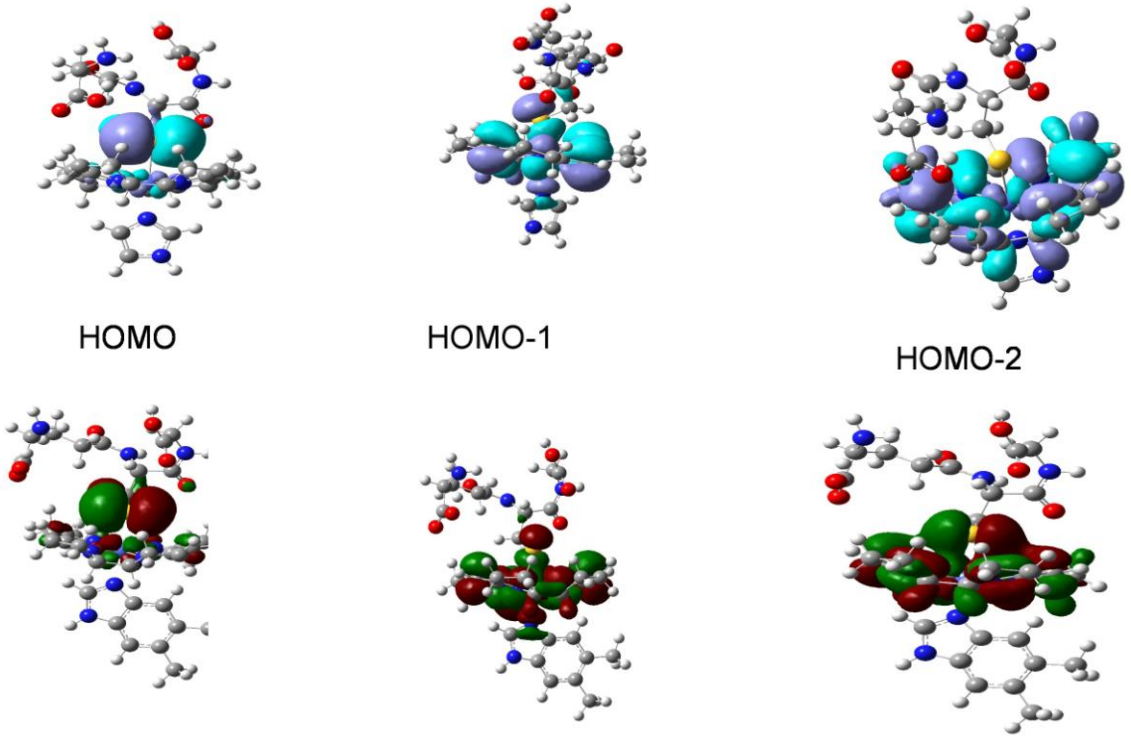

Figure 2.7. Frontier MO Isosurfaces from GS-CblIm (gas) B3LYP/6-311G(d,p) model on-top and GS-CblBzm(H_2O)BP86/6-311G(d,p) model the on-bottom. HOMO-1 shows the pseudo-σ Co-S bond and HOMO-2 shows a π Co-S bond with BP86 but not with B3LYP.

The HOMO shows a π anti-bonding interaction between the $3p_y$ sulfur orbital and the $3d_{yz}$ Co orbital and weak σ bonding between the Co(dyz) and two Neq groups in the corrin ring. On the other hand, the HOMO-1 shows the off-axis pseudo-σ bond formed

between the sulfur $3p_z$ orbital and $3d_{xz}$ Co orbital. These MOs are very similar for the two models, i.e. for GS-CblIm(gas)B3LYP/6-311G(d,p) and GS-CblBzm(H_2O)BP86/6-311G(d,p). However, the HOMO-2 is very different in the two models with B3LYP GS-CblIm(gas) showing no Co-S bond whereas a π(Co(dyz)-Spy) bond is clearly evident in the GS-CblBzm(H_2O)BP86 model. The HOMO-2 for a GS-CblBzm(H_2O)B3LYP/6-311G(d,p) model is the same as the GS-CblIm(gas)B3LYP/6-311G(d,p) model so the difference in the HOMO-2 isosurfaces in Fig. 2.6 is in the DFT. The BP86 shows the π bonding which is not seen with B3LYP. The excitation calculations with BP86 using natural transition orbitals demonstrate significant involvement of both σ bonded and π bonded Co-S in the molecule.

2.2.3 Charge Decomposition Analysis and Energy Decomposition Analysis of R-Cbls

2.2.3.1 CDA and EDA of GS-Cbl

The bonding can be discussed in terms of a donor-acceptor interaction using the Charge Decomposition Analysis (CDA) as calculated with the *AOMIX-CDA* program (9). The CDA is based on the model of Dewar-Chatt-Duncanson as formulated by Dapprich and Frenking (20). In this method the donation, back-donation, repulsion, and residue terms are calculated between fragments for each MO of the complex (Table 2.4). The wavefunction of the complex, in our case GS-Co-Corr-Im, is expressed in terms of a linear combination of fragment molecular orbital, FMO, of the ligand GS- (fragment 2) and of the remaining fragment, Co-Corr-Im (fragment 1). Thus the donation (i) is from

the mixing of the occupied fragment MOs (OMOs) of GS- with the unoccupied fragment MOs (UMOs) of Co-Corr-Im, the back-donation (ii) from the mixing of OMOs of Co-Corrin-Im with the UMOs of GS-, the repulsion (iii) from the repulsive polarization of the OMOs of GS- with the OMOs of Co-Corr-Im, and the residue term,Δ, (iv) from the mixing of the UMOs of GS- with the UMOs of the Co-Corr-Im (21). The sum of this latter Δ term is close to zero (Table 2.4) which shows that the compound can be classified as a donor-acceptor complex (21).

Table 2.4 shows that the HOMO-1 and the HOMO-5 have the largest amount of alpha-spin orbital charge donation, i. e., +0.058 e and +0.022 e, respectively which is consistent with the isosurfaces on Fig. 2.6 and in Appendix I. The donation is from the thiolate ligand fragment, RS-, to the rest of the complex and as seen from the isosurfaces, this is σ-charge donation from the S to the Co d orbitals. The total α-spin donation is 0.204 e and that of the back-donation is -.011 with the sum of total α-spin + β-spin donation, 2 $\rightarrow$1, of 0.408 e and net donation of 0.386 e. However, the donation and the back-donation terms do not only include charge transfer, CT, from occupied to unoccupied orbitals but also include electronic polarization in the orbitals. Thus the difference between the two terms is a measure of overall reorganization of the electron density and not the net CT. Thus it is difficult to separate the two effects in the small back-donation terms such as in the HOMO (0.005 e) and the HOMO-1 (0.006 e) which might indicate back-donation from Co to S or electronic polarization, Pl. These two MOs also show the largest repulsive polarization terms and make up most of the closed-shell repulsion.

The *AOMIX-CDA* (9) program also allows an extended charge decomposition analysis (22), EDCA. This analysis isolates the CT from the electronic polarization. It shows a net 0.717 electrons transferred by charge donation from fragment 2, RS-, to fragment 1, Co-Corrin-Im, with a net 9.2% electronic polarization between fragment 1 and fragment 2. The discrepancy between the 0.386 e CT from the CDA and the 0.717e CT from the ECDA must come from a large electronic polarization contribution in the 2 $\rightarrow$1 donation which lowers the amount of CT in the CDA. Examination of the change in the fragment orbital populations when binding in the molecule in terms of % FO contributions to OMOs and UMOs of the molecule shows there is considerable electronic rearrangement. Most of the populations of the fragment orbitals do not change on going from separated fragments to bound fragments, i.e., OFO population from the separated fragments remain close to 100% occupied in the molecular complex and UFO remain close to 100% unoccupied in the complex. However, there are dramatic changes for two of the fragment orbitals on forming the complex. These are the LUFO from Fragment 1 (Co-Corr-Im) and the HOFO-1 from fragment 2 (GS-). In the complex, the LUFO of the Co-Corr-Im fragment is no longer totally unoccupied and contributes 39.88 % to OMOs while 60.12 % remains in UMOs in GS-Co-corr-Im complex. This is most likely the result of CT to this LUFO in the formation of the Co-S bond. On the other hand, while HOFO-1 of fragment 2 (GS-) still contributes 71.70 % to OMOs in the complex, now 28.29 % population has moved into UMOs of the GS-Co-Corr-Im. This latter amount corresponds to the electronic polarization which would lower the amount of CT calculated by the CDA and shows the utility of the ECDA (22).

Further insight into the nature of the bonding interaction can be gained by using an energy decomposition analysis, EDA, as investigated by Kitaura and Morokuma (23) and the related extended transition state, ETS, analysis of Ziegler and Rauk (24). The binding energy of two fragments, A, B, in the complex, A-B, can be divided into the sum of a preparation energy, also called deformation energy, and the interaction energy

$$E_{binding} = E_{int} + E_{prep}\,.$$

The binding energy can be calculated from the difference in energy between the optimized A-B complex and the sum of each optimized fragments. The preparation energy is the energy required to take fragment A and B from their ground state equilibrium geometry to their ground state geometry in the A-B complex. The interaction energy $E_{int} = E_{binding} - E_{prep}$ can be directly calculated from the energy difference between the optimized A-B complex and the sum of the energy (single point calculations) of fragments A and B in their ground state geometry in the A-B complex. Such a calculation for E_{INT} between the two fragments in the AOMIX analysis without BSSE correction is -202.24 kcal/mol. The binding energy for the model reaction

$$GS^{1-} + \text{Co-Corr-Im}^{2+} \rightarrow \text{GS-Co-corrin-Im}^{1+}$$

in vacuum with B3LYP/6-311G(d,p) is calculated to be -166.01 kcal/mol. Thus preparation energy is $E_{prep} = E_{binding} - E_{int}$ = +36.23 kcal/mol. Analysis of the individual preparation terms shows the preparation energy is 66.01% from the deformation of the Co-Corr-Im^{2+} fragment and 33.99% from the defomation of the GS^{-} fragment.

The interaction energy between the two fragments can be partitioned between three terms

$$E_{INT} = E_{ES} + E_{EX} + E_{ORB}$$

where E_{ES} is the electrostatic interaction energy, E_{EX} is the Pauli repulsion and exchange energy, and E_{ORB} is the orbital interaction energy which includes charge transfer and electronic polarization energy, E_{EPL}. Thus $E_{ORB} = E_{CT} + E_{EPl}$. With the calculated value E_{ORB} = -108.0 kcal/mol, the difference, E_{INT} - E_{ORB} = - 94.24 kcal/mol which is the so-called steric interaction energy, i.e., E_{steric}= E_{ES} + E_{EX}. Since the GS^- fragment has a -1 charge and the Co-Corrin-Im^{2+} has a 2+ charge, there must be a positive electrostatic attraction which should dominate the steric interaction energy. The orbital interaction energy which is slightly more than half of the total interaction energy contains the bond stabilization due to CT and the electronic polarization between the fragments. From the above extended charge decomposition analysis, this CT is 0.72 electrons which should come from the axial S atom donation to the Co ion.

The bonding interactions can clearly be seen in the overlap population density of states, OPDOS, of *AOMIX* where the overlap population can be extended to user defined fragments such as the central metal atom, Co, the sulfur atom of the β-axial ligand and the equatorial corrin ring ligand as in Figure 2.8. The positive overlap population, $OP_{AB,}$ represents a bonding interaction while negative values represents an anti-bonding interaction with $OP_{AB,i} = \sum_{a \in A} \sum_{b \in B} 2 c_{ai} c_{bi} S_{ab}$ were A,B are user defined fragments and the sum for the ith MO is over the products of LCAO-MO coefficients, c_{ai} c_{bi}, and the S_{ab} overlap integral. The negative stick (S function) on the black Co-S line in Fig. 2.8 at -7.40 eV is the π anti-bonding interaction in the HOMO while the positive stick below it at -7.86 eV is the σ bonding interaction in the HOMO-1. There are several peaks in the

OPDOS from the occupied MOs for Co-S bonding in -12 eV to -7.4 eV region while the strong bonding interactions between Co-corrin ring are in -14 eV to -11 eV region.

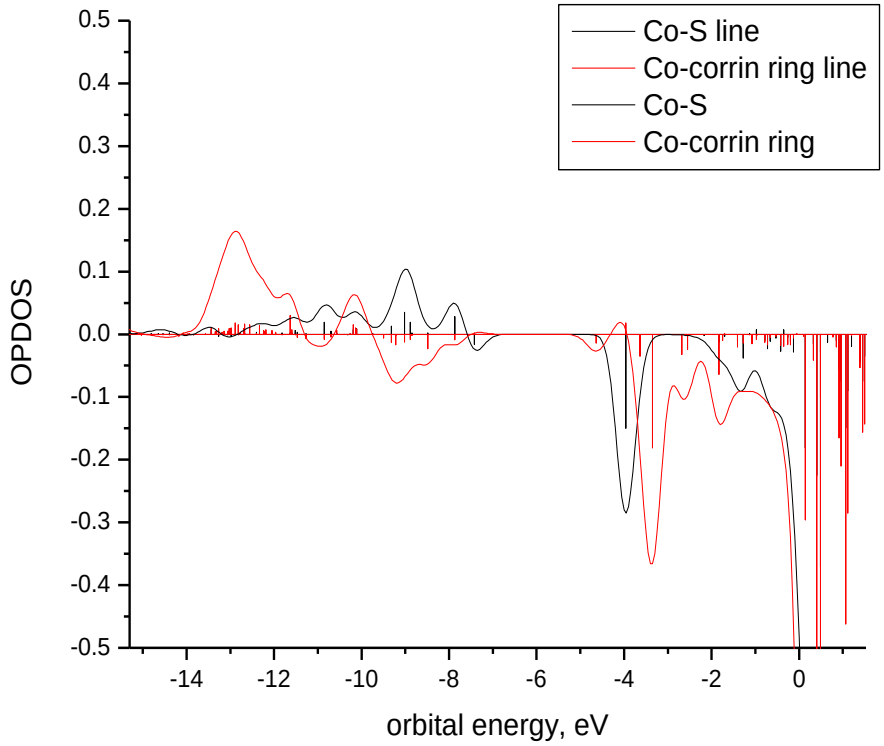

Figure 2.8. Overlap population (Sticks) and Overlap Density of States (OPDOS) for Co-S and Co-corrin bonding in the GS-Cbl-Im gas-phase model (B3LYP/6-311G**) from AOMIX.

It is interesting to compare the two-centered bond orders for the R-Co-corrin-Im models as calculated from the DFT calculation (B3LYP/6-311G(d,p) in the gas phase. With AOMIX (9) the generalized Wiberg and Mayer bond orders calculated from the canonical MOs in the AO basis are the same for closed shell spin-singlet state calculation. The generalized 2-center Mayer (Wiberg) bond order indices, $B_{AB,}$ between fragments A and B are defined as

$$B_{AB} = \sum_{a \in A} \sum_{b \in B} (PS)_{ba} (PS)_{ab} \qquad (1)$$

where P is the total density matrix and S is the atomic orbital overlap matrix (25).

A four fragment bond index calculation can be made with the axial ligand R, $Co^{3+,}$ the corrin ring and the axial base as the fragments. The generalized Mayer (Wiberg) bond orders between the β-axial ligand R and Co^{3+}, with R = Me^-, GS^-, and H_2O are 0.901, 0.778, and 0.257, respectively, in the R-Co-Corr-Im model complex. If the bond order comes primarily from the β-axial ligand atom attached to Co, then the Me-Co bond order is closest to a pure covalent sigma organo-metallic bond. Since the GS-Co bond order is very close to that of Me-Co, it also shows a significant amount of covalent character especially in comparison to the quite low generalized Mayer (Wiberg) bond order for the O-Co bond from water. If a two fragments calculation is made with R and Co(III)-Corr-Im^{2+} as the fragments, then the bond indexes between the two fragments are 1.02, 1.03, and 0.342 for R = Me-, GS-, and H_2O, respectively. In the case of GS-Co-corr-Im^+, the high bond index of 1.03 comes from interactions in addition to the S-Co bond. Thus the four fragment calculation shows that there is a direct interaction of the GS^- ligand with the corrin ring fragment itself since this bond index is 0.180. On the other hand, the bond index for Me^- with the corrin ring is only 0.054 showing that the C-Co bond is indeed closer to a pure σ covalent bond than the S-Co bond. For comparison, the Wiberg bond index for Co-S in orthogonal natural atomic orbital (NAO) basis for the GS-Co-corr-Im model is 0.682 (Table 2.8).

Table 2.4 Charge Decomposition Analysis of the GS-Co-Corr-Im with GS- as Fragment 2 and the Rest (Co-Corr-Im) of the Molecule as Fragment 1 for Major Contributions.

α-spin MO	Donation 2→ 1	Back donation 1→ 2	Repulsion	Residue Δ term
HOMO-7 (#187)	0.008	0.001	-0.024	0.000
HOMO-6 (#188)	0003	-0.001	-0.002	0.000
HOMO-5 (#189)	0.022	0.002	-0.001	0.001
HOMO-4 (#190)	0.011	0.001	0.000	0.000
HOMO-3 (#191)	0.011	0.000	-0.004	0.000
HOMO-1 (#192)	0.053	0.006	-0.077	0.002
HOMO (#193)	0.008	0.005	-0.120	0.000
Sum over α- MOs	0.204	-0.011		
Total α + β	0.408	-0.022	-.233[a]	-.002[a]

a. Total over occupied MOs

2.2.3.2 CDA and EDA of H2O-Cbl

Table 2.5 shows that the HOMO and the HOMO-9 of H2O-Co-corrIm^{2+} have the largest amount of alpha-spin orbital charge donation, i. e., +0.016 e and +0.002 e, respectively. The donation is from the water ligand fragment, H2O-, to the rest of the complex and for H2O-Cbl this is σ-charge donation from the O to the Co d orbitals. The total α-spin donation is 0.087 e and that of the back-donation is -.020 with the sum of total α-spin + β-spin donation, 2 →1, of 0.174 with anet donation of 0.134. However, the donation and the back-donation terms do not only include charge transfer, CT, from occupied to unoccupied orbitals but also include electronic polarization in the orbitals. Thus the difference between the two terms is a measure of overall reorganization of the electron density and not the net CT. Thus it is difficult to separate the two effects in the small back-donation terms such as in the HOMO (0.004 e) and the HOMO-10 (0.003 e) which might indicate back-donation from Co to O or electronic polarization, Pl. These

two MOs also show the largest repulsive polarization terms and make up most of the closed-shell repulsion.

The *AOMIX-CDA* extended charge decomposition analysis, EDCA, shows a net 0.174 electrons transferred by charge donation from fragment 2, H2O-, to fragment 1, Co-Corrin-Im, with a net 4.7% electronic polarization between fragment 1 and fragment 2. The discrepancy between the 0.134e CT from the CDA and the 0.174e CT from the ECDA must come from an electronic polarization contribution in the $2 \rightarrow 1$ donation which lowers the amount of CT in the CDA. This is a small amount of electronic polarization when compared to the results for the GS-Co-corr-Im case (2.2.3.1). Examination of the change in the fragment orbital populations when binding in the molecule in terms of % FO contributions to OMOs and UMOs of the molecule shows there is considerable electronic rearrangement. Most of the populations of the fragment orbitals do not change on going from separated fragments to bound fragments, i.e., OFO population from the separated fragments remain close to 100% occupied in the molecular complex and UFO remain close to 100% unoccupied in the complex. However, there are some changes for four of the fragment orbitals on forming the complex. These are the HOFO and LUFO from Fragment 1 (Co-Corr-Im) and the HOFO and HOFO-1 from fragment 2 (H2O-). In the complex, the LUFO of the Co-Corr-Im fragment is no longer totally unoccupied and contributes 51.60 % to OMOs while 48.40 % remains in UMOs in H2O-Co-corr-Im complex. This is most likely the result of CT to this LUFO in the formation of the Co-Oax bond. On the other hand, while HOFO-1 of fragment 2 (H2O-) still contributes 94.97 % to OMOs in the complex, now 5.04 % population has moved into UMOs of the H2O-Co-Corr-Im, and HOFO of fragment 2 (H2O-) still contributes

96.59 % to OMOs in the complex, whereas, now 3.42 % population has moved into UMOs of the H2O-Co-Corr-Im. This latter amount corresponds to the electronic polarization which would lower the amount of CT calculated by the CDA.

Further insight into the nature of the bonding interaction can be gained by using an energy decomposition analysis, EDA. Such a calculation for E_{INT} between the two fragments in the AOMIX analysis without BSSE correction is E_{INT} = -22.72 kcal/mol. The binding energy for the model reaction

$$H2O + Co\text{-}Corr\text{-}Im^{2+} \rightarrow H2O\text{-}Co\text{-}corrin\text{-}Im^{2+}$$

in water solution with B3LYP/6-311G(d,p) is calculated to be $E_{binding}$ = -18.2 kcal/mol. Thus the preparation energy is $E_{prep} = E_{binding} - E_{int}$ = +4.52 kcal/mol. Analysis of the individual preparation terms shows the preparation energy is almost 95.99% from the deformation of the Co-Corr-Im^{2+} fragment and 4.01% from deformation of H2O fragment. The net preparation energy is much smaller than for the GS-Co-corr-Im because there is less influence of water than glutathionyl ligand on the preparation energy.

The interaction energy between the two fragments can be partitioned between three terms $E_{INT} = E_{ES} + E_{EX} + E_{ORB}$

where E_{ES} is the electrostatic interaction energy, E_{EX} is the Pauli repulsion and exchange energy, and E_{ORB} is the orbital interaction energy which includes charge transfer and electronic polarization energy, E_{EPL}. Thus $E_{ORB} = E_{CT} + E_{EPl}$. With the calculated value E_{ORB} = -28.2 kcal/mol, the difference, $E_{INT} - E_{ORB} = E_{steric}$ = +5.5 kcal/mol which is the so-called steric interaction energy, i.e., $E_{steric} = E_{ES} + E_{EX}$. Since the H2O fragment has a negative dipole toward oxygen and the Co-Corrin-Im^{2+} has a 2+ charge, there must be an

electrostatic attraction or negative energy contribution to the steric energy from the electrostatic term. This means the Pauli repulsion positive energy term dominates the steric energy. The interaction energy is thus dominated by the orbital energy term which contains the bond stabilization due to CT and the electronic polarization between the fragments. From the above extended charge decomposition analysis, this CT is 0.137 electrons which should come from the axial O atom donation to the Co ion. The interaction energy is much less for H_2O-Co-corr-Im^{2+} than for the GS-Co-corr-Im^{+}. This should be due to the very small electrostatic attraction and the much lower CT or covalent character of the Co-Oax bond.

Table 2.5 Charge Decomposition Analysis of the H_2O-Co-Corr-Im with H_2O- as Fragment 2 and the Rest (Co-Corr-Im) of the Molecule as Fragment 1.

α-spin MO	Donation 2→ 1	Back donation 1→ 2	Repulsion	Residue Δ term
HOMO-17 (#100)	0.002	0.001		
HOMO-10 (#188)	0.000	0.003	-.004	0.000
HOMO-9 (#108)	0.002	0.002	-.022	0.000
HOMO-8 (#109)	0.000	0.001	-.002	0.000
HOMO-6 (#111)	0.001	0.002	-.003	0.000
HOMO-5 (#112)	0.000	0.001	-.002	0.000
HOMO (#117)	0.016	0.004	-.034	0.000
Sum over α- MOs	0.087	0.020	-	-
Total α + β	0.174	0.040	-0.080	-0.005

a. Total over occupied MOs

2.2.3.3 CDA and EDA of Me-Cbl

Table 2.6 shows that the HOMO and the HOMO-4 of CH3-Co-corr-Im^{+} have the largest amount of alpha-spin orbital charge donation, i. e., +0.056 e and +0.063 e, respectively. The donation is from the methyl ligand fragment, CH_3-, to the rest of the

complex. This is σ-charge donation from the C_{ax} to the Co d orbitals. The total α-spin donation is 0.146 e and that of the back-donation is 0.025 with the sum of total α-spin + β-spin donation, 2 →1, of 0.292 e and net donation of 0.241 e. However, the donation and the back-donation terms do not only include charge transfer, CT, from occupied to unoccupied orbitals but also include electronic polarization in the orbitals. Thus the difference between the two terms is a measure of overall reorganization of the electron density and not the net CT. Thus it is difficult to separate the two effects in the small back-donation terms such as in the HOMO (0.005e) and the HOMO-5 (0.007e) which might indicate back-donation from Co to Cax or electronic polarization, Pl. These two MOs also show the largest repulsive polarization terms and make up most of the closed-shell repulsion. Table 2.6 also shows a relatively large negative repulsive term of -0.174 which indicates that electronic charge is removed from occupied/occupied fragment orbitals. This repulsive term is similar for GS-Co-corr-Im (-0.233) in Table 2.4 and is much less than for H2O-Co-corr-Im (-0.080) in Table 2.5. The delta residual term is zero which indicated that Cax-Co bond is formed by CT.

The *AOMIX-CDA* extended charge decomposition analysis, EDCA, shows a net 0. 761 electrons transferred by charge donation from fragment 2, Me-, to fragment 1, Co-Corrin-Im, with a net 13.6% electronic polarization between fragment 1 and fragment 2. The discrepancy between the 0.242 e CT from the CDA and the 0.761e CT from the ECDA must come from a large electronic polarization contribution in each fragment in the 2 →1 donation which lowers the amount of CT in the CDA. Examination of the change in the fragment orbital populations when binding in the molecule in terms of % FO contributions to OMOs and UMOs of the molecule shows there is considerable

electronic rearrangement. Most of the populations of the fragment orbitals do not change on going from separated fragments to bound fragments, i.e., OFO population from the separated fragments remain close to 100% occupied in the molecular complex and UFO remain close to 100% unoccupied in the complex. However, there are dramatic changes for two of the fragment orbitals on forming the complex. These are the LUFO from Fragment 1 (Co-Corr-Im) and the HOFO from fragment 2 (CH3-). In the complex, the LUFO of the Co-Corr-Im fragment is no longer totally unoccupied and contributes 51.60 % to OMOs while 48.40 % remains in UMOs in Me-Co-corr-Im complex. This is most likely the result of CT to this LUFO in the formation of the Co-Cax bond. On the other hand, while HOFO of fragment 2 (CH3-) still contributes 60.07 % to OMOs in the complex, now 39.94 % population has moved into UMOs of the Me -Co-Corr-Im. This latter amount corresponds to the electronic polarization which would lower the amount of CT calculated by the CDA and again shows the utility of the ECDA.

Further insight into the nature of the bonding interaction can be gained by using an energy decomposition analysis, EDA. Such a calculation for E_{INT} between the two fragments in the AOMIX analysis without BSSE correction is E_{INT} = -266.53 kcal/mol. The binding energy for the model reaction

$$CH_3^- + \text{Co-Corr-Im}^{2+} \rightarrow CH_3\text{-Co-corrin-Im}^{1+}$$

in vacuum with B3LYP/6-311G(d,p) is calculated to be $E_{binding}$ = -246.61 kcal/mol. Thus preparation energy is $E_{prep} = E_{binding} - E_{int}$ = +19.92 kcal/mol. Analysis of the individual preparation terms shows preparation energy is almost 89.64% from the deformation of the Co-Corr-Im^{2+} fragment and 10.56% from deformation of methyl anion fragment. The net preparation energy is slightly smaller than for the GS-Co-corr-Im because there is less

influence of methyl anion (CH_3^-) than the glutathionyl (GS^-) ligand on preparation energy.

The interaction energy between the two fragments can be partitioned between three terms $E_{INT} = E_{ES} + E_{EX} + E_{ORB}$

where E_{ES} is the electrostatic interaction energy, E_{EX} is the Pauli repulsion and exchange energy, and E_{ORB} is the orbital interaction energy which includes charge transfer and electronic polarization energy, E_{EPL}. Thus $E_{ORB} = E_{CT} + E_{EPl}$. With the calculated value E_{ORB} = -152.6 kcal/mol, the difference, $E_{INT} - E_{ORB} = E_{steric}$ = -113.93 kcal/mol which is the so-called steric interaction energy, i.e., $E_{steric} = E_{ES} + E_{EX}$. Since the CH3- fragment has a -1 charge and the Co-Corrin-Im^{2+} has a 2+ charge, there must be a large electrostatic attraction which should dominate the steric interaction energy. The orbital interaction energy which is 57% of the total interaction energy contains the bond stabilization due to CT and the electronic polarization between the fragments. From the above extended charge decomposition analysis, the CT is 0.761 electrons which should come from the axial Cax atom donation to the Co ion.

Table 2.6 Charge Decomposition Analysis of the Me-Co-Corr-Im with Me- as Fragment 2 and the Rest (Co-Corr-Im) of the Molecule as Fragment 1 for Major Contributions.

α-spin MO	Donation 2→ 1	Back donation 1→ 2	Repulsion	Residue Δ term
HOMO-6 (#111)	0.005	0.001	-.008	0.000
HOMO-5 (#112)	0.001	0.007	-.011	0.000
HOMO-4 (#113)	0.063	0.005	-.016	0.002
HOMO-3 (#114)	0.001	0.000	-.001	0.000
HOMO-2 (#115)	0.004	0.004	-.002	0.000
HOMO-1 (#116)	0.000	0.001	-.001	0.000
HOMO (#117)	0.056	0.005	-.079	0.000
Sum over α- MOs	0.146	0.025	-	-
Total α + β	0.291	0.051	-0.174	-0.000

a. Total over occupied MOs

The generalized Mayer bond order between fragment 1 and fragment 2 is 1.02. In a four fragment calculation the bond order between the methyl group and cobalt is 0.9. If the bond order comes primarily from the β-axial ligand atom attached to Co, then the C-Co bond order is closest to a pure covalent sigma organo-metallic bond. The Wiberg bond index (Table 2.14) in the NAO basis for Co-C_{ax} is 0.78 compared to the value of 0.68 for the Co-S_{ax}. This bond index is 0.195 (Table 2.6) for the Co-Oax. Again this shows similar covalent character of the Co-C and Co-S bonds.

2.2.4 Natural Bond Order Analysis of R-Cbls

2.2.4.1 NBO Analysis of GS-Cbl

The Natural Bond Order (NBO) analysis (26) was made for two molecular structures, GS-Co(III)-corr-Im and GS-Co(III)-corr-Bz, with different calculation models (Table 2.7). We examined the NBO analysis for the effect of solvent, changing the axial base, the basis set, and the density functional. Models A through D were made with the B3LYP hybrid density functional while models E and F were made with BP86. Only model A had imidazole, the rest had the 5,6dimethylbenzimidazole base, Bz. Most of the models were optimized with the basis set 6-311G (d,p); however, for two models B and C the smaller 6-31G (d,p) basis set was used which had an effect in the NBO analysis. Thus six models were taken for NBO analysis: GS-Co(III)-corr-Im in vacuum at B3LYP/6-311G(d,p) (A), GS-Co(III)-corr-Bz in vacuum (B) and water environment (C) both at B3LYP/6-31G(d,p) level, GS-Co(III)-corr-Bz in aqueous solution at the

B3LYP/6-311G(d,p) level(D), and GS-Co(III)-corr-Bz with BP86/6-311G(d.p in vacuum (E) and in aqueous solution (F) (cpcm). Table 2.7 shows the natural electronic configuration for Co and the σ natural bond orbitals.

The NBO natural population analysis for the six calculations gives similar natural Lewis population in the valence orbitals of between 99.600 % and 99.645 %. It is interesting, as seen in Table 2.7, that the gross natural electron configuration for Co is very similar for models A, D, E, and F at 6-311G(d,p) but different for models B and C calculated with 6-31G(d,p). In model B 0.57 e population is in the 4p natural atomic orbitals while in model C 0.57 e is in 4p ; whereas, there is virtually no occupation of 4p in the other model calculations. It turns out that models A and D made with the same DFT and basis set show very similar NBO results even though the axial base and environment were varied. In models A and D (Table 2.7), the NHO on Co is almost exactly sd^2 whereas in model B and C using the smaller basis set it is close to sp^3d^2. The occupancy of all the σ bond orbitals in Table 2.7 is from 1.91e to 1.94e whereas their antibonding pairs show 0.3e indicating considerable delocalization of the bond electron density. It is seen (Table 2.7) that model A and D show three σ natural bond orbitals between Co and a bonding atom, whereas models B and C have five such NBO bonds, and models E and F show only one NBO involving Co. The optimized canonical MO structure has six σ bonds between Co and the coordinating ligand so the bonds which do not show up in the NBO analysis are formed by donor –acceptor interactions into the anti-bond non-Lewis orbitals.

We first discuss the NBO analysis of model A which has the imidazole base. In terms of a Lewis localized bond orbital perspective, the NBO description of model A

shows that there are three two-centered/ two electron σ bonds (BD) (2c/2e) for N_{23}-Co, N_{24}-Co, and S_{ax}-Co . Also the other two nitrogens in the corrin ring as-well-as the axial nitrogen have almost fully occupied lone pairs (LP), N_{21}(1.71), N_{22}(1.71), N_{ax}(1.79). These three LPs which form dative bonds with the Co are in line with the above σ bonds, i.e. N_{23}-Co-N_{21}, N_{24}-Co-N_{22}, S_{ax}-Co-N_{ax} (see Fig. 1.1). The Co itself shows 3 LPs with 1.92 to 1.97 occupancy which are pure d orbitals and are not ostensibly involved in bonding. The three σ 2c/2e bonds can be considered as "prebonds" for forming the so-called hypervalent ω-bond with the three lone pair nitrogens which are directly across the Co from each bond (27). Thus three centered/four electron (3c/4e) localized ω-bonded natural localized molecular orbitals (NLMOs) are formed as N_{23}-Co:N_{21}, N_{24}-Co:N_{22}, S_{ax}-Co:N_{ax}. Each of these 3c/4e bonds would have a resonance form N_{23}:Co-N_{21}, N_{24}:Co-N_{22}, and S_{ax}:Co-N_{ax}, so in this resonance form N_{21},N_{22}, and N_{ax} LPs would form the (BD) 2c/2e "prebond" orbitals to the cobalt. This is the bonding picture stressed by Weinhold and Landis (27).

The Co hybrid orbital is $sd^{1.95,}$ almost exactly sd^2, which has 90^o angles and the nitrogen corrin ring hybrid orbitals bonding to Co are $sp^{3.3}$ which is close to sp^3 hybridization. This shows that the coordinate covalent bond is not planar with sp^2 nitrogen NHOs in the pyrrole rings. The MO optimized structure in model A formed between Co and its equatorial and axial bonding partners is not too far from octahedral coordination geometry with bond angles that are about 88^o for the N_{eq}-Co-S_{ax} bond angle and 173^o for the N_{eq}-Co-N_{eq} and 177^o for the N_{ax}-Co-S_{ax} bond angles. As seen in Table 2.1 this is similar for all the optimized structures.

We also note that the second order perturbation theory analysis of the Fock (Kohn-Sham) matrix in the NBO basis (28) further substantiates this bonding picture for model A. A filled donor type Lewis NBO (BD or LP) can donate charge to an acceptor type non-Lewis NBO (BD* or LP*) which stabilizes the energy of the filled NBO leading to the ω-bonding. Large values of this stabilization energy, E_2, are found for the lone pairs involved in the coordinate covalent bonding, i.e., for LP donor → acceptor BD* type donation. Thus for LP N_{21}→BD* Co-N_{23}, E_2 is 64.66 kcal/mol; for LP N_{22}→BD* Co-N_{24}, E_2 is 65.31 kcal/mol, and for LP N_{ax} →BD* Co-$S_{ax,}$ E_2 is 42.78 kcal/mol. This stabilization indicates delocalized population across the 3c/4e ω-bonds. Also the stabilization energy for BD Co-S_{ax}→ BD* Co-N_{24} is 23.51 kcal/mol, BD Co-S_{ax}→ BD* Co-N_{23} is 23.51 kcal/mol, and BD Co-S_{ax}→ BD* Co-S_{ax} is 15.88 kcal/mol, indicating delocalization stabilization by donation from the Co-S bond to the Co-N_{eq} NBOs and to its own antibonding NBO. There are two LPs on the S_{ax}, LP 1(1.97) which is which $sp^{0.27}$ and a second LP 2 (1.94) which is a pure $3p_y$ NHO. These LPs are not involved with a donor to acceptor stabilization on Co.

However, a somewhat different picture of the bonding comes from the NBO analysis of model B for GS-corrin-Bz in vacuum (Table 2.7) made with the smaller double-ζ basis set 6-31G(d,p). Now five σ "prebond" bonds are found. Four involve the equatorial bonds and the fifth involves the Co-S axial bond. Four bonding Co hybrids with $sp^{3.3}d^{2.3}$ NHOs combine with four equatorial corrin ring $sp^{2.4}$ pyrrole nitrogens to give four σ bonding localized NBOs (Table 2.7) for the square planar geometry of the corrin macrocyle. The four NHO Co $sp^{3.3}d^{2.3}$ orbitals show small absolute average deviation of the exponents, but they are close to the sp^3d^2 valence bond hybrid orbital

giving octahedral geometry for Co. There are similar small deviations of the exponents in the four N_{eq} $sp^{2.4}$ orbitals which are close to a sp^2 valance bond N hybrid orbital and coordinate with the Co. Again there are three Co lone pairs not involved in bonding which are pure d NAOs with occupancies of 1.916, 1.935, and 1.958. Table 2.7 model B also shows that different NHOs are involved in the Co-S σ bond which is the $\sigma = 0.55(sp^{0.4}d^{1.8})_{Co} + 0.83(s^{0.11}p^{.88})_{Sax}$. Here we have a Co hybrid orbital which is almost sd^2 mixed with some p character interacting with almost a pure $3p_z$ natural atomic orbital on sulfur.

On the other hand, no other bonding orbital is found for the Co-N_{ax} bond which comes from the 5, 6-dimethylbenzimidazole base model B and C. The only way to account for this bond in the NBO analysis is from delocalization of the lone pair on the N_{ax} atom to the Co. Thus we find a large stabilization energy in the second order perturbation theory analysis of the Fock (Kohn-Sham) matrix in the NBO basis for the LP $N_{ax} \rightarrow$ LP* Co of 77.08 kcal/mol for model B. Also we find E_2 for LP $N_{ax} \rightarrow$ BD* Co-S of 11.13 kcal/mol. From the NBO point of view this would indicate that the α-axial Co-N bond is formed by donation of electron density from the N_{ax} lone-pair into a delocalized *non-Lewis* LP* Co orbital and into the BD* Co-S antibond giving the S_{ax}-Co:N_{ax} 3c/4e hypervalent ω bond. The axial S atom also has two LPs, LP 1(1.94) which is pure $3p_y$ and a second LP 2 (1.91) which is a $sp^{0.41}$ NHO. Furthermore, a stabilization energy of 34.55 kcal/mol is found for the LP 2 $S_{ax} \rightarrow$ LP* Co donor/acceptor delocalization. This type of stabilization was not found in model A. Thus the second order perturbation analysis shows considerable delocalization across the S_{ax}-Co-N_{ax} axis in the model B calculation at the 6-31G (d,p) level.

Model C which has the same chemical structure and basis set as model B but is calculated with the cpcm water model rather than in vacuum gives almost exactly the same NBO analysis as model B in vacuum. Furthermore model A and model D made at the same B3LYP/G-311G (d,p) level have the same NBO bonding analysis even though the axial base and solvent environment are different. Thus it is not the solvent environment nor the change to the larger Bz base that causes the Co NHO to go from sd^2 to a sp^3d^2 type NHO but rather it seems to be the change to the smaller 6-31G (d,p) basis set which indicates population in the 4p atomic orbitals on Co.

As mentioned above with BP86/6-311G(d,p), models E and F, only one Lewis type NBO is found in the NBO analysis whether in vacuum or with cpcm. For the water case E, this is the $\sigma=0.60(sp^{0.06}d^{.94})_{Co} + 0.80(s^{0.05}p^{0.95})_{Sax}$ for the Co-S_{ax} bond. The vacuum calculation E shows nearly the same BD bond orbital (Table 2.7). The coordinate covalent bonds between Co and the equatorial and axial nitrogens must be so polarized towards the nitrogen lone pairs that the do not show up as Lewis type NBOs. However, the second order perturbation energy E_2 shows large values for each pyrrole ring nitrogen lone pair donation to two antibonding LP* acceptors on Co, LP Neq $\rightarrow$ LP* Co. In model E (cpcm case), the stabilization energy E_2 is 27 and 38 kcal/mol for the first and second donation for each nitrogen in the five-membered ring (N_{21} and N_{24})and 30 and 41 kcal/mol for each nitrogen in the six-membered ring (N_{22} and N_{23}) . Similar values are found for the vacuum case E. For the axial nitrogen lone pair on Bz, there is one LP N_{ax} $\rightarrow$ LP* Co donation with 25 kcal/mol E_2 for both water and vacuum cases and one LP N_{ax} $\rightarrow$ BD* Co-S of 35 kcal/mol for water case and 32 kcal/mol for the vacuum case. The water dielectric appears to very slightly stabilize this Co-N_{ax} bond. Also in both model D

and E, the three pure 3d NAOs on the cobalt lone pairs are again nearly fully occupied with occupancy from 1.83 to 1.96. In both the vacuum (E) and water (F) cases, the S_{ax} atom also has two LPs which are LP 1(1.97) with NHO $sp^{0.25}$ and LP 2 (1.94) with a pure 3p NAO. The LP 1 on S_{ax} donates charge to LP* 5 on Co, i.e., LP 1 $S_{ax} \rightarrow$ LP* 5 Co with stabilization energies of 25.51 kcal/mole for vacuum and 23.80 kcal/mole for water. A similar stabilization was found with models B and C and this seem to indicate a π bonding interaction between the lone pair on S_{ax} and a d_{π} orbital on Co.

In fact, symmetry considerations allow us to predict the atomic orbitals which will be involved in the hybrid orbitals. Tetragonal distortion of six-coordinate geometry takes symmetry O_h to C_{4v} (29). The local symmetry for GS-Cbl around the central Co is C_{4v}. This means that the six σ bonds have a reducible representation which reduces as $\Gamma_{\sigma} = 3A_1+B_1 + E$. Thus the hybrid bonding orbitals can only involve combinations of possible NAO from the set: $A_1(s, p_z, d_{z2})$, $B_1(d_{x2-y2})$, and E (p_x, p_y and d_{xy}, d_{yz}). Here d_{xy} which has B_2 symmetry is a nonbonding orbital. In model A, the sd^2 NHO on the Co should involve the 4s, $3d_{z2}$, and $3d_{x2-y2}$ orbitals. In models B and C, the sp^3d^2 NHO on the Co should involve the 4s, $4p_x$, $4p_y$, $4p_z$, $3d_{z2}$, and $3d_{x2-y2}$ orbitals. The NHO on the ligand N atoms binding to Co are sp^2 or sp^3 and NHO in the ligand S_{ax} σ bond is almost pure p_z. These NHOs should come from A_1 and E symmetry orbitals. Models E and F show almost a pure $3d_{z2}$ on Co bonding to $3p_z$ on S_{ax}. In every model in Table 2.7, there is 1.8 to 1.9 occupation of the three lone pairs on Co. The three Co lone pairs should come from the $3d_{xy}$, $3d_{xz}$, and $3d_{yz}$ Co atomic orbitals. The antibond d orbitals through delocalization could enter into π bonding with one of the S_{ax} lone pairs in the NBO picture.

The polarization coefficients for all the Co-N_{eq} natural localized hybrid bond orbitals in Table 2.7 in all models are very similar being around 0.39 for the Co hybrid and around 0.92 for the N_{eq} hybrid. With $100|c_A|^2$ being the percentage of the NBO on each hybrid, this gives around 15 % on the Co NHO and 85% on the N_{eq} NHO. Thus most of the population is on the equatorial nitrogens indicating coordinate covalent bonding with the bond heavily polarized towards the pyrrole nitrogen. Although all the models show somewhat different NHO on Co for the Co-S bond, all of the polarization coefficients are very similar. Thus for the Co-S_{ax} bond the polarization coefficients give around 29% on the NHO of the Co and around 71 % on the NHO of the S_{ax}. Because of the CT from the sulfur this bond is less polarized than the Co-N equatorials bonds.

The localized NBO analysis of the Wiberg bond index in the natural atomic orbital (NAO) basis (Table 2.8) illustrates that the bond indexes in models A (B3LYP in vac), D (B3LYP with cpcm) and F (BP86 with cpcm) all at the larger 3-ζ basis set 6-311G(d,p) are more similar than for model C (B3LYP/6-31G(d,p) with cpcm). The Wiberg bond indices, W_{AB}, in the NBO output come from the density matrix in the NAO basis. Here WB_{AB} are the sum of the squares of the off-diagonal density matrix elements between atoms (30)

$$W_{AB} = \sum_{a \in A} \sum_{b \in B} (P_{ba})^2 = 2P_{jj} - P_{jj}^2 \qquad (2)$$

which is equal to twice the charge density in the atomic orbitals P_{jj} minus the square of the charge density. The Wiberg bond index is suitable for the orthogonal NAO since it does not contain the overlap integral which is in the Mayer bond index, B_{AB}, in equation (1). Model A calculated in vacuum with imadazole shows a lower bond index for the Co-N_{ax} bond compared with the other models which were for the Bz base. For all four

models the bond indexes for Co-N_{23} and Co-N_{22} which are in the 5-membered ring with Co are very close in value and like-wise for the Co-N_{24} and Co-N_{22} which are in the 6-membered ring with Co. Model C show a conspicuously higher indexes for all the bonds. These latter bond indexes have the largest values across all models when compared for the Co-N bonds. The Wiberg bond index for the S_{ax}-Co bond is almost twice that of the other bond indexes in Table 2.8 indicating that it is much more covalent than the equatorial and axial Co-N bonds which are dative in character.

Table 2.9 shows a comparison of Wiberg Bond index total by atoms with the Mulliken and natural atomic charge for the three types of calculations. The models give similar Wiberg Bond index total by atoms except that of model F which shows a higher index for Co. In terms of charge on the atoms, the main difference across the models is that more charge is donated to Co ion in model F as reflected by the lower charge on the Co both in the Mulliken and natural atomic charge analysis in this calculation. The lower negative charge on S_{ax} atom also indicates the charge transfer of electron density to the Co.

Table 2.7 Natural Electronic Configuration for the Co ion in model for GS-Cbl calculations and hybrid natural bond orbitals for Co-N_{eq} and Co-S_{ax}

(A) GS-Co(III)-corr-Bz^+ B3LYP/6-311G(d.p), vac	Co[core]4s(0.29)3d(7.47)4p(0.02)5s(0.01)	$\sigma = 0.40(sd^{1.95})_{Co} + 0.92(sp^{3.27})_{N23}$ $\sigma = 0.40(sd^{1.94})_{Co} + 0.92(sp^{3.30})_{N24}$ $\sigma = 0.56sd^{2.26})_{Co} + 0.83(s^{0.05}p^{.95})_{Sax}$
(B) GS-Co(III)-corr-Bz^+ B3LYP/6-31G(d.p), vac	Co[core]4s(0.33)3d(7.25)4p(0.57)	$\sigma = 0.37(sp^{3.36}\, d^{2.24})_{Co} + 0.93(sp^{2.43})_{N21}$ $\sigma = 0.39(sp^{3.18}\, d^{2.26})_{Co} + 0.92(sp^{2.52})_{N23}$ $\sigma = 0.38(sp^{3.29}\, d^{2.27})_{Co} + 0.93(sp^{2.44})_{N24}$ $\sigma = 0.37(sp^{3.19}\, d^{2.21})_{Co} + 0.93(sp^{2.43})_{N22}$ $\sigma = 0.55(sp^{0.41}d^{1.76})_{Co} + 0.83(s^{0.11}p^{.88})_{Sax}$
(C) GS-Co(III)-corr-Bz^+ B3LYP/6-31G(d.p), cpcm	Co[core]4s(0.33)3d(7.24)4p(0.58)	$\sigma = 0.39(sp^{3.36}\, d^{2.40})_{Co} + 0.92(sp^{2.48})_{N21}$ $\sigma = 0.37(sp^{3.31}\, d^{2.26})_{Co} + 0.93(sp^{2.45})_{N23}$ $\sigma = 0.39(sp^{3.29}\, d^{2.27})_{Co} + 0.92(sp^{2.44})_{N24}$ $\sigma = 0.37(sp^{3.41}\, d^{2.34})_{Co} + 0.93(sp^{2.44})_{N22}$ $\sigma = 0.53(sp^{0.47}d^{1.70})_{Co} + 0.85(s^{0.12}p^{.87})_{Sax}$
(D) GS-Co(III)-corr-Bz^+ B3LYP/6-311G(d.p), cpcm	Co[core]4s(0.28)3d(7.45))5s(0.01)	$\sigma = 0.40(sd^{1.94})_{Co} + 0.92(sp^{3.34})_{N23}$ $\sigma = 0.40(sd^{1.94})_{Co} + 0.92(sp^{3.34})_{N24}$ $\sigma = 0.52sd^{2.17})_{Co} + 0.85(s^{0.05}p^{.95})_{Sax}$
(E) GS-Co(III)-corr-Bz^+ BP86/6-311G(d.p), vac	Co[core]4s(0.29)3d(7.56)5s(.01)	$\sigma = 0.62(s^{0.05}d^{.94})_{Co} + 0.79(s^{0.04}p^{.96})_{Sax}$
(F) GS-Co(III)-corr-Bz^+ BP86/6-311G(d.p), cpcm	Co[core]4s(0.29)3d(7.56)5s(0.01)	$\sigma = 0.60(s^{0.06}d^{.94})_{Co} + 0.80(s^{0.05}p^{0.95})_{Sax}$

Table 2.8 Wiberg Bond Indexes for GS-Cbl models in NAO Basis

Bond	(A)GS-Co(III)-corr-Im^+ B3LYP/6-311G(d.p), vac	(GS-Co(III)-corr-Bz^+ B3LYP , cpcm (C) 6-31G**	(D) 6-311G**	(F) GS-Co(III)-corr-Bz^+ BP86/6-311G(d.p), cpcm
Co-N_{23}	0.347	0.478	0.349	0.377
Co-N_{21}	0.390	0.514	0.387	0.424
Co-N_{24}	0.386	0.514	0.388	0.424
Co-N_{22}	0.351	0.478	0.346	0.375
Co-N_{ax}	0.202	0.378	0.239	0.250
Co-S_{ax}	0.682	0.874	0.619	0.634

Table 2.9 Wiberg Bond Index(BDIX) Total by Atom and Mulliken (Natural) Atomic Charges. (A) GS-corrin-Im, B3LYP/6-311G(d.p), vac. (B) GS-Co-corrin-Bz B3LYP/6-311G(d.p), cpcm. (C) GS-Co-corrin-Bz BP86/6-311G (d.p), cpcm.

Atoms	Wiberg BDIX Total (A)	Wiberg BDIX Total (D)	Wiberg BDIX Total (F)	Mulliken (Natural) Charge (A)	Mulliken (Natural) Charge (D)	Mulliken (Natural) Charge (F)
Co	2.73	2.70	3.10	1.26 (1.21)	1.29 (1.26)	1.21 (1.14)
N_{23}	3.23	3.24	3.30	-0.578 (-0.594)	-0.571 (-0.591)	-0.526 (-0.545)
N_{21}	3.27	3.28	3.34	-0.544 (-0.548)	-0.549 (-0.546)	-0.505 (-0.505)
N_{24}	3.28	3.29	3.34	-0.547 (-0.552)	-0.545 (-0.546)	-0.503 (-0.506)
N_{22}	3.24	3.23	3.29	-0.575 (-0.592)	-0.581(-0.598)	-0.537 (-0.553)
N_{ax}	3.18	3.19	3.23	-0.440 (-0.558)	-0.533 (-0.571)	-0.511 (-0.542)
S_{ax}	2.02	1.95	2.03	-0.267 (-0.239)	-0.362 (-0.328)	-0.297 (-0.254)

2.2.4.2 NBO of H2O-Cbl

The NBO analysis (24) for aquocobalamin was made for only one molecular structure, H2O-Co(III)-corr-Im (Table 2.10). The model was taken for NBO analysis: GS-Co(III)-corr-Im in water environment at B3LYP/6-311G(d,p) level, (cpcm). Table 2.10 shows the natural electronic configuration for Co and the σ natural bond orbitals.

The NBO natural population analysis for the calculation gives natural Lewis population in the valence orbitals of 99.6275 %. Table 2.10 shows 4s(0.27)3d(7.37)4p(0.02)5s(0.01) natural atomic orbital population in the Co valence shell. There is virtually no occupation of 4p as found in the calculations at B3LYP/6-31G (d,p) for GS-Cbl models. The NHO on Co is almost exactly sd^2 and the occupancy of all the σ bond orbitals in Table 2.10 is from 1.91e to 1.94e whereas their antibonding pairs show about 0.3e indicating considerable delocalization of the bond electron density. The optimized canonical MO structure has six σ bonds between Co and the coordinating ligand so the bonds which do not show up in the NBO analysis are formed by donor – acceptor interactions into the anti-bond non-Lewis orbitals.

We discuss the NBO analysis for a model which has the imidazole base. In terms of a Lewis localized bond orbital perspective, the NBO description of the model shows that there are three two-centered/ two electron σ bonds (BD) (2c/2e) for N_{23}-Co, N_{24}-Co, and N_{ax}-Co . Also the other two nitrogens in the corrin ring as-well-as the axial nitrogen have almost fully occupied lone pairs (LP), N_{22}(1.682), N_{23}(1.679). These two LPs which form dative bonds with the Co are in line with the above σ bonds, i.e. N_{23}-Co-N_{21}, N_{24}-Co-N_{22}, (see Fig. 1). The Co itself shows 3 LPs with 1.951 to 1.978 occupancy which are pure d orbitals and are not ostensibly involved in bonding. The three σ 2c/2e bonds can be considered as "prebonds" for forming the so-called hypervalent ω-bond with the three lone pair nitrogens which are directly across the Co from each bond (27). Thus two centered/four electron (3c/4e) localized ω-bonded NLMOs are formed as N_{23}-Co:N_{21}, N_{24}-Co:N_{22}. Each of these 3c/4e bonds would have a resonance form N_{23}:Co-N_{21}, N_{24}:Co-N_{22}, so in this resonance form N_{21},N_{22}, and N_{ax} LPs would form the (BD) 2c/2e

"prebond" orbitals to the cobalt. Again this is the bonding picture stressed by Weinhold and Landis (27).

The Co hybrid orbital is $sd^{1.95}$ almost exactly sd^2, which has 90^o angles and the nitrogen corrin ring hybrid orbitals bonding to Co are $sp^{3.3}$ which is close to sp^3 hybridization. This shows that the coordinate covalent bond is not planar with sp^2 nitrogen NHOs in the pyrrole rings. The MO optimized structure in the model formed between Co and its equatorial and axial bonding partners is not too far from octahedral coordination geometry with bond angles that are about 87^o for the N_{eq}-Co-O_{ax} bond angle and 172^o for the N_{eq}-Co-N_{eq} and 177^o for the N_{ax}-Co-O_{ax} bond angles.

We also note that the second order perturbation theory analysis of the Fock (Kohn-Sham) matrix in the NBO basis (28) further substantiates this bonding picture for the model. A filled donor type Lewis NBO (BD or LP) can donate charge to an acceptor type non-Lewis NBO (BD* or LP*) which stabilizes the energy of the filled NBO leading to the ω-bonding. Large values of this stabilization energy, E_2, are found for the lone pairs involved in the coordinate covalent bonding, i.e., for LP donor $\rightarrow$ acceptor BD* type donation. Thus for LP $N_{23}\rightarrow$BD* Co-N_{21}, E_2 is 69.17 kcal/mol; for LP $N_{22}\rightarrow$BD* Co-N_{24}, E_2 is 68.55 kcal/mol. This stabilization indicates delocalized population across the 3c/4e ω-bonds. Also the stabilization energy for BD Co-$O_{ax}\rightarrow$ BD* Co-N_{24} is 23.51 kcal/mol, BD Co-$O_{ax}\rightarrow$ BD* Co-N_{23} is 23.51 kcal/mol, and BD Co-$O_{ax}\rightarrow$ BD* Co-O_{ax} is 15.88 kcal/mol, indicating delocalization stabilization by donation from the Co-O bond to the Co-N_{eq} NBOs and to its own antibonding NBO. There are two LPs on the O_{ax}, LP 1(1.97) which is which $sp^{0.27}$ and a second LP 2 (1.94) which is a pure $3p_y$ NHO. These

LPs are not involved with a donor to acceptor stabilization on Co as found with GS-ligand.

The polarization coefficients for all the Co-N_{eq} natural localized hybrid bond orbitals in Table 2.10 in the model is close to 0.43 for the Co hybrid and around 0.91 for the N_{eq} hybrid. With $100|c_A|^2$ being the percentage of the NBO on each hybrid, this gives around 18 % on the Co NHO and 82% on the N_{eq} NHO. Thus most of the population is on the equatorial nitrogens indicating coordinate covalent bonding with the bond heavily polarized towards the pyrrole nitrogen. All of the polarization coefficients are very similar. Thus for the Co-O_{ax} bond the polarization coefficients give around 19 % on the NHO of the Co and around 81 % on the NHO of the O_{ax}.

The localized NBO analysis of the Wiberg bond index in the natural atomic orbital (NAO) basis (Table 2.11) illustrates the bond indexes for the model. The Wiberg bond indices, W_{AB}, in the NBO output come from the density matrix in the NAO basis, equation (2). The model calculated in vacuum with imadazole shows a higher bond index (0.473) bond index for the Co-N_{ax} bond compared with the GS-Co-corr-Im in vacuum model (0.202). The bond indexes for Co-N_{23} and Co-N_{22} which are in the 5-membered ring with Co are very close in value and like-wise for the Co-N_{24} and Co-N_{22} which are in the 6-membered ring with Co. The Wiberg bond index for the O_{ax}-Co (0.195) is much smaller that of the other bond indexes for the Co-Sax (0.682) in Table 2.8 and for Co-Cax (0.77) in Table 2.14 indicating that its much less covalent character than ligand bond.

Table 2.12 shows a comparison of Wiberg Bond index total by atoms with the Mulliken and natural atomic charge for the model. In terms of the charge on the atoms, the main difference is reflected in the higher charge on the O (-.876) in the natural charge

analysis than in the Mulliken charge analysis (-.471). This is consistent with the higher bond indexes for the Co-O bond in the Mayer bond order (0.257) than in the Wiberg bond order (0.20).

Table 2.10 Natural Electronic Configuration for the Co ion in model calculations of Aquo-Cbl and hybrid natural bond orbitals for Co-N_{eq} and Co-O_{ax}

(A) Aq-Co-corrin-Im B3LYP/6-311G(d.p), vac	Co[core]4s(0.27)3d(7.37)4p(0.02)5s(0.01)	$\sigma = 0.42(sd^{2.21})_{Co} + 0.91(sp^{3.28})_{Nax}$ $\sigma = 0.43(sd^{1.94})_{Co} + 0.91(sp^{3.54})_{N23}$ $\sigma = 0.43(sd^{1.93})_{Co} + 0.90(sp^{3.54})_{N24}$

Table 2.11 Wiberg Bond Index in NAO Basis

Bond	A) Aq-corrin-Im B3LYP/6-311G(d.p), vac
Co-N_{23}	0.3594
Co-N_{21}	.4229
Co-N_{24}	.4209
Co-N_{22}	.3595
Co-N_{ax5}	.4727
Co-O_{ax1}	.1949

Table 2.12 Wiberg Bond Index(BDIX) Total by Atom and Mulliken (Natural) Atomic Charges. (A) GS-corrin-Im, B3LYP/6-311G(d.p), vac. (B) GS-Co-corrin-Bz B3LYP/6-311G(d.p), cpcm. (C) GS-Co-corrin-Bz BP86/6-311G (d.p), cpcm

Atoms	Wiberg BDIX Total (A)	Mulliken (Natural)Charge (A)
Co	2.59	1.36 (1.34)
N_{23}	3.23	-0.625 (-0.620)
N_{21}	3.29	-0.572 (-0.562)
N_{24}	3.30	-0.565 (-0.550)
N_{22}	3.23	-0.607 (-0.613)
N_{ax5}	3.33	-0.454 (-0.506)
O_{ax1}	1.75	-0.471 (-0.876)

2.2.4.3 NBO of Me-Cbl

The NBO analysis (26) was made one molecular structure, Me-Co(III)-corr-Im^+ (Table 2.13). The model was taken for NBO analysis was Me-Co(III)-corr-Im in a water environment at B3LYP/6-31G(d,p) level, (cpcm). Table 2.13 shows the natural electronic configuration for Co and the σ natural bond orbitals.

The NBO natural population analysis for the calculation gives natural Lewis population in the valence orbitals of 99.6184%. In the model only 0.02e population is in the 4p natural atomic orbitals and only 0.01 in 5s. The NHO on Co is almost pure d. The occupancy of the σ bond orbitals in Table 2.13 is 1.99e whereas the antibonding pair shows 0.24773e indicating considerable delocalization of the bond electron density. The optimized canonical MO structure has six σ bonds between Co and the coordinating ligand so the bonds which do not show up in the NBO analysis are formed by donor – acceptor interactions into the anti-bond non-Lewis orbitals.

We discuss the NBO analysis for a model which has the imidazole base. There is only one 2c/2e σ bond found in the NBO analysis for the Co-Cax bond. The Co hybrid orbital is $s^{0.05}d^{0.95}$ which is almost pure d and the nitrogen corrin ring hybrid orbitals bonding to Co are $sp^{4.8}$. However, the MO optimized structure in the model formed between Co and its equatorial and axial bonding partners is not too far from octahedral coordination geometry with bond angles that are about 90^o for the N_{eq}-Co-C_{ax} bond angle and 173^o for the N_{eq}-Co-N_{eq} and 177^o for the N_{ax}-Co-C_{ax} bond angles.

The other covalent coordinate bonds are indicated by the Perturbation analysis. Thus the second order perturbation theory analysis of the Fock (Kohn-Sham) matrix in

the NBO basis (28) substantiates this bonding picture for the model. A filled donor type Lewis NBO (BD or LP) can donate charge to an acceptor type non-Lewis NBO (BD* or LP*) which stabilizes the energy of the filled NBO leading to the ω-bonding. Large values of this stabilization energy, E_2, are found for the lone pairs involved in the coordinate covalent bonding, i.e., for LP donor → acceptor BD* type donation. Thus for LP N_{23}→BD* Co-N_{21}, E_2 is 69.17 kcal/mol; for LP N_{22}→BD* Co-N_{24}, E_2 is 68.55 kcal/mol. This stabilization indicates delocalized population across the 3c/4e ω-bonds. Also the stabilization energy for BD Co-S_{ax}→ BD* Co-N_{24} is 23.51 kcal/mol, BD Co-S_{ax}→ BD* Co-N_{23} is 23.51 kcal/mol, and BD Co-S_{ax}→ BD* Co-S_{ax} is 15.88 kcal/mol, indicating delocalization stabilization by donation from the Co-S bond to the Co-N_{eq} NBOs and to its own antibonding NBO. There are two LPs on the S_{ax}, LP 1(1.97) which is which $sp^{0.27}$ and a second LP 2 (1.94) which is a pure $3p_y$ NHO. These LPs are not involved with a donor to acceptor stabilization on Co.

The polarization coefficients for the Co-C_{ax} natural localized hybrid bond orbitals are in Table 2.13 in the model is 0.67 for the Co hybrid and 0.75 for the C_{ax} hybrid. With $100|c_A|^2$ being the percentage of the NBO on each hybrid, this gives around 45 % on the Co NHO and 55% on the C_{ax} NHO. Thus for the Co-C_{ax} bond the polarization coefficients are quite similar indicating the covalent nature of the bond.

The localized NBO analysis of the Wiberg bond index in the natural atomic orbital (NAO) basis (Table 2.14) illustrates that the bond indexes in the model The Wiberg bond indices, W_{AB}, in the NBO output comes from the density matrix in the NAO basis. The Wiberg bond index is suitable for the orthogonal NAO since it does not contain the overlap integral which is in the Mayer bond index, B_{AB}, in equation (1).

Model A calculated in vacuum with imadazole shows a lower bond index for the Co-N_{ax} bond compared with the other R-ligand models. The value for the bond index of Co-Cax is the largest of three indexes and again indicator of the covalent bond. Table 2.15 shows the Wiberg bond indexes total and Mulliken, and Natural charges.

Table 2.13 Natural Electronic Configuration for the Co ion and hybrid natural bond orbitals for Me-Co-corr-Im.

(A) Me-Co-corrin-Im B3LYP/6-311G(d.p), vac	Co[core]4s(0.01)3d(7.52)4p(0.02)5s(0.27)	$\sigma = 0.67(s^{0.05}d^{0.95})_{Co} + 0.75(sp^{4.812})_{Cax}$

Table 2.14 Wiberg Bond Index in NAO Basis for Me-Cbl model.

Bond	A) Me-corrin-Im B3LYP/6-311G(d.p), vac
Co-N_{23}	.3423
Co-N_{21}	.3863
Co-N_{24}	.3850
Co-N_{22}	.3438
Co-N_{ax}	.1304
Co-C_{ax}	.7767

Table 2.15 Wiberg Bond Index (BDIX) Total by Atom and Mulliken (Natural) Atomic Charges for Me-Co-corr-Im.

Atoms	Wiberg BDIX Total (A)	Mulliken (Natural) Charge (A)
Co	2.79	1.25 (1.19)
N_{23}	3.24	-0.566 (-0.581)
N_{21}	3.28	-0.530 (-0.535)
N_{24}	3.28	-0.527 (-0.536)
N_{22}	3.24	-0.564 (-0.576)
N_{ax6}	3.12	-0.418 (-0.572)
C_{ax11}	3.85	-0.557 (-0.763)

2.3. Summary and Conclusions

We first consider geometry calculation for the three molecules. Bond distances and bond angles do not depend greatly on basis set or vacuum/water solvent effect or the effect of changing from imidazole to 5,6- dimethylbenzimidazole axial base. Thus there is no ststistical difference between models. For glutathiony-cobalamin the geometric optimizations accurately reflect the structural features such as the axial and equatorial cobalt-ligand bond distances and the fold angle. Here, geometric optimizations made in vacuum show a better fit to the X-ray crystal structure with respect to bond distances which may be reflecting the real differences between the solid and solution states.

Various energies from the energy decomposition analysis for the models of the three molecules are given in Table 2.16. All values necessary for the calculations of energies in Table 2.16 are given in Table 2.17. The R-Co-corr-Im models for Me-Cbl and GS-Cbl show roughly ten times the interaction energy of H2O-Cbl. It is also seen from

the table that orbital energy which is related to the covalent character of the bond is much greater for the GS-Cbl and Me-Cbl that for the H2OCbl. Furthermore the steric energy contains the electrostatic interaction component of the bond energy and the Pauli repulsion component. The latter which is destabilizing has a positive value. For MeCbl and GSCbl models the steric energy is a little less than half of the interaction energy showing significant electrostatic component of the bonding energy. For the case of H2OCbl the Pauli repulsion dominates the streric energy since its value +5.48kcal/mol. This shows that the water dipole has a little electrostatic interaction with Co^{3+} ion. The preparation energy which is also called the deformation energy is in the order GSCbl >MeCbl>H2OCbl for the models. This is reasonable since glutathionyl is a bulkier ligand. Also, the two different methods given in Table 2.16 for the calculation of this preparation energy are consistent with each other.

The bonding from the NBO analysis in the Co ligand structure of the RCbls is consistent with an 18 electron system with three lone pair d orbitals almost fully occupied. Thus the electron sum comes from six electrons in three lone pair Co d orbitals and twelve electrons in the Co-ligand bonds which are formed by charge donation from the ligands to Co unoccupied orbitals. The twelve electrons are in the σ bonds formed across two collinear N_{eq}-Co-N_{eq} and one collinear R_{ax}-Co-N_{ax} 3c/4e ω hypervalent prebonds. Here the dative bonding equatorial and axial nitrogen ligands show up as sp^2 or sp^3 NHOs with the bond polarized toward the nitrogen. On the other hand, the polarization coefficients for the NBO σ Co-S_{ax} and σ Co-C_{ax} bond show this bond is more covalent and the NHO involves a pure p_z orbital on the sulfur and carbon atoms of the ligands. The ECDA and EDA from the AOMIX analysis further confirm the CT

nature of the Co-S and Co-C bonds where .717e and .761e are transferred from ligand to the cobalt ion, respectively.

Table 2.16 Energies, kcal/mol for R-corr-Im in vac BLYP/6-311G (d,p). Two fragments: Co-corr-Im and R-.

	Me-Cbl	H2O-Cbl	GS-Cbl
E_{bind}	-246.61	-18.20	-166.01
E_{INT}	-266.53	-22.72	-202.24
E_{ORB}	-152.6	-28.2	-108.0
E_{steric}	-113.93	+5.48	-94.24
$E_{prep*(Eint-Ebind)}$	+19.92	+4.52	+36.23
$E_{prep**(EA^{sp}+EB^{sp}-EA^{opt}-EB^{opt})}$	+19.57	+4.56	+36.21

Table 2.17 Energies for Me-Cbl, GS-Cbl, and H2O-Cbls calculated with B3LYP/6-G311 (p,d) in vacuum and Im as a bottom ligand, in a.u.

	E_A^{opt}	E_B^{opt}	E_{AB}^{opt}
Me-Cbl	-2564.55778	-39.82883	-2604.78016
GS-Cbl	-2564.5579328	-1404.910603	-3969.7330958
H2O-Cbl	-2564.55778	-76.44745	-2641.0342007
	E_A^{sp}	E_B^{sp}	E_{AB}^{sp}
Me-Cbl	-2564.529885	-39.8255352	-2604.7801636
GS-Cbl	-2564.5383344	-1404.8724714	-3969.7330958
H2O-Cbl	-2564.5508115	-76.4471585	-2641.0342262

We compare the bonding in the three R-Co-corr-Im^+ models at the B3LYP/6-311G (d,p) in vacuum level in Fig. 2.9. The axial bond distances and Wiberg bond indexes, WBI, (in parenthesizes) are given on the figure. Models for GsCbl and MeCbl are seen to be similar in terms of the coring ring Wiberg bond indexes. Thus for the Wiberg Bond Index in NAO basis, GS-Cbl and Me-Cbl have almost the same values for Co-Neq in 6-member (0.34) and 5-member rings (0.39) while for H2O-Cbl these are significantly higher for 5-membered ring (0.42) and slightly higher for 6-membered rings (0.36).

The bond distances for β-axial ligand R-Co are 1.97 Å, 2.06 Å, and 2.30 Å for R= Me-, H2O-, GS- respectively; whereas the order of the bond indexes is not the same being Co-Cax (0.78)> Co-Sax (0.68)> Co-Oax (0.19). This can be expalained by two facts: (i) the Wiberg bond index indicates only covalent character and more impotantly that GS- is much bulkier ligand and must give some steric repulsion. This is also indicated by highest value of the preparation energy (+36.2 kcal/mol, Table 2.16). It is also seen that as the β-axial ligand bonding get stronger the α-axial ligand bonding gets weaker, i.e. a trans –ligand effect. Thus the α-axial ligand bond indexes are in the reverse order H2O-Cbl (0.47)> GS-Cbl (0.20) > Me-Cbl (0.13) and the ratio of WBI of the upper β-ligand-Co to WBI of the lower α-ligand-Co bond is 5.9 for Me-, 3.4 for GS-, and 0.45 for water. Furthermore, the total Wiberg BDIX, the Mulliken and natural charge have similar values for all equatorial nitrogens in the coring ring for all models as seen in Tables 2.9, 2.12, and 2.15. It is also observe that the axial nitrogen base has similar total Wiberg bond indexes no matter whether the base is imidazole or 5, 6-dimethylbenzimidazole. For the Co atom the total BDIX is similar in vacuum calculations for the three models of R-Co-corr-Im (around 2.7). On the other hand, for the GS-Co-corr-Bz the total BDIX is about 3.8 (Table 3.9). This might be due to water environment or to the change in the axial base.

In summary the charge and energy decomposition analysis as well as the bond indexes show that the models for GSCbl and MeCbl are very similar in their properties as opposed to the model of aquacobalamin. On the other hand, for all three R-cobalamin models, the coring ring has very similar properties.

Figure 2.9 R-Co-corr-Im^{+} models for GSCbl, H2OCbl, and MeCbl with axial bond distances in Å and Wiberg bond indexes in parentesis.

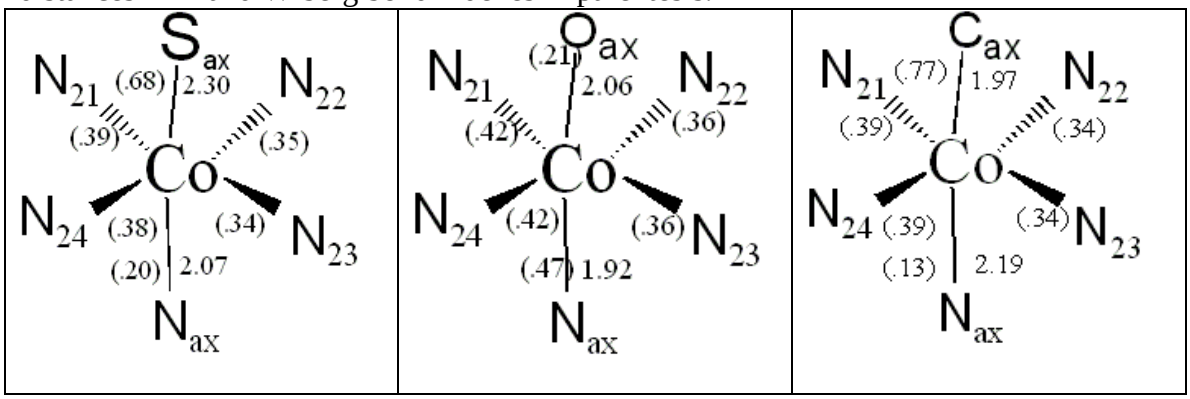

Chapter 3.

Simulation of the Electronic Absorption and CD Spectrum of GS-Cbl, H2O-Cbl, and Me-Cbl

3.1 Experimental and Computational Methodology

Aquocobalamin (hydroxy-cobalamin·HCl) and glutathione were obtained from Sigma-Aldrich Chemical Co. in < 97% purity. UV-VIS spectra were run with an Aligent model 8453 spectrometer and CD spectra with a Jasco J-810 spectrometer at ambient temperatures. Glutathionylcobalamin was made up in solution by adding a slight excess of glutathione to aquocobalamin (≈ 1:1 molar ratio). The GSCbl UV-VIS spectra for these solutions were identical to solutions made from solid authentic GSCbl kindly supplied by Nicola Brasch. Deiononized–distilled water was used to make up all solutions and all chemicals including those to make up buffers and salt solutions were analytical reagent grade.

Calculations with TD-DFT have been implemented in the Gaussian code based on the linear response theory (1) and our TD-DFT calculations conformed to nonequilibrium vertical transitions. With G03 and G09 the calculations were made with the 6-311g(d,p) basis set (2). For the GS-Cbl model we compared the B3LYP (3, 4) hybrid exchange correlation functional with the BP86 functional, the Becke-Perdew (5, 6) XC-potential, with generalized gradient approximation (GGA), utilizing G09 with the above basis set.

Excited state transitions were analyzed with Natural Transition Orbitals of Martin (7) as implemented in G09. NTO analysis gives hole and electron orbital representations

(isosurfaces) for the electronic transition density matrix for a given excited state transition.

At least three types of excited state calculations were done for each of the cobalamin species. These consisted of a simple calculation (i) of optimized ground state and excited state transitions of the molecule without considering any solvent effects (vac-vac). Another type (ii) was done in which the molecule was optimized without taking into account any solvent effects, but the excited state calculations for the optimized structure were done with a solvent model (vac-sol). Finally, calculations, type (iii), were done where the solvent was taken into account at every level, from the optimization to the energy transitions (sol-sol). It turned out that type (ii) calculations were closer to type (iii) than type (i) in excited transitions energies but the type (iii) matched the deconvoluted peaks better. The reason we used the type (ii) calculations with the GS-Cbl models was because with G03 code the geometry optimized calculations with a water CPCM model would not completely converge. However, with G09 this convergence was no longer a problem, and finally we only needed to compare the vacuum, type (i), calculations to the solvent optimized type (iii) calculations for simulating electronic spectra. Calculations of oscillator strengths were transformed into spectra using a home-made program which had the option of Lorentzian or Gaussian broadening.

3.2. Simulation of the Electronic Absorption and CD Spectrum of H2O-Cbl

We compared three types of excited state calculations for H2O-corrin-Im. As previously outlined, these were with the excited state calculations in vacuum, with the

excited state calculations in water solvent for H2O-corrin-Im, and calculations where the solvent was taken into account in both the optimization step and the excitation step (solvent optimized) for H2O-corrin-Im. We also used the B3LYP density functional methods with the same basis set, 6-311G (d,p), for all calculations. Figure 3.1 shows the results for three different calculation cases. The experimental absorption spectrum is included for comparison. The calculation results are for Gaussian broadened (1000 cm^{-1} HWHH) oscillator strengths versus wavelength and have been energy red shfted by 3679 cm^{-1} for excitation calculations in vacuum (vac-vac), by 3232.8 cm^{-1} for solvent calculations (vac-sol), and by 3511.9 cm^{-1} for solvent optimized calculations (sol-sol). Shifts were done by matching the 350 nm band. It is seen from the plot that all calculations have meaningful excitations in the whole experimental spectrum. The oscillator strengths used in Fig. 3.1 were arbitrarily multiplied be a factor of 3 to get spectra of the same magnitude as the experimental absorption spectrum.

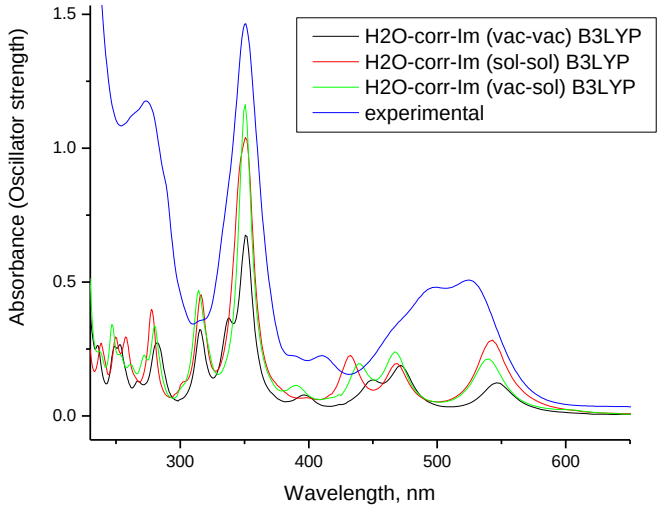

Figure 3.1. Gaussian broadened (1000 cm^{-1}) oscillator strength vs. wavelength in nm for H2O-Co-corr-Im compared with the experimental absorption spectrum of H2O-Cbl at pH 5.00. The calculation magnitudes have been arbitrarily multiplied by a factor of three.

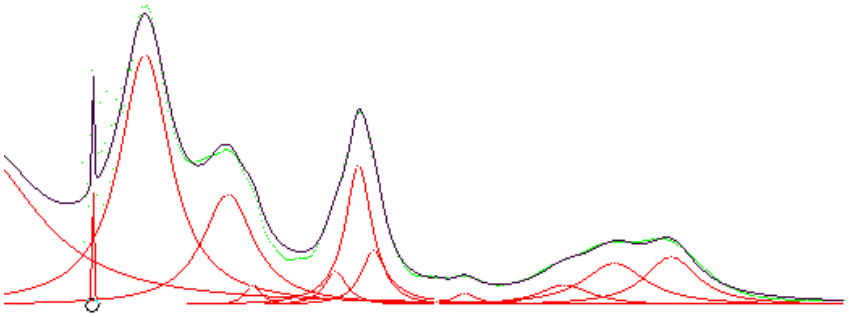

Fig. 3.2. Reconstracted experimental H2O-Cbl spectrum from deconvoluted peaks: green – experimental; red deconvoluted peaks of experimental spectra obtained with Fityk program, Lorentzian broadening applied; black – reconstructed model based on deconvoluted peaks

Table 3.1. Comparison of Spectral Peaks in nanometers for H2O-Co(III)-corrin-Bz Models Calculated in Water Solvent at B3LYP/6-311G(d,p) with the Experimental Absorption Spectrum of Aquocobalamin, pH 5.

Experimen-tally Observed Peaks (nm)	Deconvoluted Peaks (nm) from Experim (blue)	H2O- Cbl (nm) Vac-vac (black)	H2O-Cbl (nm) sol-sol (red)	H2O- Cbl (nm) vac-sol (green)
525 s, α band	530.4 m	546	541	539
497 s, β band	497.6 m			
	468.7 w	471	468	467
		449 sh	432 sh	439 sh
411, D band	411.1 w	425 sh	416 sh	423 sh
390, E band	394.9 vw	397 w		390 w
352, γ band	358.4 sh	351 s	351	351 s
	349.4 vs			
	336 sh	337 sh		
316	312 w	316 ms	316 ms	314 ms
288 sh	288.5 ms	282 m	302	280 m
273 s				272 sh
264 sh	267.0 vs	267 w	278	262
		253	258	253
		249	250	247
		236	238	237
		227	222	227
			217	218

Deconvoluted spectrum is shown in Fig. 3.2. Deconvoluted Bands -vs: very strong, s: strong, ms: medium strong, m: medium, w: weak.

Table 3.1 shows the ten discernible peaks in the experimental absorption spectrum, and the Gaussian deconvoluted peaks in this spectrum. Figure 3.2 shows reconstructed experimental spectra from the deconvoluted spectrum and the peaks in two of the simulated spectra from Gaussian broadened oscillator strength. The experimental spectrum in the α,β region can be deconvoluted into three components at 530 nm, 497 nm, and 469 nm. When the three structural models calculated with B3LYP are shifted by the correct amounts to line up with the 350 nm band, they all show two bands in this region which are around 540 and 470 nm. In all model calculations there is no band at 497 nm. The shift between 534 nm and 497 nm in wavenumbers is 1243 cm^{-1} which is of the order of vibrational frequency in the long-axis C=C stretching vibration. Previously for aquocobalamin this band was considered to be a vibronic (8) which agrees with the above results.

The shifted simulations also show that on comparing the optimized (vac-sol) with the solvent optimized (sol-sol) results for H2O-corr-Im, all three calculations simulate the experiment band at 460 nm. In the 330 nm to 380 nm region all simulated spectra are very similar with only difference being that the vac-vac calculation shows an extra peak at 337 nm. The experimental spectrum shows two less resolved bands, shoulders of the 350 nm peak at 358 and 336, and peaks at 390 nm and 411 nm in the valley between γ and α, β regions. The shoulder at 390 nm only shows in the vac-vac and vac-sol simulations. In fact, there is no preferable simulation for the H2O-corr-Im model and the goodness of the fit depends on the spectral region.

In Figure 3.3 we compared electronic circular dichroism spectra of the experimental and simulated models for H2O-corr-Im which are calculations where the solvent was taken into account only in excitation step (vac-sol) and calculations where the solvent was taken into account in both the optimization step and the excitation step (sol-sol). The length rotatory strength were compared from the B3LYP /6-311G (d,p) calculations with experiment as opposed to velocity rotatory strength. The calculations used a broadening of 1000 cm^{-1} and all were shifted by 1600 cm^{-1}, and the factor of 3 was used for scaling the calculated rotatory strengths. It appears that calculations where the solvent was taken into account only in the excitation calculation (vac-sol) gives a better simulated spectrum with respect to wavelength than the sol-sol one.

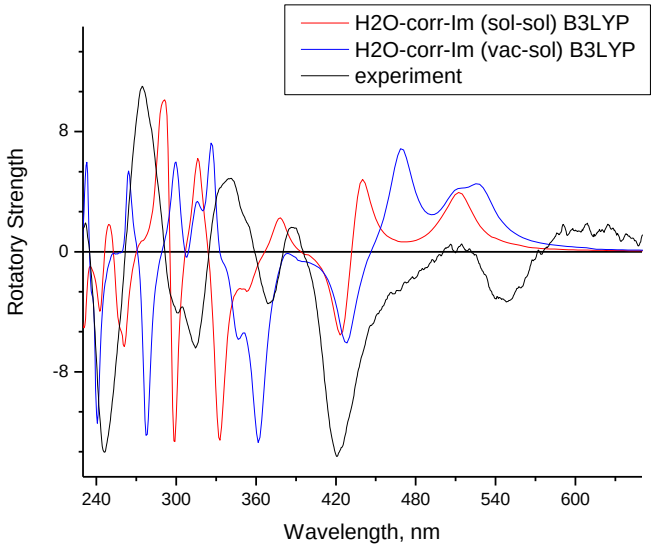

Figure 3.3. Circular dichroism, differential extinction (M^{-1} cm^{-1}), vs wavelength (nm) for the experimental of H2O-Co-corr-Im and rotatory strengths for calculations. Results calculated in length gauge for H2O-corr-Im with solvent optimized (red) and H2O-corr-Im with vac-sol optimized (blue) gauge which are Gaussian broadened (1000 cm^{-1}, HWHH of peak).

Simulating the experimental CD spectrum is complicated by the fact that each experimental band can be a summation of rotatory strengths at more than one transition and simulating the bands depends on how the rotatory strengths are allocated to each band and their bandwidths. The CD spectrum depends on the conformation of the molecule in the solution and our truncated models are not detailed enough, no side chains, to do a good job in simulating the experimental spectra.

3.3. Simulation of the Electronic Absorption and CD Spectrum of Me-Cbl

We compared three types of excited state calculations for each of the two different chemical models of methyl-cobalamin: Me-corrin-Im and Me -corrin-Bz. As previously outlined, these calculations were with the optimized ground and the single point excited state in the vacuum-vacuum, vacuum-solvent cases for Me-Co-corr-Im and solvent-solvent simulations for both Me-Co-corr-Im and Me-Co-corr-Bz. Figure 3.4 shows the results for the four different cases at B3LYP/6-311G (d,p) level and Figure 3.5 shows reconstructed spectrum from the deconvolution. The experimental absorption spectrum is included for comparison. The calculation results are for Gaussian broadened (1000 cm^{-1} HWHH) oscillator strengths versus wavelength and have been energy shifted in the Me-Co-corr-Im model by 100 cm^{-1} for the vac-vac, 48 cm^{-1} for vac-sol, and 1711 cm^{-1} for sol-sol in order to line up with the experimental deconvoluted peaks. Suprisingly the excited state energy simulation did not have to be shifted at all for the Me-Co-corr-Bz model. The electronic position operator oscillator strengths used in Fig. 3.4 were

arbitrarily multiplied be a factor of three to get spectra of the same magnitude as the experimental absorption spectrum.

Table 3.4 shows fifteen Gaussian deconvoluted peaks in the experimental absorption spectrum, and the observed peaks in four of the simulated spectra from Gaussian broadened oscillator strength. The α,β region can be deconvoluted into three components at 552 nm, 524 nm, and 490 nm. When the four structural models calculated with B3LYP are shifted by the correct amounts to line up with the 553 nm band, they all show only two bands in this region. These peaks are found at 553 nm and 475 nm and peaks in the region do not have a band close to 521 nm. In aquocobalamin this band was considered to be a vibronic band and because the purely electronic excitation calculations do not show this band, we again consider this band in Met-Cbl to be of vibronic origin.

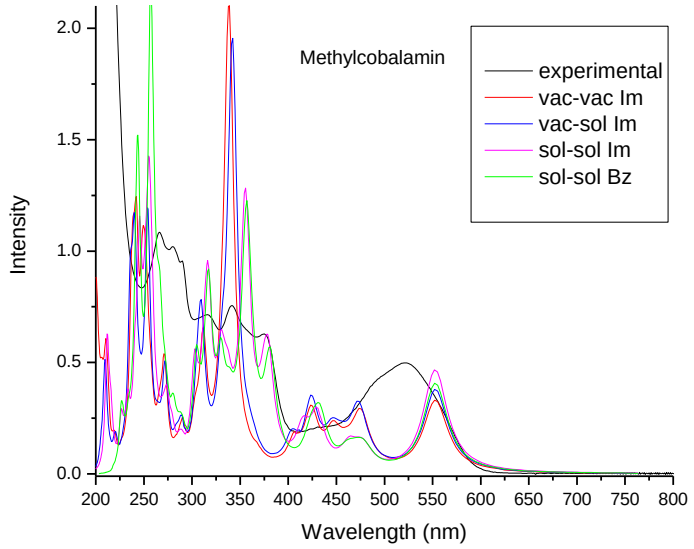

Figure 3.4. Gaussian broadened (1000 cm^{-1}) oscillator strength vs. wavelength in nm compared with the experimental absorption spectrum for Me-Co-corr-Im at pH 5.00. The calculation magnitudes have been arbitrarily multiplied by a factor of three. Each spectrum shifted: by vac-vac Im 100 cm^{-1}, vac-sol Im 48 cm^{-1}, sol-sol Im 1711 cm^{-1}, sol-sol Bz no shift.

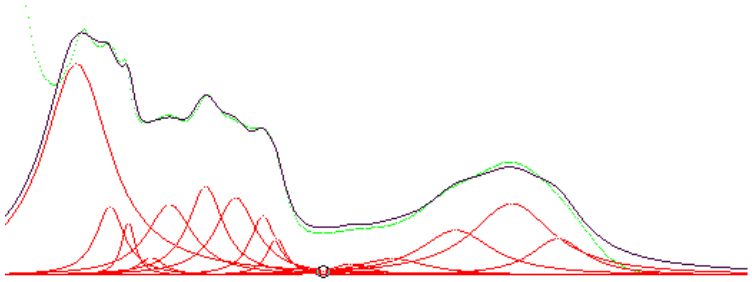

Fig. 3.5. Reconstracted experimental Me-Cbl spectrum from deconvoluted peaks: green – experimental; red deconvoluted peaks of experimental spectra obtained with Fityk program, Lorentzian broadening applied; black – reconstructed model based on deconvoluted peaks

On comparing the experimental band at 490 nm with the shifted simulations shows that all of the simulations are at a considerably lower wavelength around 475 nm. None of the simulated spectra (Table 3.4) show a peak at 521 nm wavelength which suggests this is a vibronic band as in the case of aquocobalamin. The difference between 552 nm and 524 nm deconvoluted experimental peaks is 968 cm^{-1} and the difference between 524 nm and 490 nm is 1324 cm^{-1}. Previously both 524 nm and 490 nm bands were considered to be vibronic but the difference in the vibrational energies and the simulated results which show the 475 nm suggests that the band at 524 nm is not vibronic. Further investigation of this conclusion is nessesary for more certainty. The two simulations that best fit the experimental absorption spectrum are the Me-Co-corr-Im and Me-Co-corr-Bz chemical models made with the cpcm water solvent model for both the ground state optimization and excited state single point calculation (sol-sol). Thus the green and purple spectra are been seen virtually at the top of each other.

Table 3.4. Comparison of Spectral Peaks in nanometers for Me-Co(III)-corr-Im(Bz) Models Calculated in Water Solvent at B3LYP/6-311G(d,p) level with the Experimental Absorption Spectrum of methylcobalamin, pH 5.

Experimen-tally Observed Peaks (nm)	Deconvoluted Peaks (nm) from Experimental (black)	Me-Cbl Peaks (nm) Vac-vac Im (red)	Me-Cbl Peaks (nm) sol-sol Im (purple)	Me-Cbl Peaks (nm) vac-sol Im (blue)	Me-Cbl Peaks (nm) Sol-sol Bz (green)
551	552	553	553	553	553
521 s	524				
490	490.1	475	475	472	475
	451.9	446	464	446	464
431	426.8	423	429	424	431
	410.6	406	416	404	
	381.9		377		380
375	373.7				
	357.3		355		357
342 s	339	338	337	342 s	339
			330		330
316	317.4	311	316	309	317
	306	290	302	288	305
290	292.2		288	283	293
280	281.3		279		288
265	260.9	271	273	271	280
		250	255	254	265
		242	245		256
			241	240	243
			233	236	234
			226		226
		220	216	220	
		211	212	209	

Deconvoluted spectrum is shown in Fig. 3.5. Deconvoluted Bands -vs: very strong, s: strong, ms: medium strong, m: medium, w: weak.

In Figure 3.5 we compared the experimental and simulated B3LYP circular dichroism spectra.

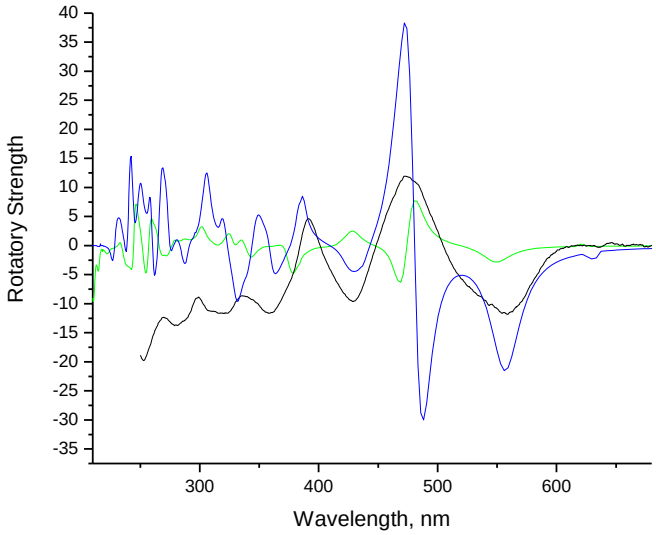

Figure 3.5 Circular dichroism, differential extinction (M^{-1} cm^{-1}), vs wavelength (nm) from rotatory strengths. Results calculated in both length (blue) and velocity (green) gauges which are Gaussian broadened (1200 cm^{-1}, HWHH of peak). Shift 1600 cm^{-1}.

Both the velocity and length rotatory strengths calculation were compared with experiment for Me-Co-corr-Bz solvent-solvent model at the B3LYP/6-311G(d,p) level with cpcm. There is a well-know problem with all-electron calculations which use Gaussian basis sets in that they do not obey gauge-invariance with finite basis set representations. Usually the velocity gauge does better than the length gauge; however, our results indicate that the length scale is a better fit to the experimental. The simulation of the electronic CD spectrum for the above Me-Co-corr-Bz case results in a better fit to the experimental data than was found for the H2O-Co-corr-Im model fit to the CD spectrum of aquocobalamin.

3.4. Simulation of the Electronic Absorption and CD Spectrum of GS-Cbl

We compared two types of excited state calculations for each of the three different chemical models of glutathionyl-cobalamin: GS-Co-corr-Im, zwitterionic GS-Co-corr-Bz and GS-Co-corr-Bz. As previously outlined, these were with the ground and excited state calculations in vacuum for GS-corrin-Im and calculations where the solvent was taken into account in both the optimization step and the excitation step (solvent optimized) for GS-Co-corr-Im and the two forms of GS-Co-corr-Bz. In addition to the different chemical structural models, we also used both the B3LYP and BP86 density functional methods with the same basis set, 6-311G(d,p), for all calculations. Figure 3.7 shows the results for five different cases. Four cases are at B3LYP/6-311G(d,p) level for GS-Co-corr-Im in vacuum and water, zwitterionic GS-Co-corr-Bz and the protonated form in water. The fifth case is for GS-Co-corr-Bz in water at the BP86/6-311G(d,p) level. The experimental absorption spectrum is included for comparison.

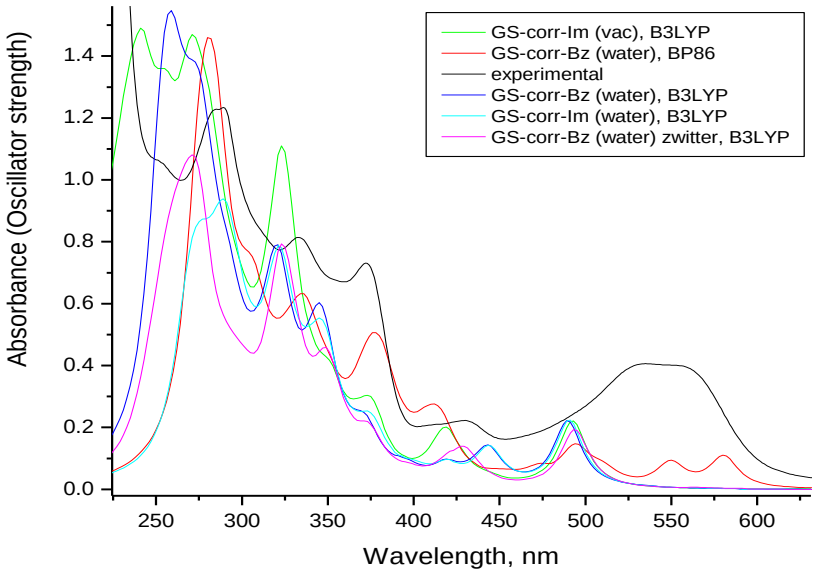

Figure 3.7 Gaussian broadened (1700 cm^{-1}) oscillator strength vs. wavelength in nm compared with the experimental absorption spectrum at pH 5.00. The calculation magnitudes have been arbitrarily multiplied by a factor of six.

The calculation results are for Gaussian broadened (1700 cm^{-1} HWHH) oscillator strengths versus wavelength and have not been energy shifted although density functional results usually overestimate energy transitions. It is seen from the plot that with B3LYP only excitations below 500 nm appear, while the BP86 calculation has oscillator strength under the first few low energy transitions in the experimental spectrum. This is quite noteworthy since most previous calculations of various cobalamins, especially with the B3LYP functional, needed to be red shifted by ca. 4000 cm^{-1} to get plots which matched experiment. In our calculations the B3LYP results would need to be red shifted by amounts of between 2475 cm^{-1} and 2605 cm^{-1} for the low energy transition to line-up with the α deconvoluted peak in the experimental spectrum at 561 nm.

Table 3.5. Comparison of Spectral Peaks in nanometers for GS-Co(III)-corrin-Bz Models Calculated in Water Solvent with the Experimental Absorption Spectrum of Glutathionylcobalamin, pH 5.

Experimentally Observed Peaks (nm)	Deconvoluted Peaks (nm) from Experiment (a)	Protonated GS- Peaks (nm) BP86/ 6-311G(d,p) (b)	Protonated GS- Peaks (n) B3LYP/ 6-311G(d,p (c)	Zwitterionic GS- Peaks (nm) B3LYP/ 6-311G(d,p) (d)
615 sh	612 w			
	583 ms	580		
561	561 ms	555	560	561
534	529 ms			
498	496 m	493	500	501
	475 w	473	472	472
	457 w	449		
433	432 m		441	446
410	408 m	412	411	415
	388 w			
372	375 s	378	380	381
355	357 ms	347		
333	334 vs	337	348	351
310 sh	304 vs	306	315	312
	291 vs			
287 283	280 s 279 s	284 276	296	295 290
	269 s	-	274	
254	252 vs	-		

(a) Deconvoluted spectrum is shown in Fig. 3.8. Deconvoluted Bands -vs: very strong, s: strong, ms: medium strong, m: medium, w: weak. (b) Peaks taken from Fig. 3.7, no shift in calculated peaks; (c) Peaks taken from Fig. 3.8, red shifted 2605 cm^{-1}.
(d) Peaks taken from Fig. 3.7, red shifted 2545 cm^{-1}.

The 12 discernible peaks in the experimental absorption spectrum in Fig. 3.7 are listed in Table 3.5, along with the Gaussian deconvoluted peaks in this spectrum. All the deconvoluted peaks are shown in Fig. 3.8 below.

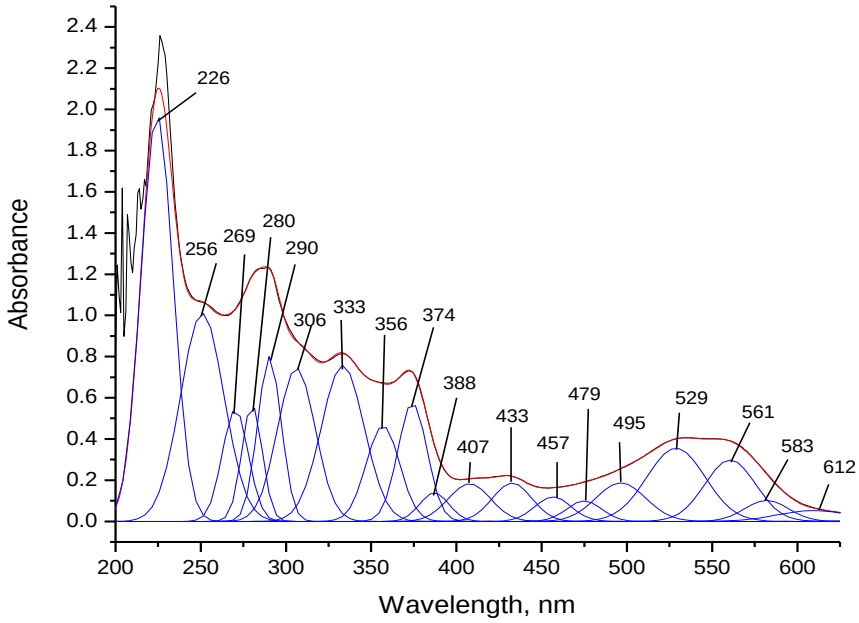

Figure 3.8 Deconvolution of the absorption spectrum of glutathionycobalamin.

Table 3.5 also shows peaks in three of the simulated spectra from Gaussian broadened oscillator strength. The α,β region can be deconvoluted into five components at 612 nm, 583 nm, 561 nm, 529, and 496 nm. When the four structural models calculated with B3LYP are shifted by the correct amounts (Fig. 3.9) to line up with the 561 nm band, they all show only two bands in this region very close to 561 nm and 500 nm. None of the simulated spectra have a band close to the experimentally observed deconvoluted peak at 529 nm. In aquocobalamin this band was considered to be a vibronic band and because the purely electronic excitation calculations do not show this band, we also consider this band in GS-Cbl to be of vibronic origin. The shifted simulations also show that on comparing the water with the vacuum results for GS-Co-cor-Im, the vacuum calculation does not simulate the experiment band at 496 nm. All the other simulations done in water do show a transition around 500 nm. Another indication

of the improvement of the solvent optimized calculations over the vacuum one is the simulation in the 330 nm to 380 nm region. The experimental spectrum shows two strong peaks at 372 nm and 333 nm with a less resolved band at 355 nm in the valley between them. All of the water calculations suppress oscillator strength in this valley which is most pronounced at 350 nm in the shifted vacuum calculation. In fact, the BP86 calculation does the best at simulating this region.

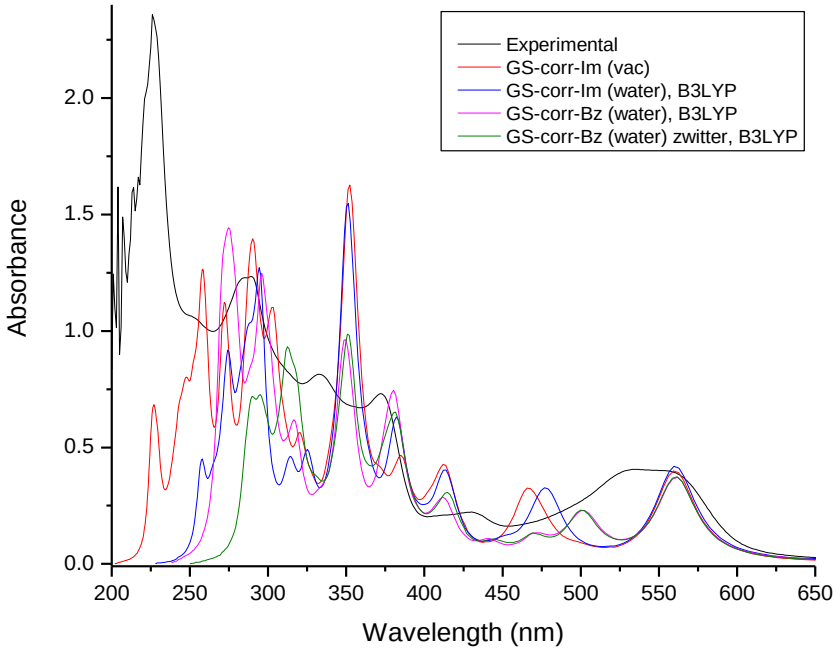

Figure 3.9 Gaussian broadened (1700 cm^{-1}) oscillator strength vs. wavelength in nm compared with the experimental absorption spectrum at pH 5.00. The calculation magnitudes have been arbitrarily multiplied by a factor of six.

Other comparison of interest from the results in Fig. 3.7 are between the B3LYP water optimized GS-Co-corr-Im and the B3LYP water optimized GS-Co-corr-Bz which are nearly on top of each other. Thus changing the axial base from imidazole to 5, 6-dimethylbenzimidazole has little effect on the calculated excitation spectra. Also the water optimized zwitter ionic and protonaned GS-Co-corr-Bz B3LYP shifted simulations

are almost exactly equal to each other as seen in Table 3.5, but the spectrum of the shifted zwitter ion form lacks any features in the 270-280 nm region which is observed in the experimental spectrum. Both the B3LYP and BP86 water optimized simulations for protonated carboxylic groups do show bands in this region. In comparing the latter two simulations when the B3LYP excitations are red shifted, most of the calculated peaks are very close in wavelength (Table 3.5) except that the BP86 calculations shows the experimental peak at 580 nm which is not calculated with B3LYP. Also BP86 does much better in simulating the very strong peak in the experimental spectrum at 333 nm where the shifted B3LYP simulation is nearly 20 nm too low at 315 nm (Table 3.5).

The electronic position operator oscillator strengths used in Fig. 3.7 were arbitrarily multiplied by a factor of six to get spectra of the same magnitude as the experimental absorption spectrum. In order to make comparisons on an absolute basis with experiment, we converted these oscillator strengths to molar extinction coefficients using the formula (9) $f_i = 4.61 \times 10^{-9} \varepsilon_{max} \bar{\nu}_{1/2}$ where $\bar{\nu}_{1/2}$ is the fixed full width at half maximum (FWHM) for each band. A value of $\nu_{1/2} = 1000$ cm^{-1} was used to convert all oscillator strengths f_i to ε_{max} which were then Lorentzian broadened by 1000 cm^{-1} (FWHM) to simulate the spectrum.

The results in Fig. 3.10 show good absolute agreement of the water optimized BP86/6-311G (d,p) simulated spectrum with the experimental spectrum. Both B3LYP/ 6-311G (d,p) and BP86/6-311G(d,p) excitation calculations give extinction coefficients which are within a factor of about two or better of the experimental extinction coefficients (Appendix I). The oscillator strengths are increasingly overestimated as the transitions move toward higher energies (425 nm to 250 nm region). The B3LYP calculation needed

to be uniformly red shifted by 2605 cm^{-1} to match up (Appendix II) but this is far less than shifts made in previous comparisons of vacuum excitations B3LYP calculations with cobalamin experimental spectra in water. For example shifts of 5500 cm^{-1} were used for these comparisons in aquo-, methyl-, and adenosyl- cobalamins (10). It is rather remarkable that the BP86/6-311G (d,p) water calculation is so good at predicting the transition energies. Furthermore it is clear that the BP86 gives a better simulated spectrum than B3LYP with respect to extinction coefficients and wavelength (Appendix II).

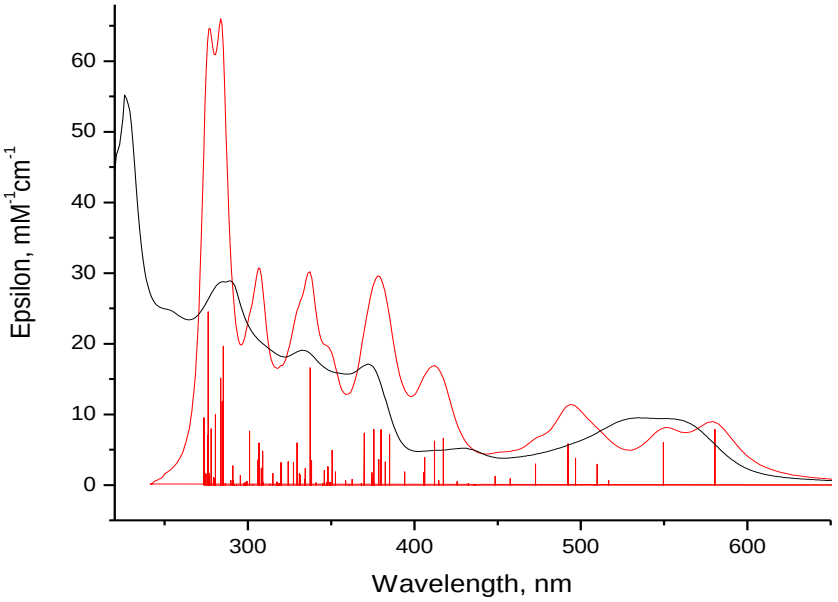

Figure 3.10. Absolute electronic absorption (extinction)) vs wavelength (nm) spectra from a BP86/6-311G(d,p) GS-Co-corr-Bz aqueous model compared with the experimental spectra (black) at pH 5.00. Calculated oscillator strength, red sticks, and their Lorentzian broadened (1000 cm^{-1}, FWHM) extinction coefficients spectrum in mM^{-1} cm^{-1}, red line vs. wavelength. The conversion of oscillator strength to extinction coefficient maximum is discussed in the text.

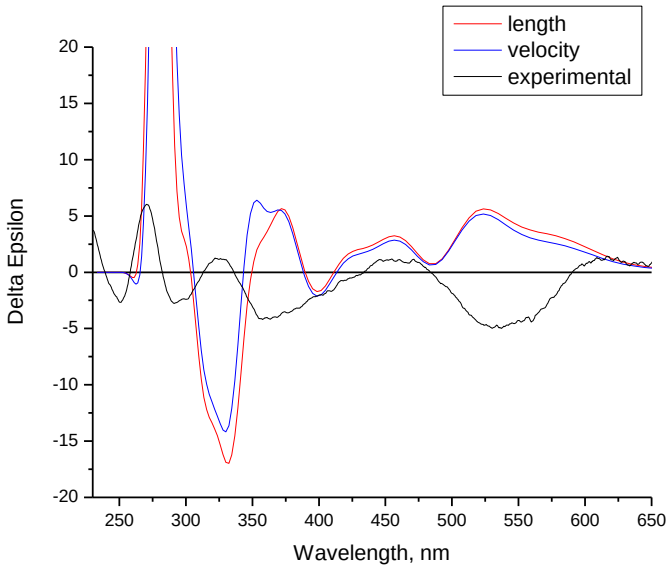

Figure 3.11. Absolute electronic circular dichroism, differential extinction (M^{-1} cm^{-1}), vs wavelength (nm) from rotatory strengths. Resulits calculated in both length (red) and velocity (blue) gauges which are Gaussian broadened (1200 cm^{-1}, HW at 1/e of peak). The conversion of rotatory strength to differential extinction is discussed in the text.

In Figure 3.11 we compare the experimental and simulated (BP86) circular dichroism spectra. The absolute electronic circular dichroism, EDC, calculated spectrum was compared with the room temperature experimental differential extinction spectrum as shown in Fig. 3.11 by converting calculated rotatory strength to differential extinction. The differential extinction in M^{-1} cm^{-1} is given by (11) $\Delta\varepsilon_i = \lambda^o R \times 10^{40} \Big/ 22.94\lambda_{1/2}\sqrt{\pi}$ where R is the calculated rotatory strength for randomly oriented samples in the cgs units of 10^{-40} erg-esu-cm/Gauss, λ^o is the transition energy (band center in cm^{-1}) and $\lambda_{1/2}$ in cm^{-1} is the half-width at 1/e of the peak height . The value of $\lambda_{1/2}$ used to convert to Δε was 1200 cm^{-1} and the spectrum was broadened with a Gaussian half-width (1/e Max) of 1200 cm^{-1} or a FWHM of 1998 cm^{-1}. Both the velocity and length rotatory strengths were compared from

the BP86/6-311G(d,p) calculation with experiment. There is well-know problem with all-electron calculations which use Gaussian basis sets in that they do not obey gauge-invariance with finite basis set representations (12). Usually the velocity gauge is used which does alleviate some of this problem. Our results do vary slightly with gauge at each transition energy, but for the most part the two simulated CD spectra are very similar and track each other with a noticeable deviation around 350 nm, Fig 3.11.

Comparing the absolute experimental and simulated ECD spectra, the magnitude of the differential extinction $\Delta\varepsilon$ of the simulated spectrum agrees quite well with the experimental spectrum especially in the 350 nm to 600 nm region, but again at lower wavelength, the magnitude of the simulated results are substantially larger. In addition, what is immediately obvious in Fig. 11 is that $\Delta\varepsilon$ calculated for several bands is opposite in sign to the experimental bands. Simulating the experimental ECD spectrum is complicated by the fact that each experimental band can be a summation of rotatory strengths at more than one transition and simulating the bands depends on how the rotatory strengths are allocated to each band and their bandwidths. Table 3.6 shows a comparison of the deconvoluted ECD and UV-VIS experimental spectral bands and it is clear that the transition energies are consistent between the two except that the UV-VIS displays more transitions. It is also seen that the ECD bandwidths (FWHM) vary from around 1000 to 2600 $cm^{-1,}$ Table 3.6. Nonetheless, even with variable bandwidths, it does not seem that the simulated spectrum could be made into a good fit to the experimental one. An explanation of the poor match between experimental and simulated ECD spectra is that the truncated geometric model is not sufficient because it lacks side-chains which should affect the configuration of the glutathionyl group. It has also been found in the X-

ray crystal structure study that the GS- ligand could be modeled in two distinct configurations (13). Thus the simulated structure is a good representation of the experimental structure involved in the electronic transitions but it does not well represent the solution configurations to which the ECD spectrum is sensitive.

Table 3.6. Deconvoluted peaks and band widths from the experimental glutathionylcobalamin ECD spectrum compared with UV-VIS Spectrum.

Deconvoluted UV-VIS peaks in nm	Deconvoluted peak centers in ECD spectrum in nm	ECD Peak Heights $\Delta\varepsilon$ in $M^{-1}cm^{-1}$	Full Width at Half Maximum in cm^{-1}
615	608	3.8739	2177.6
561	558	-6.37544	1865. 9
529	524	-6.19468	1753.3
496, 475	472	2.83331	2008.1
457, 432	448	1.63826	1113.6
408	405	-1.55219	1218.2
388	381	-3.44911	2206.2
357	357	-6.49011	2667.2
334	327	4.2112	2828.3
304	302	-3.48864	1535.6
291, 280, 279	289	-5.58614	1913.3
269	270	12.1707	2468.7
252	252	-6.26344	2565.2

3.5 Excited State Transitions from TD-DFT Calculations for GS-Cbl.

In an excited state singlet TD-DFT treatment with the BP86 density functional for the aqueous GS-Co-corr-Bz model, we calculated one hundred excited states. Most transitions were calculated in the visible and the lowest wavelength (highest energy) transition was at 273 nm in the UV region. In contrast, with the B3LYP TD-DFT treatment with the same chemical model, only fifty excited states were needed to get to the highest energy transition at 252 nm. One of the reasons for the good fit of the former calculation is the multitude of transitions calculated in the UV region as seen from Figure 3.10.

In both BP86 and B3LYP calculations, the HOMO to LUMO transition is calculated with very low oscillator strength. The calculations with BP86 show a first excited singlet state, S_1, at 756.90 nm with oscillator strength f= 0.0010 and this is the HOMO $\rightarrow$ LUMO with 0.69 (95%) expansion coefficient. State 2 is at 663.36 nm with an even smaller oscillator strength, f=0.0002, and is the HOMO$\rightarrow$ LUMO+1 with 0.70 (98%) expansion coefficient. Calculated excited states S_1 and S_2 are excited state transitions that are dominated by a simple transition between one occupied MO and an unoccupied MO. In most of the other excited state transitions, several Slater Determinants of occupied to vacant orbital promotions make up the excitation. These low intensity transitions do not appear strong enough to come out in the experimental spectrum above 600 nm. However, there is a broad deconvoluted peak (Table 3.5 and Fig. 3.8) centered at 612 nm and this transition is also seen in the CD spectrum at 609 nm, but the closest calculated excitation is S_2 at 664 nm. The theoretical results indicate that the two lowest energy transition are

above 600 nm and are very weak which is consistent with their ill defined nature in the experimental absorption spectrum in this region.

For the BP86 calculation we use the compact Natural Transition Orbitals (NTOs) of Martin's treatment (7) to discuss the nature of the transitions in the UV-VIS absorption spectrum. Table 3.7 gives the excitation properties of the 34 states with significant oscillator strength ($f \geq .01$) in terms of the description of the hole and electron NTOs. Images of the 34 holes and electron isosurfaces are illustrated in Appendix III. We also report in the Appendix IV the set of expansion coefficients for each of these 34 excited states. In the first column of Table 3.7, we indicate fifteen deconvoluted experimental bands to which the calculated excitations can be assigned. We include S_1 as an exception (f= 0.001) in the tables since it is the HOMO $\rightarrow$ LUMO transition. In this transition the electron density change is mainly from the Spy $\rightarrow$ corr π^* but the NTOs also show that a small amount electron density goes from an extended σ bond (N24-Co(dyz)-N22) to the corr π^* leaving Co(dyz) in the electron NTO. Other stronger transitions which include the HOMO in the hole where the sulfur p_y orbital is a major contributor of electron density are S_8, S_{27}, and S_{40}, where of the expansion coefficients (Table 3.7) which contain the HOMO in the donor are 55%, 74 %, and 96%, respectively. Moreover, Table 3.7 shows that almost every transitions contains cobalt d orbitals in the hole and electron NTOs. This can be seen in the snap shots of the NTO hole – electron isosurfaces of the excitations, Appendix III.

The first calculated state with strong oscillator strength, f = 0.0337, is S_3 at 580.50 nm and is the only excitation that appears under the deconvoluted peak at 583 nm of the experimental spectrum (Fig. 3.10 and Table 3.7). This transition contains two parts (i) a localized axial σ Co(dxz)-S(pz) bond $\rightarrow$ Co(dxz) atomic orbital and (ii) a corr $\pi\rightarrow$ corr π^*.

This transition is the HOMO-1 → LUMO transition (Table 3.7) with an expansion coefficient is 93%. In part (i) it appears that electron density comes out of the hole σ bond leaving a bare Co(dxz) orbital in the excited state in addition to corrin π* orbitals (Fig. 3.12). The next excited state transition S_4 at 560.6 nm also has considerable oscillator strength (f=.0257) as noted in Table 3.7 and again is the only transition under the deconvoluted peak at 561 nm. Table in Appendix IV shows this transition is HOMO-1 → LUMO+1 transition with an expansion coefficient of 86 %. These transitions, S_3 and S_4 contain π → π* corrin ring and also a σ (Co-S) → Co(d) type transition. The electron and hole NTOs for the two transitions are shown in Figure 3.12. Other transitions which involve Co-S σ bond in the hole are S_{18}, S_{20}, S_{25}, S_{37}, and S_{89}.

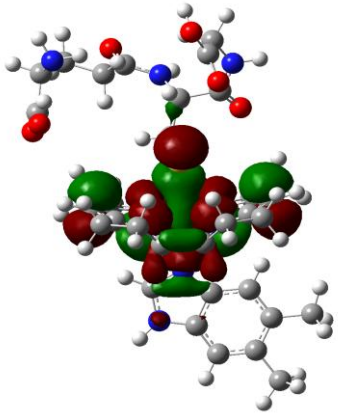

Hole NTO, S_3

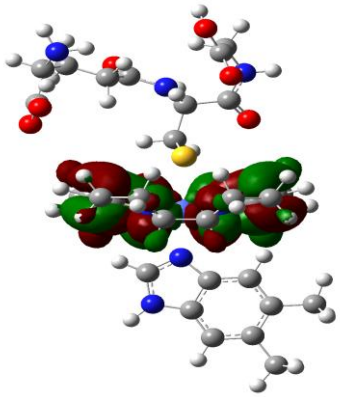

Electron NTO, S_3

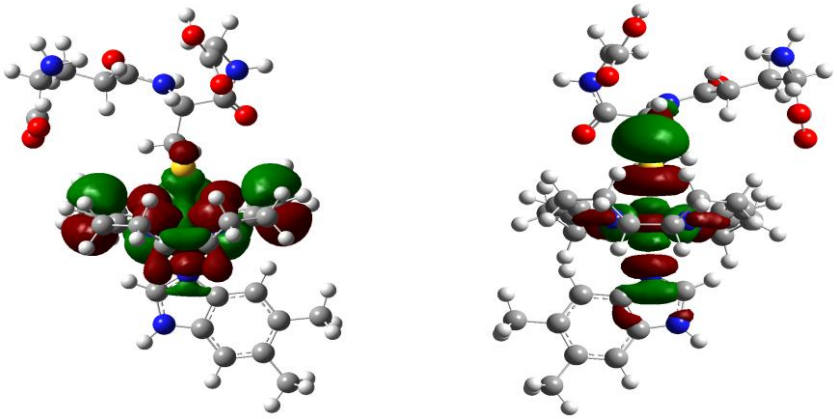

Hole NTO, S_4 Electron NTO, S_4

Figure 3.12. Electron and hole isosurfaces of Natural Transition Orbitals for states S_3 and S_4 from a BP86/6-311(d,p) calculation.

There are also a number of transitions which clearly show the Co-S π bonding interaction in the hole. For example, excited state 24 (f=0.0307) which can be assigned to the deconvoluted band at 388 nm can again be decomposed into two components: π(Co(dyz)+S(py))→ Co(dx2-y2) and corr π → corr π* which is shown in the hole and electron NTOs for S_{24}, Figure 3.13. The hole NTO for S_{24} contains HOMO-2 (Fig. 3.13) which shows π Co-S bonding and comes from an expansion coefficient which contributes 44 % of the transition. Other exited states where the hole NTO shows a π Co-S bonding interaction are S_9(f=0.025), S_{26} (f=0.0335), S_{66} (f=0.256), S_{85}(f= 0.0842) which are dominated by HOMO-2 in the donor with 52 %, 44%, 42%, and 62%, expansion coefficient contributions, respectively. The strongest oscillator strength of any transition is for S_{85} and the hole and electron NTOs are also shown in Figure 3.13 where the overall transition is π(Co(dyz)+S(py))+ corr π → glutamacyl part of the glutathionyl axial ligand.

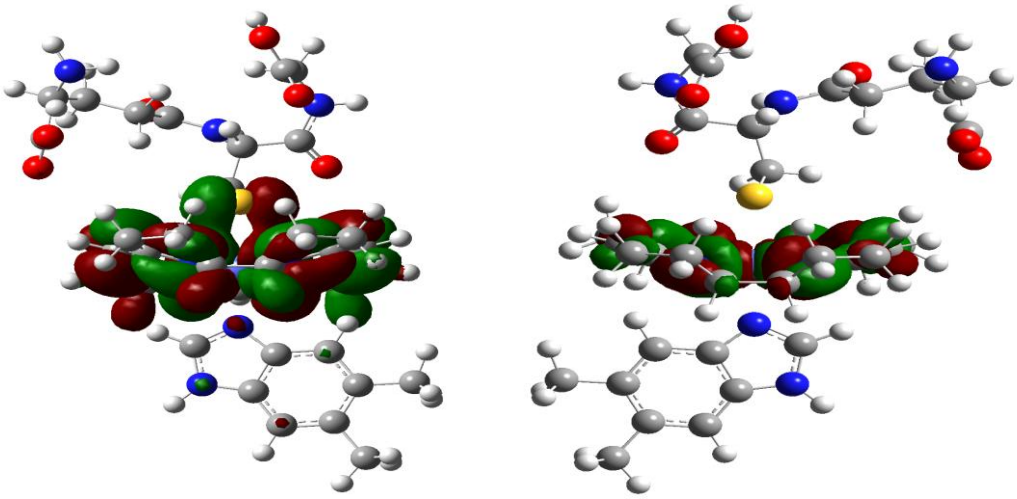

Hole NTO, S_{24} Electron NTO, S_{24}

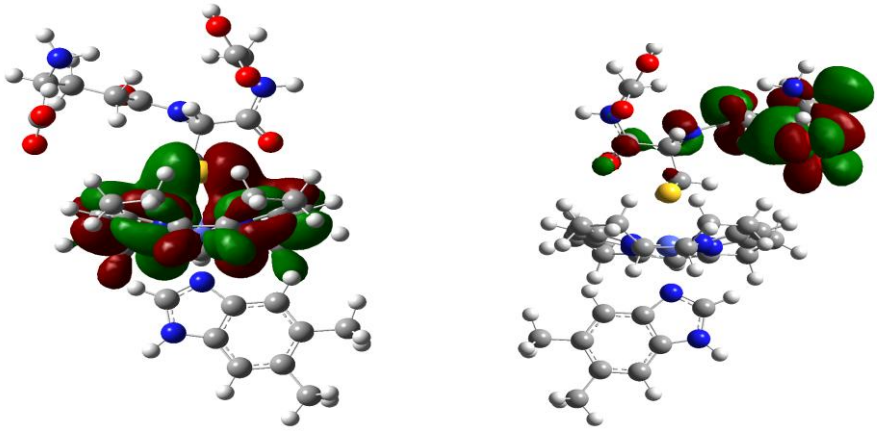

Hole NTO, S_{85} Electron NTO, S_{85}

Figure 3.13. Electron and hole isosurfaces of Natural Transition Orbitals for states S_{24} and S_{85} from a BP86/6-311(d,p) calculation.

There are quite a few excited states in which the hole NTOs show a complicated isosurface involving more than simple Co-S bonding and/or corrin π bonds. For example, excited state 46 (f=0.071) assigned to the band at 357 nm and excited state 90 (f=0.0426) assigned to the band at 280 nm are both excitations with considerable oscillator strength and have multi-centered donors. Figure 3.14 clearly shows the hole NTO for S_{46} has a four centered Neq-

Co-S-Neq bonding interactions from which density is withdrawn and donated to Co(dyz) and corrin π* in electron NTO.

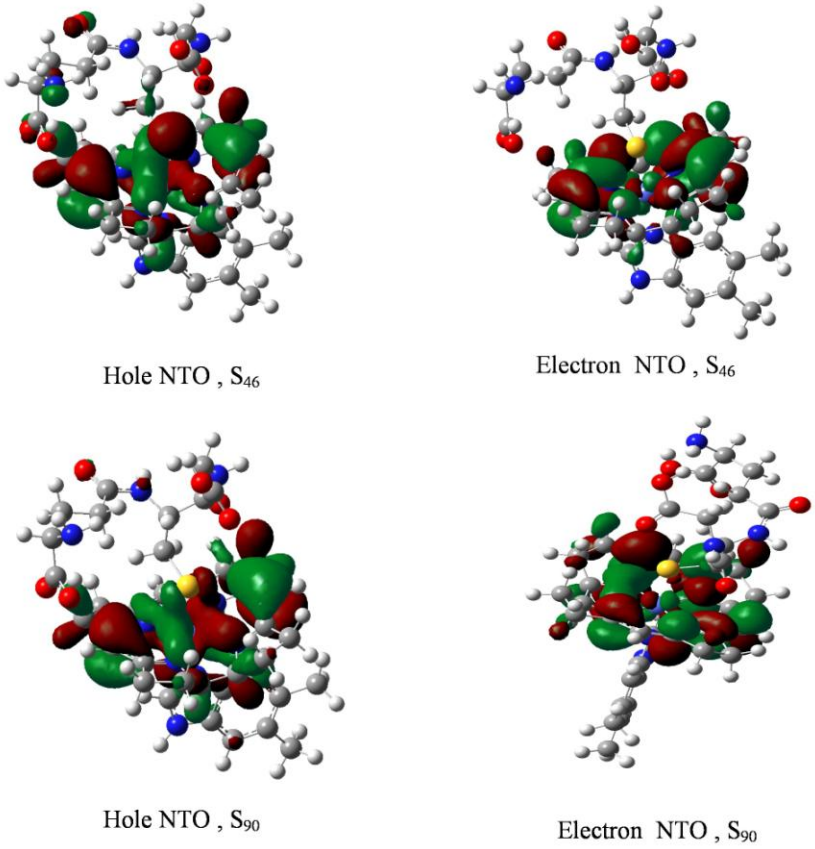

Figure 3.14. Electron and hole isosurfaces of Natural Transition Orbitals for states S_{24} and S_{85} from a BP86/6-311(d,p) calculation.

On the other hand, excited state S_{90} has a five centered bonding interactions involving Co and all four pyrrole ring Neq atoms and the S(py) with π(Co(yz))-S(py)) and π(Co-Neq) bonding from which density is withdrawn and donated to Co(dxz) and corrin π* in electron NTO as in seen in Fig. 3.14. This hole NTO exhibits the utility of the natural transition orbital analysis of electronic excitations since nine MOs contribute to the donor of excited state 90 with contributions of only 3% to 15% for any one MO making it impossible to understand this transitions from a molecular orbital analysis.

Table 3.7. NTOs for hole and electron isosurfaces from a BP86/6-311(d,p) calculation which are correlated with deconvoluted bands in the experiment absorption curve of gluthionylcobalamin.

band	State	E(eV)	λ(nm)	f	hole	electron
	1	1.638	756.9	0.001	σ(Neq-Co(dyz)-Neq) + Spy	Co(dyz)+ corr π*
583	3	2.1358	580.5	0.0337	σ(Co(dxz)+S(pz))+ corr π + Nax(pz)	Co(dxy) + corr π*
561	4	2.2562	549.52	0.0257	σ(Co(dxz)+S(pz)+ corr π+ Nax(pz)	Co(dz2*) + S(pz)*+ Nax(pz)*+ corr π*
	6	2.4321	509.79	0.0125	σ(Co(dxz)+Spy) + Bzm π+ corr π	Co(dyz) + corr π*
496	8	2.4962	496.7	0.0162	Co(dyz)+ S(py)	Co(dxz)+ corr π*
	9	2.519	492.2	0.025	π(Co(dyz)+S(pz)+corr π	Co(dx2-y2)+S(pz)*+π*
475	10	2.6228	472.72	0.0128	Co(dxz)+corr π+Bzm π	Co(dz2)+S(pz)*+Neq* + Nax(pz)*
456	12	2.7643	448.53	0.0052	σ(Co(dxz)+S(pz))+ corr π	Co(dx2-y2)* + corr π*
	18	2.9705	417.39	0.0283	σ(Co(dxz)+S(pz)+Nax(pz))+ gluO(py)+ Bzm π	Co(dyz) + corr π*
	20	3.0084	412.13	0.0266	σ(dxz+Spz)+corr π+ Nax(pz)	Co(dxz) +corr π*
408	21	3.0531	406.1	0.0167	π(Co(dxz)+ Nax(px))+glu+Bzm π	Co(dz2*)+S(pz)*+ Nax(pz)* corr π*
388	24	3.2196	385.09	0.0307	π(Co(dyz)+S(py))+ corr π	Co(dxz*) + corr π*
	25	3.2414	382.5	0.0139	σ(Co(dxz)+S(pz))+Nax(pz)+corr π	Co(dx2-y2)*+Bzm π*
	26	3.2639	379.86	0.0335	π(Co(dyz)+S(py))+corr π	Co(dxz) + corr π*
	27	3.2756	378.5	0.0154	Co(dyz) +S(py)	Co(dx2-y2) + corr π*
	29	3.301	375.59	0.0338	σ(Co(dxy)+S(pz))+ glu	Co(dz2*)+S(pz*)+Nax(pz*)
375	31	3.3527	369.81	0.0316	Co(dxy)+S(px)+ corr π+ glu	Co(dz2*)+S(pz*)+ Nax(pz*)
	37	3.5367	350.56	0.021	σ(Co(dx2-y2)+S(pz)+ Nax(pz))+corr π	Co(dyz*)+S(pz + Nax(pz*))+corr π*
357	40	3.5632	347.96	0.0111	Co(dyz) + S(py)	Glu π*
	46	3.6739	337.47	0.071	π(Co(yz)+S(py))+σ (Co(dyz)+Neq) +corr π	Co(dyz) + corr π*
330	52	3.7623	329.54	0.0255	Co(dxy)+corr π	Co(dx2-y2)+Bzm π* +π(Neq+C(pz)
	64	4.0155	308.76	0.0206	π(Co(dxz)+S(px))+ glu	Co(dxz) + corr π*
	66	4.0418	306.75	0.0256	π (Co(dyz)+S(py))+corr π	Co(dx2-y2) +corr π*
	67	4.0442	306.58	0.0164	Co(dxz) + glu	Co(dx2-y2) + Neq(sp2*)
304	71	4.1205	300.89	0.0326	Co(dxz) + corr π+Bzm	Co(dx2-y2) +corr π*
	85	4.3481	285.15	0.0842	π(Co(dyz)+S(py)) +corr π	Glu π*
	88	4.3554	284.67	0.0505	π(Co(dyz)+S(py))+ π (Co(dyz)+Neq(pz)) +corr π	Co(dxy)* + Neq(sp2*) + glu π*
296	89	4.3722	283.57	0.0648	σ(Co(dxz)+S(pz))+ Nax(pz)) + corr π	Co(dy2) + S(pz*)+ Nax(py*) + corr π*
280	90	4.4213	280.43	0.0426	π(Co(dyz)+S(py))+ π(Co-Neq(pz)) + corr π	Co(dxz)+ corr π*
279	93	4.46	277.99	0.0341	π(Co(dyz)+2Neq) +corr π	Co(dyz)+ corr π*
	96	4.4888	276.21	0.105	σ(Co(dyz)+S(pz))+ Bzm π	σ *(Co(dz2*) + S(pz*)) + Nax(px*) + corr π*
	97	4.4897	276.15	0.0302	Glu O(py)	σ *(Co(dz2*) + S(pz*))+ Nax(pz*))+ Neq(px*)
	99	4.5273	273.86	0.0208	Co(dx2-y2) + glu	Co(dxy) +corr π*
269	100	4.5313	273.62	0.0406	Co(dyz) + corr π + Bzm π	Co(dz2*) + S(pz*) + corr π*

IV. Summary and Conclusions

We have used DFT calculations to analyze geometry, bonding, and electronic transitions and to simulate UV-VIS and electronic CD spectra of the biologically important glutathionyl-cobalamin molecule.

The calculations in water (cpcm model) were clearly superior to the vacuum calculations in simulating the electronic spectra for MeCbl and GSCbl, whereas, for H2OCbl the simulation in vacuum was nearly the same as in water. For GSCbl we made an effort to make absolute fits of simulated to experimental spectra. In this regard, the BP86/6-311(d,p) in water calculations were a much better fit to the spectra than the B3LYP/6-311 (d,p) in water with respect to absolute intensity and absolute energy. We also concluded that the experimental deconvoluted band for H2OCbl at 497 nm, for MeCbl at 524 nm, and for GSCbl at 529 nm was a vibronic band since it was not found in the purely electronic calculations. With regard to the electronic CD spectra, it can be concluded that a more complete chemical model involving the side-chains is necessary to simulate a better fit to the differential extinction experimental results.

The nature of the electronic transitions and the bonding in the GSCbl macrocyclic metal complex can be very appropriately illustrated using the hole and electron natural transition orbital representation of R. L. Martin (7).

Chapter 4

Cyclic Voltammetry of Glutathionycobalamin and Spectrophotometry Titration to determine its Formation Constant Low pH

4.1 Electrochemistry of GS-Cbl

4.1.1 Introduction

Cobalamins are coordination complexes of Co(III), Co(II), Co(I) with a rich redox chemistry which can be explored with electrochemical techniques. The reduction of R-Cbl(III) involves the loss of the R- axial ligand at some point in the process since while R-Cbl(III) is a six-coordinate species, Cbl(II) is five coordinate, and Cbl(I) is four coordinate. Typically, the reduction of any R-Cbl will yield the same Cbl(II) and/or $Cbl(I)^-$ species. A question which is explored in this thesis is whether the electrochemistry of GS-Cbl is more like that where the R group is an inorganic species as in H_2O-Cbl(III) and CN-Cbl(III) or more like that where it is an organic species as in CH_3-Cbl(III). Since this is a major goal we first review in detail the electrochemistry of H_2O-Cbl(III) and CN-Cbl and alkyl-Cbl(III).

4.1.2 Background Electrochemistry of Vitamin B_{12} analogs

Under physiological conditions, the cobalt center in vitamin B_{12} derivatives has been observed in three different oxidation states, which display quite different chemical properties. Roughly speaking, Cbl(III) appears as an electrophile, Cbl(II) as a radical, and Cbl(I) as a nucleophile. Oxidoreductive conversions between the three oxidation states

are thus of key importance in the chemistry of vitamin B_{12}. Using electrochemistry these three species can be formed under controlled conditions and electrochemical methods became a particularly valuable source of information for investigating the redox chemistry of vitamin B_{12} and its derivatives.

Diehl and his coworkers using polarography were the first to report the electrochemistry of vitamin B_{12} analogs (1). In Vitamin $B_{12,}$ the R- group in R-Cbl is the cynanide and this is the form in which it was first isolated. Early work in this field used mostly polarography as a technique and concerned mainly cyano- and aquocobalamins (2, 3). Polargraphic data were also gathered concerning deoxyadenosyl-, methyl-, and other alkylcobalamins (2). However, specific adsorption on mercury, especially with the Co(II) complexes, is particularly important and hard to prevent. Later on, with the use of solid electrodes, such as platinum, gold, and glassy carbon, the cyclic voltammetry, CV, method was applied to carry out a considerably more extensive study of the electrochemical parameters in a variety of B_{12} derivatives (4, 5, 6, 7). More recently , potential step methods, UV-VIS spectroelectrochemistry, as-well-as CV have been applied to understand the electrochemical behavior of vitamin B_{12} (cyanocob(III)alamin, vitamin B_{12a} (aquocob(III)alamin), vitamin B_{12r} (cob(II)alamin), vitamin B_{12s} (Cob(I)alamin), and alkyl cobalamins and cobinamides as reviewed by Lexa and Saveant (8) and Halpern (9). The thermodynamics and kinetics of the (Cbl(III)) / (Cbl(II)) and (Cbl(II)/(Cbl(I)) couples have been worked out including the effect of pH (10), From a study of these redox potentials , Birke and coworkers were the first to show (3) that the disproportionation of (Cbl(II)) had equilibrium and kinetic constants such as to invalidate

disproportionation as a pathway to Cbl(I) formation. Kenyhercz et al. were the first to use a spectroelectrochemical cell to study aquocobalamin and its derivatives (10).

4.1.3. Electrochemical studies of aquocob(III)alamin and cyanocob(III)alamin

4.1.3.1 Electrochemical studies of aquocob(III)alamin

Lexa and Saveant (8) carried out a series of ground breaking investigations dealing with the electrochemistry of aquocobalamin and cyanocobalamin. They studied the redox properties of aquocoalamin at different pH values. Figure 4-1 shows the E^0 vs pH of the B_{12a}-B_{12r}-B_{12s} system in water. Below pH 2.9, a single reversible wave is observed whatever the sweep rate, and there was no adsorption of B_{12r}. When the pH is higher than 3, mercury can still be employed as the electrode material since a solvent like Me_2SO adequately suppress the adsorption of B_{12r}. However, under this condition, the scan rate ν showed effects on the cyclic voltammogram. At high sweep rate ($\nu > 100$ V/s), two successive cathodic peaks are observed. The ratio of their heights is independent of ν. Upon the decrease of the sweep rate, the first peak increases at the expense of the second. At very low sweep rates ($\nu < 0.1$ V/s) the second peak disappears. This entire phenomenon has been explained by the role of the α-axial base-off/base-on equilibrium reaction in the redox chemistry of B_{12r} (Cbl(II) to B_{12s} $(Cbl(I)^-)$. Below pH 2.9, the nucleotide side Bz chain comes off being replaced by water at Co(II) in the α-position, and the base-off form completely predominates at equilibrium giving a single reversible wave. When the pH is higher than 3, the major component of the reduced form

B_{12r} is the base-on form, and it's harder to be reduced, which gives rise to the second peak. The peak height ratio corresponds to the equilibrium amount of the two forms under high sweep rate. However, upon the decrease of the sweep rate, an additional component results from the dynamic conversion of the base-on form into the more easily reducible base-off form.

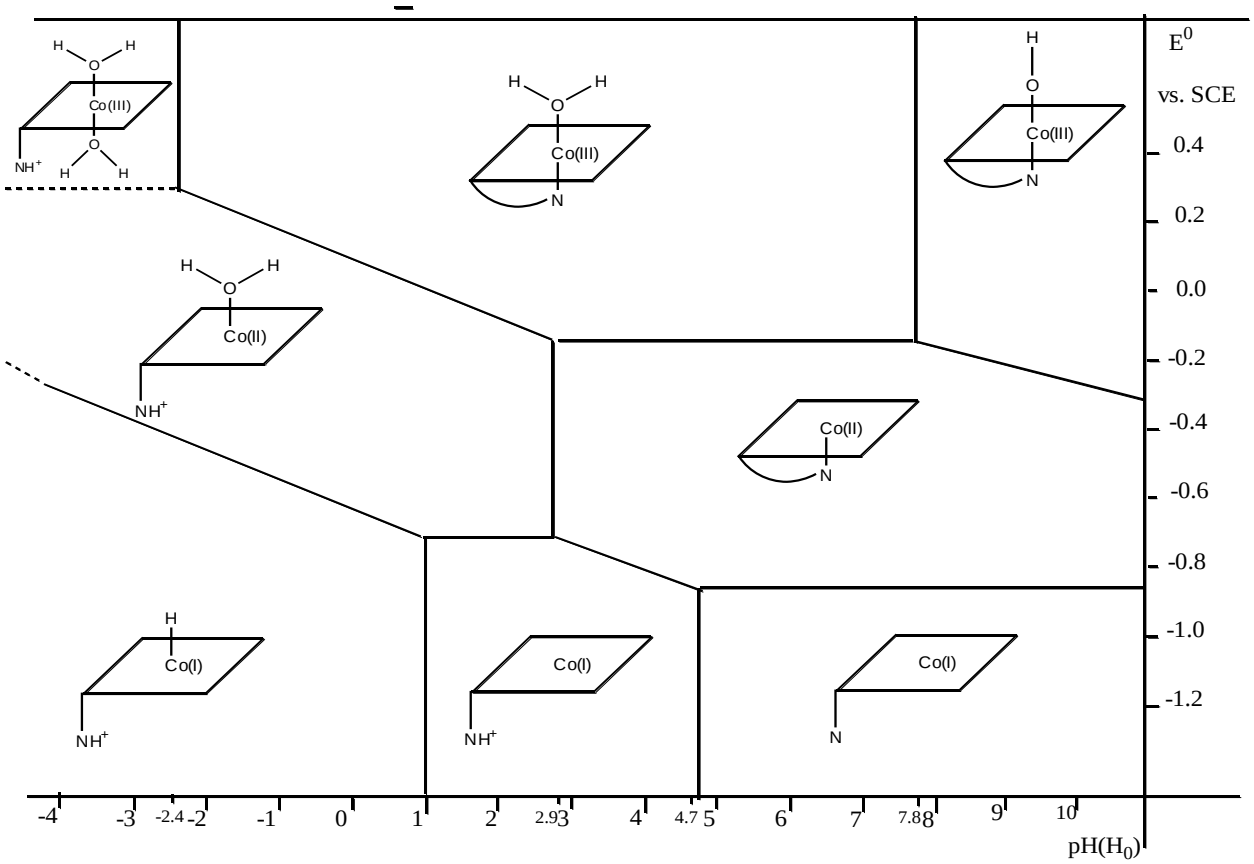

Figure 4.1 E^0-pH diagram of the vitaminb B_{12a}-B_{12r}-B_{12s} in water at 22°C. According to Lexa and Saveant (8).

The base-off/base-on reaction plays a much less important role in the reduction of B_{12a}/B_{12r} Co(III)/Co(II) couple where B_{12a} is shifted to the base-on form. The E^o- pH data were obtained mainly from potentiostatic measurements with a plantinum electrode and

with electrolysis times long enough to allow for complete equilibrium, followed spectroscopically by UV/VIS analysis. In the case of B_{12a}, the equilibrium is very much in favor of the base-on form (~10^7) and the base-on/base-off conversion is too slow for any significant reduction through the base-off form to occur. It appears only at pH 0 and below. A rather different situation is found above pH 7 where the aquo/hydroxocobal(III)alamin , H2O-Cbl(III)$^+$/OH-Cbl(III), equilibrium is involved in the reduction of B_{12a}. The aquo complex is easier to reduce than the hydroxo form for both thermodynamic and kinetic reasons. A kinetic current involving the dynamic conversion of the hydroxo into the aquo complex is found at pH values above the pKa(7.8) of B_{12a} and only involves protonation of the OH^- ligand rather than base change at the cobalt center .

Lexa and Saveant and coworkers also studied the kinetic effects in the B12a-B_{12r}-B_{12s} redox system (11, 12, 13). The complete mechanistic scheme based on cyclic voltammetry and rotating disk electrode voltammetry on gold, glassy carbon, and mercury electrodes has been discussed by Saveant and de Tacconi (14) for the kinetic characteristics of B_{12a}-B_{12r}-B_{12s} systems. The thermodynamics and kinetics of most of steps involved in the redox pattern of B_{12a}-B_{12r}-B_{12s} oxido-reduction have been delineated:

(1) In neutral and weak acidic media (pH=3~8), B_{12a}/B_{12r} and B_{12r}/B_{12s} redox couples are all base-on, with two reduction peaks on the cyclic voltammogram. The first peak is the reduction of B_{12a} to B_{12s} accompanied by the rapid gain or lose H_2O at β-axial site. Kinetic characteristics such as transfer coefficient α, standard rate constant k_s and

standard redox potential E^0 have been tabulated. The voltammograms obtained on various electrode materials at the same pH exhibited very little difference.

(2) In basic media (pH> 8), the hydroxo form of B12a tends to predominate over the aquo form at equilibrium. This results first in a negative shift of the first CV peak potential with pH. Then while still moving negatively, the first wave decreases at the expense of the second wave. The sum of the two wave heights remains constant and corresponds to an overall electron exchange of 2 faradays/mol. The height of the first wave reflects the kinetics and thermodynamics of the antecedent chemical reaction while the location of the wave depends upon these parameters as well as upon the charge-transfer kinetics. The aquo form being easier to reduce than the hydroxo form, it follows that the first cathodic wave features the reduction of B_{12a} through its aquo form. The second wave features the direct reduction of the hydroxo form, which occurs at a potential very close to the reduction potential of B_{12r} to B_{12s} from a solution of B_{12r}. Direct electron transfer to hydroxo-B_{12a} leads to a B_{12r} with an OH^- as sixth ligand. This is obviously an unstable species which immediately decomposes into the standard base-on B_{12r} form which is reduced to B_{12s} at the same potential.

(3) In strong acid media (pH< 3), at a glassy carbon electrode the B_{12a} to B_{12r} and B_{12r} to B_{12s} reduction peaks still can be observed, with a positive shift of the anodic peak. In this pH range , a small prewave appears on the first canthodic scan, its height increases when the pH decreases. During the second cathodic scan the height of the prewave is higher than during the first and an almost reversible system is thus obtained around +0.4 volts vs. SCE.. The appearance of the prewave is typical of a reaction sequence involving a chemical reaction proceeding the electron transfer process. This

suggests that a part of the reduction occurs through the protonated base-off B_{12a} and the redox couple around 0.4 volts is the reduction/oxidation of base-off B_{12a} /base-off B_{12r}.

4.1.3.2 Electrochemistry of cyanocobalamin (vitamin B_{12})

4.1.3.3

Lexa, Saveant, and Zickler (6) studied the electrochemistry of cyanocobalamin (vitamin B_{12}), and the thermodynamics of the system was derived from the results of steady state spectroelectrochemical experiments. The description of the thermodynamic pathways that are followed under dynamic conditions and how they change with the CN^- concentration was derived in the context of cyclic voltammetry and are shown in Figure 4-2.

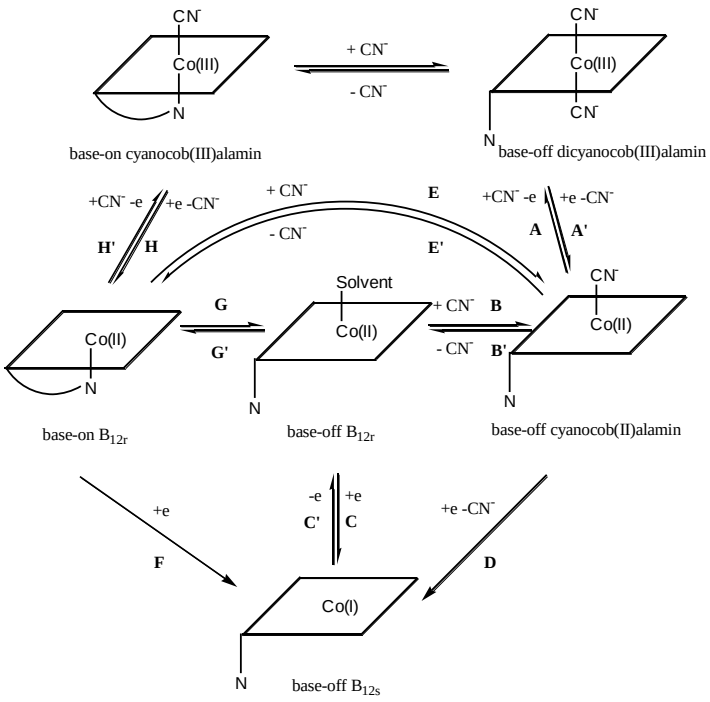

Figure 4.2 Cyanocobalamin(vitamin B_{12}) redox chemistry according to ref.6.

When the CN^- concentration is three to four times that of cyanocobalamin, the reduction starts from the dicyanocob(III)alamin yielding in a first stage cyanocob(II)alamin (pathway A), with concomitant loss of a CN^- under one electron transfer. Two competitive pathways are then followed for the further reduction to the Co(I) form: Pathway B plus C, which predominates at low CN^- concentration and low sweep rate give rise to a total two electron ECE process. Direct reduction of cyanocob(II)alamin, pathway D, predominates at high CN^- concentration and high sweep rate and occurs with electron transfer at a potential more negative than pathway A giving rise to a separated one-electron wave. Starting from cyanocob(III)alamin without addition of CN^-, the reaction pathway is another two electron ECE process(pathway H+G+C). Pathway F can only be observed under high sweep rates and low temperatures. When the CN^- concentration is between zero and three times that of the starting cyanocobalamin, there is a competition between the two reaction pathways (pathway A+B+C and pathway H+G+C), and the conversion rate of the second into the first (pathway E) is too slow to interfere into the reduction process. Starting from the Co(I) form, the reoxidation process follows the C′+B′ pathway. In the presence of CN^-, cyanocob(II)alamin is then reoxidized into dicyanocob(III)alamin, but in the absence of CN^-, cyanocob(II)alamin is reoxidized directly into base-on cyanocob(III)alamin. Potential step chronoamperometry has also been used to study this reaction especially the ECE pathways (5). More recently the reaction has been studied in acidic media (15).

Since thiolate anions like GS^- strongly bind to Cbl(III), their electrochemistry could be similar to CN-Cbl(III). Lexa and co-workers (16) studied GS-Cbl(III) on a glassy carbon electrode at pH 6.4 BR buffer by adding GSH to an aquo-Cbl(III) solution.

At stoichiometric amounts of GSH:H2OCbl(III) the Cbl(III)/Cbl(II) wave disappears and has merged with the Cbl(II)/Cbl(I) wave which shifts to more negative potentials. They also found a similar pattern in the voltammetry when GSH was added to aquo-Cbl(III) adsorbed on a pyrolytic electrode forming adsorbed GS-Cbl(III). Furthermore they also prepared Cbl(II) by controlled potential reduction and added it oxygen free to an optical cell. The spectrum of Cbl(II) did not change when GSH was subsequently added to the optical cell. Thus Cbl(II) was found to be stable at high concentrations of glutathione unlike the case of CN^-. They also concluded from equilibrium studies that GS-Cbl(III) is in the base-on form. Finally, without any quantitative calculation but on the qualitative result that in the electrochemical titration of H2O-Cbl(III) with GSH the second wave grows as the first wave diminishes, they suggest that "glutathionylCo(III)balamin seems to be reduced directly in a two-electron step." This assertion is further investigated in this thesis.

4.1.4 Electrochemistry of alkylcobalamin and its derivatives

Because of the role of methylcobalamin, Me-Cbl(III) and 5′-deoxyadenosylcobalamin (coenzyme B_{12} or Ado-Cbl(II)) as cofactors in enzymes, the electrochemistry of these alkylcobalamin and their derivatives has attracted much interest. However, measurements are complicated due to rapid and irreversible loss of the organic ligand upon reduction of alkyl-cobalmain derivatives. Alkylcobalamines and alkylcobinamides (cobalamins with the nucleoside side-chain cleaved) behave differently from other B_{12}-Co(III) complexes bearing strong axial ligands such as OH^- or CN^-. The

reduction potential of alkyl-Cbls are quite negative, most of them more negative than –1.3V vs. SCE. To slow down the electrode processes, low temperatures were used to obtain pertinent thermodynamic and kinetic information.

The early work on alkylcobalamin was done by polarography by Hogenkamp and Holmes (2) who studied ten types of alkylcobalamins and alkylcobinamides and found that most of the reduction potential were between –1.37V to –1.39V. However, when the alkyl groups are CH_2COOH and CH_2COOMe, the standard reduction potentials are –0.84V and –1.14V respectively, which is much more positive than other alkylcobalamins and alkylcobinamides. It was thought to be related to the electron withdrawal effect of the COOH group. Other groups have studied alkylcobalamin and alkylcobinamides with exceptional positive reduction potential and high reversibility, but it was thought to be caused by the adsorption of alkylcobalamin onto the mercury surface.

For alkylcobalamins , alkylcobinamides , and model compounds, a quantitative understanding of the electrochemistry and axial ligand effects are less complete than when the β-axial ligand is an inorganic species. A single irreversible cathodic wave was observed by Lexa and Saveant (7) at low sweep rates in non aqueous medium corresponding to the reductive cleavage of the cobalt-carbon bond. Upon raising the sweep rate, the anodic wave grows in, clearly showing the existence of a one-electron intermediate before cleavage of the cobalt-carbon bond to form $B_{12s}(Co^{1+})$ and methyl radical. This reaction can be simply expressed by the reaction sequence :

$$R\text{-}B_{12}Co^{3+} + e^- \longrightarrow (R\text{-}B_{12})^- \xrightarrow{k} (Co^{1+}B_{12s})^- + R\cdot$$

The rate constant for the following bond break reaction k is 1200 s^{-1} at –30°C .

Reduction with the alky-cobalamin derivatives in aqueous media on mercury is complicated by adsorption effects; however, Birke and Kim (17) were able to study the thermodynamics and kinetics of methyl- and adenosylcobalamin for the reductive cleavage reaction by using a surfactant to lower the cobalamin adsorption. The mechanism of this reaction at an electrode was first suggested by Lexa and Saveant using rapid sweep CV for methycobalamin and methylcobinamide in 1:1 DMF-1-propanol at –20°C (5). Since the electrode process appears to involve a one electron addition and since B_{12s} $(Cbl(I)^{-})$ is detected electrochemically , the existence of the one electron adduct was strongly indicated. The lifetimes of this intermediate species varies from 0.1 to $4x10^{-4}$ s at temperatures between -20 and 19 ^{o}C in nonaqueous solutions. In the investigation of Kim and Birke (17) of the reductive cleavage mechanism of methylcobalamin and adenosylcobalamin in aqueous solution , the rate of the bond breaking is rather slow for methylcobalamin, 0.37 s^{-1}, but much faster for adenosylcobalamin, $2.7x10^{3}s^{-1}$.

More recently Finke and Martin (18, 19, 20) have shown by thermolysis that homolytic Co(III)-C cleavage is very slow compared with the rate of homolytic cleavage following electron transfer, ET, as in above studies of methyl and adenosylcobalamin. It was thought that addition of an electron to the σ^{*} Co-C orbital of the molecule leads to an enhancement in the bond cleavage rate of 10^{12} to 10^{15} ; however, recent molecular orbital calculations show that addition of an electron goes into a π^{*} corrin ring orbital. Theoretical electronic structure calculations from the group of Birke and coworkers show that a one-electron addition to R-cobalamins goes into a LUMO orbital that is a corrin π^{*} orbital (21, 22, 23). In another electrochemical study of this reaction (24), it was suggested the electron

first goes in to this corrin π* orbital but then jumps into a Co-C σ* orbital causing a half-bond reduction of the Co-C bond strength (as suggested by Finke and coworkers (20, 21). The four orbitals above the SOMO of the one-electron adduct of methylcobalamin were examined by DFT calculations of this doublet state and do not represent this antibonding σ * orbital. What appears to be happening is a dissociative electron transfer mechanism which involves a step-wise intra- molecular ET from the σ * corrin orbital to the Co-C σ* orbital. The initial ET step from the electrode to methylcobalamin was modeled as a nonadiabatic process and the electronic coupling matrix element calculated. The intra-molecular ET occurs as the Co-C bond vibrates and vibronic coupling lowers the Co-C σ* orbital as the bond stretches allowing the step-wise intra-molecular ET and the Co-C bond reductive cleavage reaction (23).

A mechanism for the electrochemical reductive cleavage of methylcobalamin was proposed by Spataru and Birke (22) and parameters obtained by digital simulation of the electrode process.

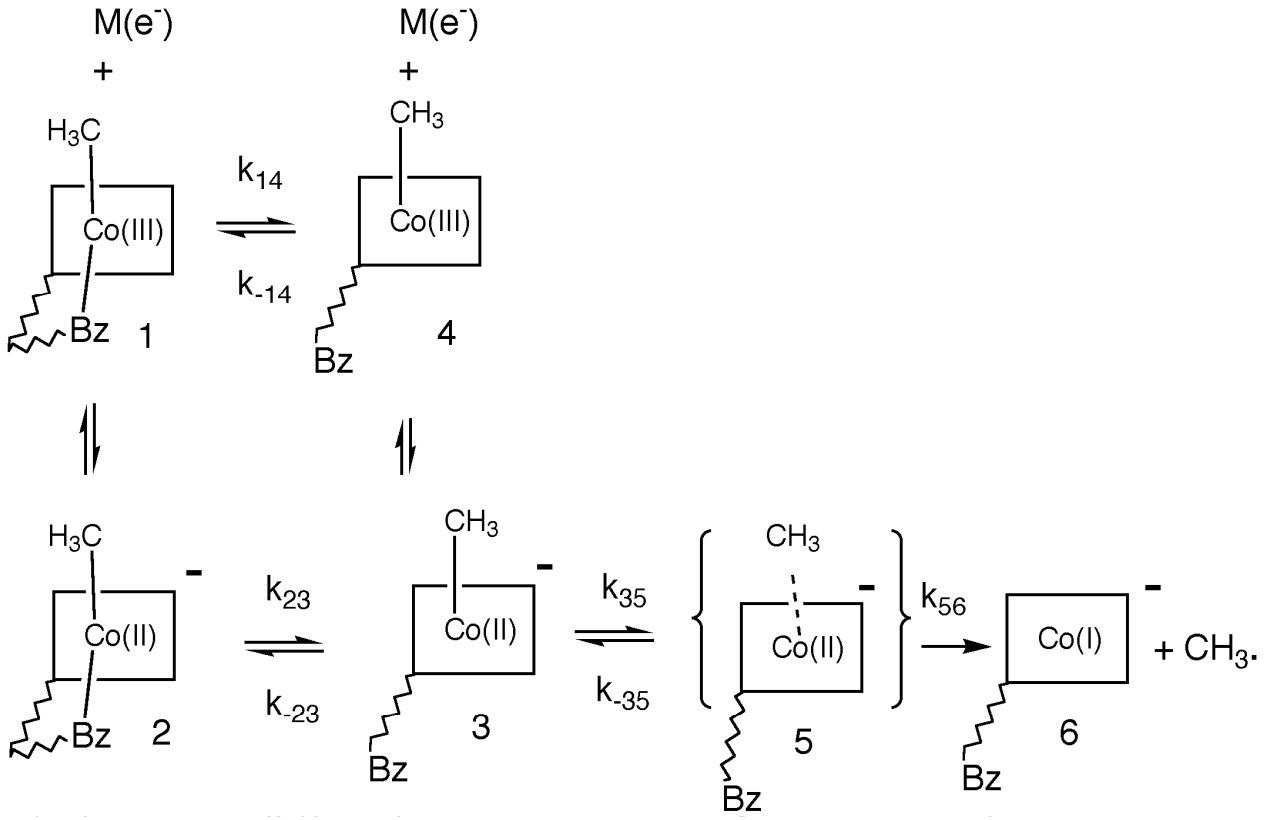

Figure 4.3. Mechanism of Reductive Cleavage of Methyl Cobalamin. Here $M(e^-)$ is the electron in the metal electrode.

The above scheme is modified from that of Lexa and Savéant (5) which did not explicitly indicate the scheme of squares and which had the bond cleavage from both a base-on species **2** and a base-off species **3** one electron reduced methylcobalamin $[Me\text{-}Cbl]^-$. Conversely in the above scheme, the cleavage occurs from only the base-off species which is then the channel leading to an irreversible chemical step. The parallel step with C-Co bond breaking from species **2** was not included in the mechanism since electronic structure calculations show that the Me-Co dissociation energy is much less from the base-off species **3** than from the base-on species **2**. The paramerter set (23) that was found in the best visual fit to the CV curves is the following:

E^0_{12} = -1.55 V and E^0_{43} = -1.42 V both vs. the aqueous $Ag/AgCl/Cl^-$(3M) ref. elec.

k^o_{12} = 0.050 cm/s , □□□ = 0.77 and k^o_{43}= 0.050 cm/s , □□□ = 0.50

K_{14} = 0.0124, K_{23} =2.0 , and K_{35}= 0.15

k_{14} = 124. s^{-1}, k_{-14} = 1.0 x10^4 s^{-1} ; k_{23} = 2.0 x 10^4 s^{-1}, k_{-23} = 1.0 x10^4 s^{-1} ; k_{35} = 1.5 x 10^3 s^{-1},

k_{-35} = 1.0 x10^4 s^{-1}, k_{56} = 1.0 x10^4 s^{-1}, k_{-56} = 0.0 s^{-1}, D = 3.0 x10^{-6} cm^2/s for all Cbl species , A = 0.028 cm^2.

The above parameters were obtained for an 80:20 solvent mixture of DMF/MeOH. Although a detailed examination of the solvation effects on the formation and break-up of the caged species was not undertaken, the authors tentatively concluded that it is k_{56} for bond breaking from a solvent cage which is most affected by changes in the solvent mixtures. The formation of the methyl radical/$Cbl(I)^-$ cage species in step 35 is by an intramolecular electron transfer step and it was argued that this step involves less solvation energy change than the break-up of the cage to form the separated methyl radical and $Cbl(I)^-$ species.

The electrochemical studies of one electron addition followed by Co-C bond breaking could model a transition state of a single electron transfer, SET , a possible mechanism in methionine synthase turn-over. An ET mechanism which results in a ground state radical anion was originally thought to be unlikely for the enzymatic reactions because of the very negative reduction potential (-1.0 V to -1.6 V vs. SCE) required , and a nucleophilic substitution , S_N2 , reaction at the CH_3-Co site has been a more preferred mechanism for methyl transfer. The ET mechanism involves a transfer of an electron from the homocysteine thiolate, $R\text{-}S^-$, to the CH_3-Co(III)Cbl, forming a species at the active site [$R\text{-}S\bullet$ $(CH_3\text{-}Co(II)Cbl)^-$] in the transition state of a methyl transfer mechanism of B_{12}-

methionine synthase. The $(CH_3\text{-}Co(II)Cbl)^-$ part of this species is the same intermediate which is implied by fast scan cyclic voltammetry. Coupling of R-S• and CH_3• radicals at active site of the enzyme would give $R^{-}S^{-}CH_3$, i.e., methionine and vitamin B_{12s}.

4.1.3 Vitamin B_{12} Catalyzed Processes

Finally we mention the phenomenon of B12 catalyzed process and especially that of hydrogen reduction catalyzed by reduced vitamin B12 species which can occur at low pH. Birke and coworkers have investigated the B_{12}-catalyzed reduction of H^+ at a Hg electrode (25). In these reactions, cobalamin reduction at the electrode produces B_{12s} $Cbl(I)^-$ which chemically reacts with hydrogen ion in solution with the recycling of the oxidized cobalamin catalyst by further reduction. There are other substrates which have not been studied with the catalytic redox cycle electrochemically but have been shown to react with vitamin B_{12S} in a redox reaction in vitro including nitrous oxide (26), oxyhalogens (27), and hydroxylamine derivatives (28). Additional electro-catalyzed processes were studied in Zagal's group (29, 30, 31, 32) which found that vitamin B12 can be absorbed on ordinary pyrolytic graphite (OPG) for the electroreduction of O_2, for the oxidation of cysteine and glutathione, and for the reduction of cystine.

4.1.6 Experimental Voltammetry Details

The CV experiments were performed with the CH 660A workstation. A three electrodes configuraton was used in all experiments. The working electrodes were a mercury drop from a BAS controlled growth Hg electrode (CGME) or a BAS 3 mm

diameter glassy carbon electrode. A Ag/AgCl/Cl (3M) electrode was used as the reference electrode and a platinum electrode was used as the counter electrode. All potentials are quoted versus the above reference electrode. Aquocobalamin(hydroxy-cobalamin·HCl) also called vitamin B_{12a} and glutathione were obtained from Sigma-Aldrich Chemical Co. in < 97% purity. Glutathionylcobalamin was made up in solution by adding a slight excess of glutathione to aquocobalamin (≈ 1:1 molar ratio). The UV-VIS spectra for these GSCbl solutions were identical to solutions made from solid authentic GSCbl kindly supplied by Nicola Brasch. The concentration of B12 compounds was determined spectrophotochemically in solution by adding excess cyanide which converts them to dicyanocob(III)alamin and using the latter's know extinction coefficients. Deiononized–distilled water was used to make up all solutions and all chemicals including those to make up buffers and salt solutions were analytical reagent grade. The pH buffers were made from different ratios of acetic acid/sodium acetate.

4.1.7 CV Results

We only report on CV results at an acid pH since adsorption of the cobalamin species is greatly lowered under these conditions. Figure 4.4 shows the CV curves of 0.453 mM GS-Cbl prepared from B12a and GSH in a 0.1 M pH 4 acetate buffer. The curves here are measured as a function of rather low values of scan rate using a BAS controlled growth mercury electrode (CGME) under stationary drop mercury electrode conditions (SDME). Only the region between around -0.6 V to -1.2V vs Ag/AgCl is shown because at potentials more positive to -0.3V there is as adsorption wave on the Hg

electrode due to the adsorption of the slight excess of GSH in the solution. It is observed that at starting around -0.9 V the GS-Cbl reduction waves show both a forward and reverse wave and they have a quasireversible nature. Table 4.1 shows the cathodic peak current, ipc, on the SDME over a larger range of scan rates. Figure 4.5 is log peak current versus log scan rate plot which shows that this is a diffusion controlled process (scan rate $^{0.408}$ dependence). The shift to more negative potentials with scan rate may include an IR drop effect and indicates a quasireversible electron transfer process. At the scan rate of 0.5 V/s , the hint of a second peak at -1.1V is observed in Fig. 4.4 This is probably the catalytic H^+ wave as was observed on Hg electrodes previously (25).

In order to estimate the number of electrons transfer in the process, the ratio of cathodic to anodic peak currents were measured. Extrapolating the reverse peak current using the decay of the forward scan at about -1.12 V to the reverse peak current gives rations of i_{pc}/ i_{pa} of 1.3, 1.2, and 1.0 for the black(0.05V/s) , red (0.2 V/s) and green (0.1 V/s) scan rates. Because of the second peak for the blue curve at 0.5 V/s scan rate it could not be used to get this ratio. It would appear that the number of electrons transferred is closer to one than two on these curves.

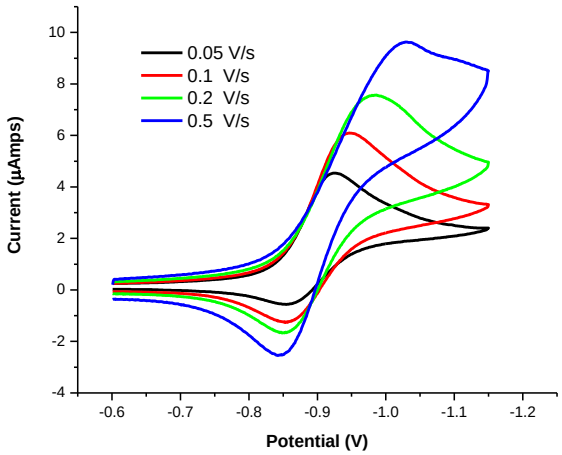

Figure 4.4 CV of 0.45 mM glutathionylcobalamin at pH 4 in a 0.10 M acetate buffer on SDME (Hg) electrode

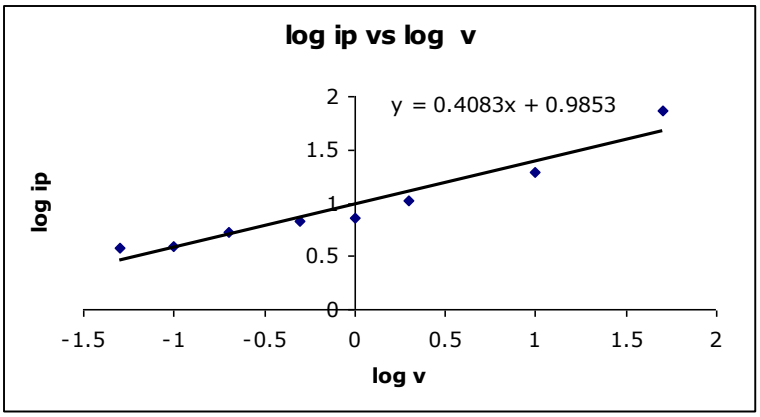

Figure 4.5 Log-log plot CVdata for the same conditions as in Fig.4.4 of glutathionylcobalamin on SDME (Hg) electrode

Table 4.1 Scan rate, peak potential and current

ν(V/sec)	Ep_c (V)	Ip(µA)
0.05	-0.963	3.78
0.1	-0.996	3.92
0.2	-1.034	5.29
0.5	-1.054	6.78
1	-1.054	7.2
2	-1.054	10.6
10	-1.082	19.3
50	-1.12	73.4

A similar cyclic voltammetry study was made on polished glassy carbon electrodes as given in Figure 4.6. Here it is possible to scan from +0.5 V to around -1.2 V because there are no waves from adsorbed GSH. Also one see that on the negative going scan at 0.05 V/sec there is no reduction due to aquo-Cbl around 0 V; however, there is one reduction wave at -0.917 V which is coupled with an oxidation wave at -0.854 V, giving a 63 mV difference. As the scan rate increases the voltage difference between cathodic and anodic peaks grow (122 mV at 0.2 V/s) again suggesting quasi-reversibility. Also it is observed that this first oxidation peak is nearly at the same potential on the reverse scan and does not shift as much with scan rate as does the cathodic peak. This potential coincides with the

B_{12s} (Cbl(I)$^-$) base-off $\rightarrow$ B_{12r} (Cbl(II)) base-on + e^-

one electron oxidation and the second oxidation between -0.05 V and 0.0 V coincides with the

B_{12r} (Cbl(II)$^-$) base-on$\rightarrow$ B_{12a} (Cbl(III)) base-on + e^-

one electron oxidation as illustrated in the E^0 vs pH plot in Figure 4.1.

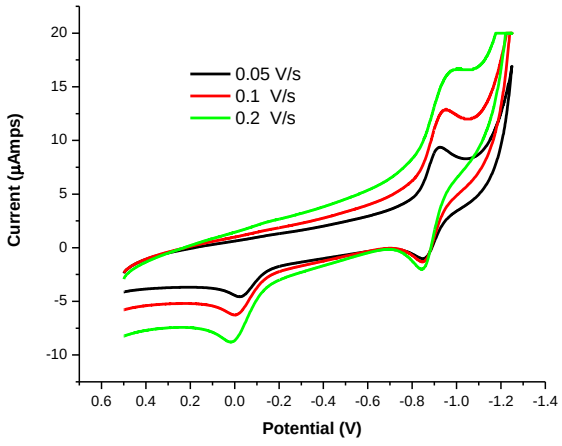

Figure 4.6 CV of 0.5 mM glutathionylcobalamin on GC electrode at pH 4 in 0.10 M acetate buffer

4.2 Simulation of electrochemical mechanism

The main question concerning the electrochemical process is whether it involves a 2 or 1 electron transfer mechanism. If it is a 2-electron transfer it would be similar to the reduction mechanism of CNCbl as discussed in 4.1.1(2). On the other hand, if it is 1-electron transfer it would be similar to the reduction mechanism of alkyl-Cbl as discussed in 4.1.2. Considering the ratio of the cathodic to anodic currents on mercury it appears to be the 1-electron mechanism. This conclusion can be strengthening by the simulating of the electrode process. The two mechanisms are shown below in Fig. 4.7.

Mechanism I (one electron reduction)

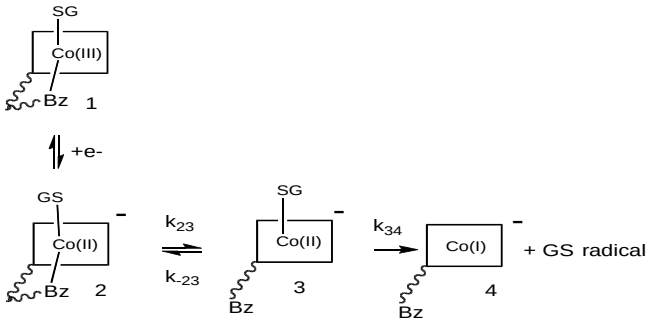

Mechanism II (two electron reduction)

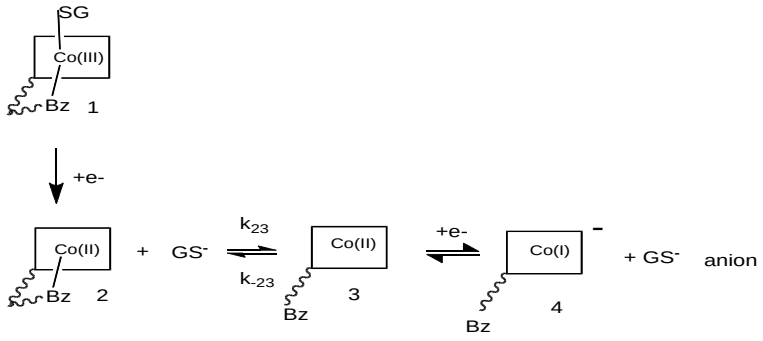

Figure 4.7 Mechanism I with the formation of GS· radical, and mechanism II with the formation of GS^- anion.

In both mechanisms we consider only the base-on form of GSCbl(III) as in species 1 (Figure 4.7). Also in both mechanisms the reduced Cbl species goes from the base-on to the base-off form (2 ⇌ 3). Two representative simulations of mechanisms I and II with the same concentrations and diffusion coefficients are shown in Figure 4.8. Known values for the Cbl(III)/Cbl(II) (-.050 V) and Cbl(II)/Cbl(I) (-0.870 V) were used in both. In the first mechanism the value for the GSCbl(III) reduction potential was -0.890 V and in the second it was -0.94 V. Also the equilibrium constant, K_{23}, was 100 in both cases. All parameters are given in Appendix V. The simulation with other representative parameters was made using the CVSim program of Gosser (33). The distinguishing feature of the two mechanisms is the ratio of cathodic peak current to anodic peak current at around -1.0 V. The blue curve is for the 2-electron mechanism and the purple curve is for the 1-electron mechanism. Two oxidation peaks on the curve are very close to the potentials found on the GC electrode with GSCbl figure 4.6. In mechanism II the cathodic current is significantly higher and two peaks appear even though the reduction potentials for the 2-electron steps are the same.

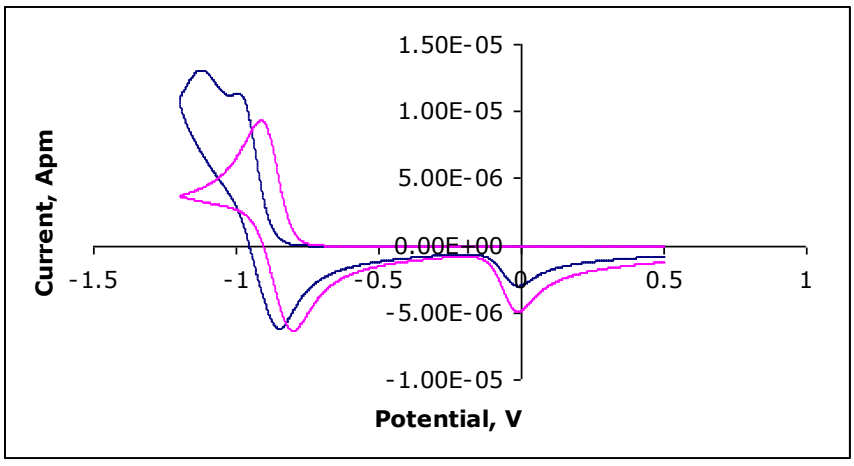

Figure 4.8 Simulation of the two electrode mechanisms; mechanism I: purple, mechanism II: blue.

In figure 4.9 we compare a simulation with the experimental CV curve. Data from the experimental voltametry of GSCbl on the GC electrode under the same conditions as on Fig. 4.6 was used for a visual comparison with the simulated voltammograms. As seen in Fig 4.6 there is considerable background current which was subtracted out in order to make a comparison of the simulated with the experimental voltammogram. The best visual fit of the simulated to the experimental voltamogram is given in Fig. 4.9 for mechanism I.

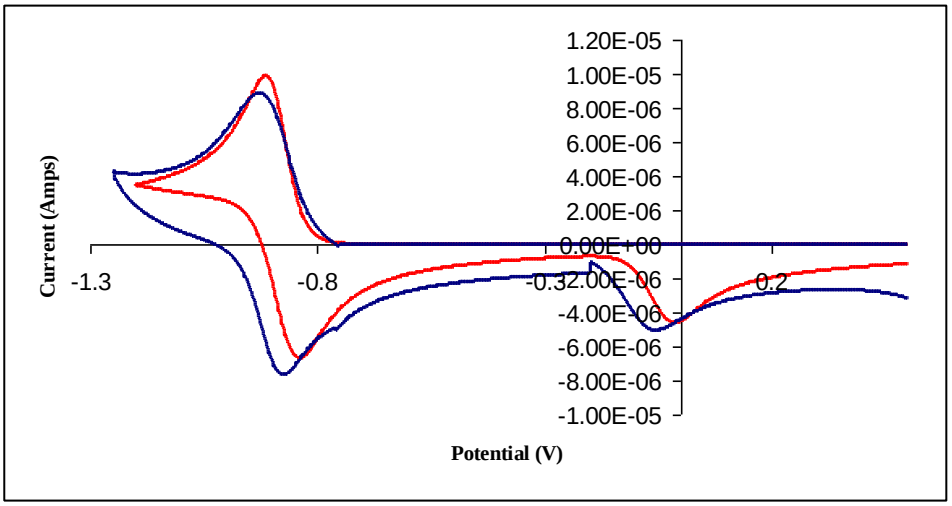

Figure 4.9 Simulated and experimental CV of GS-Cbl on Glassy carbon electrode using CVSim. Experimental CV: dark blue; simulated CV: red.

The following values were used for simulation according to the notation in Figure 4.7 (not shown in Figure 4.7 are vitamin B12a and B12r species which involved in re-oxidation):

E^0_{12} = -0.890 V, $E^0_{B12a/B12r}$ = -0.050 V, $E^0_{B12r/B12s}$ = -0.870 V all vs. the aqueous Ag/AgCl/Cl^-(3M) ref. elec.
k^o_{12} = 0.005 cm/s , □□□ = 0.75; $k^o_{a/r}$= 0.005 cm/s , □$_{a/r}$ = 0.50; $k^o_{r/s}$= 0.010 cm/s , □$_{r/s}$ = 0.75
k_{23} = 1.0 x 10^2 s^{-1}, k_{-23} = 1.0 s^{-1} ; K=1.0 x 10^2

[GS-Cbl] =0.453M. D = 3.0 x10^{-6} cm^2/s for all Cbl species,

The electrode area was used as an adjustable parameter to give simulated currents of the right order of magnitude. The chemical step 34 is considered irreversible and using a high value of k_{34} in the calculation does not change the above simulation. As it is seen from Figure 4.9 there is reasonably good fit of the simulated and experimental peak potentials. The main difference between the simulated and experimental CV curves is that the interfacial capacitance was not used in the simulation but is noticeable on the experimental curve right after the potential scan is reversed. Figure 4.10 shows a comparison of the simululation using mechanism I with the experimental CV results on the SDME and similar parameters were used in the simulation on the GC electrode except for changes in the charge transfer coeffients. The background current was subtracted from the experimental CV. All parameters for the simulation in Fig. 4.10 are given in Appendix V.

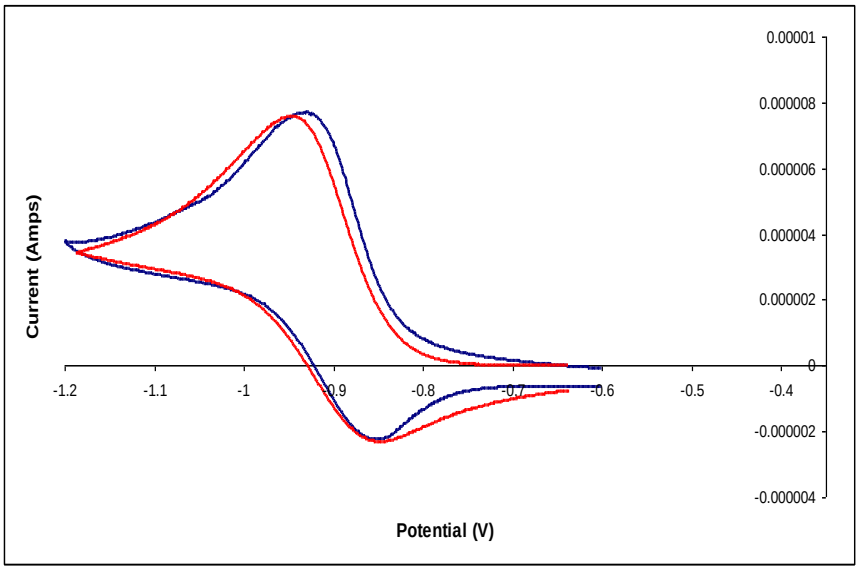

Figure 4.10 Simulated and experimental CV of GS-Cbl on SDME using CVSim; experimental CV: blue; simulated CV: red.

4.3 Spectrophotometric titration of aquocobalamin with glutathione

4.3.1 Experimental details

Aquocobalamin (hydroxy-cobalamin·HCl) and glutathione were obtained from Sigma-Aldrich Chemical Co. in < 97% purity. UV-VIS spectra were run with an Aligent model 8453 spectrometer at ambient temperatures. Glutathione was added to a 0.1 M NaH_2PO_4 or 0.1M acetate/acetic acid buffered solution of aquocobalamin stepwise. The final GSCbl UV-VIS spectrum in a titration was identical to solutions made from solid authentic GSCbl kindly supplied by Nicola Brasch. Deiononized–distilled water was used to make up all solutions and all chemicals including those to make up buffers and salt solutions were analytical reagent grade.

4.3.2. Literature studies of the formation of glutathionylcobalamin

The formation of glutathionylcobalamin from aquocobalamin was previously discussed in the Introduction and background section of Chapter 1. The equilibrium constant measured for this reaction in the most detailed study by Brasch and coworkers (34) is given by the following equation:

$$H_2OCbl^+ + GSH_{total} \rightleftharpoons GSCbl + H_3O^+ \quad (1)$$

The equilibrium constant for reaction (1) was called K_{obs}, where GSH_{total} is a total GS- concentration not bonded to cobalamin. The total [GSH_{total}] does not distinguish between the various protonated forms of GSH. There are four basic groups on GSH which are two terminal carboxylates and an amine and a thiolate form. The microscopic ionization

constants for all these forms have been determined by NMR (36). The K_{obs} equilibrium constant lumps all protonated forms of GSH in solution together and lumps all protonations forms of GS on GS-Cbl together. Brasch and coworkers measured the K_{obs} over the range of pH 4.5 – pH 6.0. Because we studied the electrochemistry of GSCbl at pH 4.0, we decided to measure this equilibrium constant at pH 4 and below. At pH 4.50 they found value of $(5.0 \pm 0.4) \times 10^5$ (34).

4.3.3 Experimental titration

A typical spectrophotometric titration is shown in Fig 4.11. 2.00 mL of H2OCbl at concenration 0.0435 mM in sodium dihydrogen phosphate pH 3.30 buffer solution was placed in a 1.00 cm quartz optical cell and 0.050 mL increments of 0.50 mM GSH was added to the cell. The solutions in the optical cell were degassed with prepurified N_2 using a septum for the cell top and a syringe needle in the septum to distribute the gas. The strong γ peak at 350 nm decreases with each increment of GSH added and two peaks from GSCbl at 334 nm and 388 nm grow in on either side of 350 nm peak. Also $\alpha\beta$ region shifts toward the red. GSH does not show an absorption spectrum in the region of interest, 250 nm - 650 nm. There are seven well defined isosbestic points which observed on the figure. At higher pH values these isosbestic points are not that sharply defined.

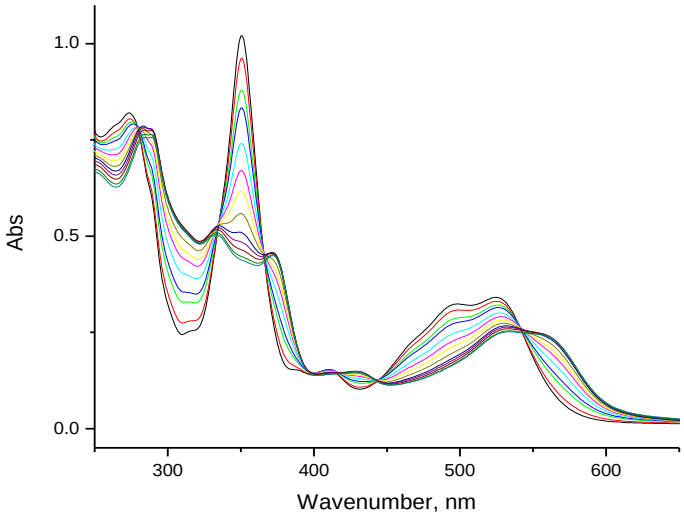

Figure 4.11 UV-Visible spectra of titration of B12a with glutathione, pH 3.30.

4.3.4 K_{obs} Calculation

From the photometric titration curve K_{obs} can be calculated from absorbances at 350 nm. Equation (13) of Appendix VI

$$\frac{A - A_\infty}{A_o - A} = \frac{1}{K_{obs}[X']}$$

can be used to calculate K_{obs}, where A is the absorbance at any point in the titration at 350 nm, A_0 is initial absorbance at 350 nm before any thiol is added, A_∞ is the final constant absorbance at 350nm after endpoint, and $\frac{A - A_\infty}{A_o - A}$ is plotted vs 1/[X'], [X'] is the total free concentration, $[GSH_{total}]$, of GSH in solution and is calculated from the expression

$$[X'] = c_T - \left[c°_M \frac{A_o - A}{A_o - A_\infty} \right]$$

where c_T is total concentration of glutathione added to the solution. Figure 4.12 shows the titration plot at pH 5 in acetate buffer. The repricical of the slope of the plot gives K_{obs} = 2.0 x 10^4 . This is somewhat less than found by Brasch and coworkers, which is probably due to the lack of a good assay of the glutathione concentration.

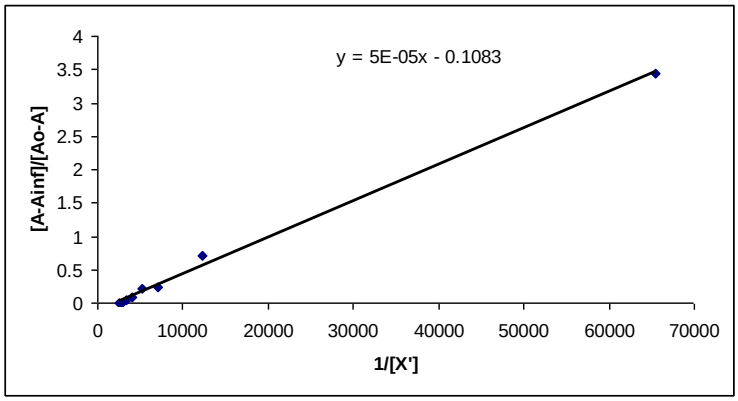

Figure 4.12 Plot to determine K_{obs} by photometric titration, pH 5.0.

Figure 4.13 shows the determination of K_{obs} by photometric titration at lower pH 3.3. In this case we made volume corrections for each point on the curve. The A_∞ was corrected at each point by the factor V_∞/V_i. The y-axis term A' includes the correction $A_\infty V_\infty/V_i$, and the [X'] also contains a volume correction (equiations 15 and 16 of Appendix VI). So reciprocal of the slope plot gives K_{obs} = 9.1 x 10^2. Thus as the pH is lowered, K_{obs} decreases but it is still high enough to form the complex with aquocobalamin.

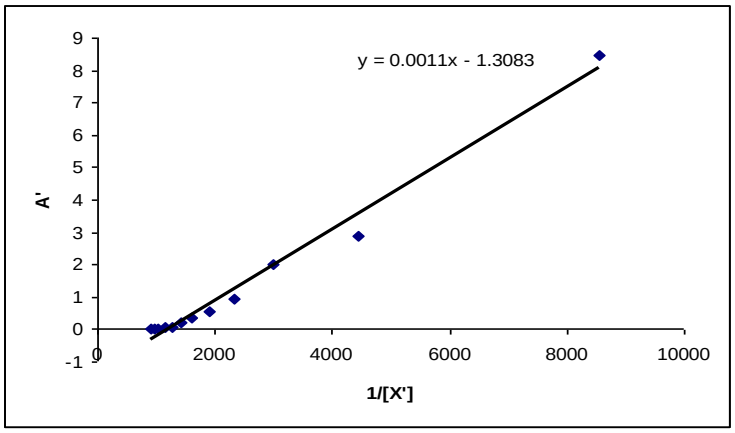

Figure 4.13 Plot to determine K_{obs} by photometric titration, pH 3.3.

4.3. Conclusion

We tentatively conclude that electrochemistry of GSCbl is very similar to that of MeCbl which is 1-electron reduction mechanism. However, the reduction potential of MeCbl is much more negative (-1.6 V) than GSCbl (-0.9 V). Mechanism I is consistent with a homolytic bond breaking after 1-electron addition forming a radical from the β-axial group. This is also consistent with the covalent nature of the Co-S bond in GSCbl which is close to the covalent nature of the Co-C in MeCbl as we have shown by bond order calculation in Chapter 2.

Appendix I MO isosurfaces for GS-Co-corr-Bz^{+} at the BP86/6-311G(d,p) level with cpcm water solvent model

MO	
195	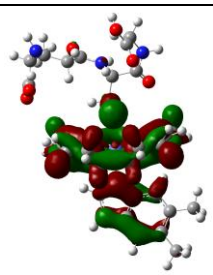
196	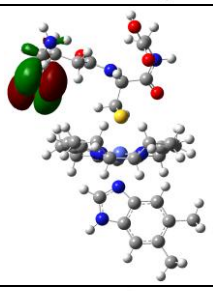
197	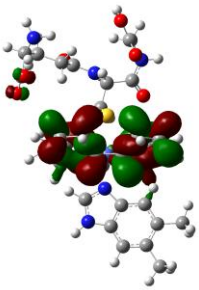
200	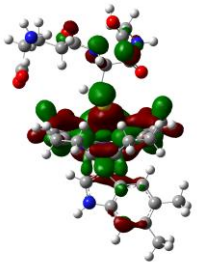
201	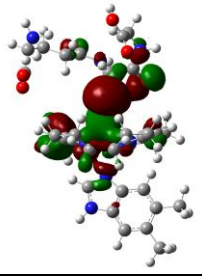

MO	
203	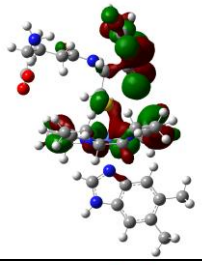
204	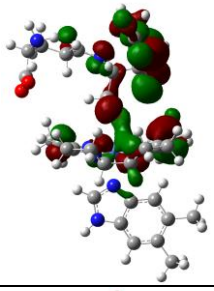
205	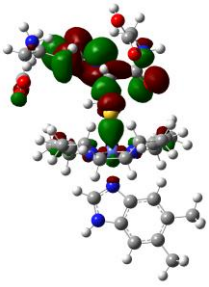
206	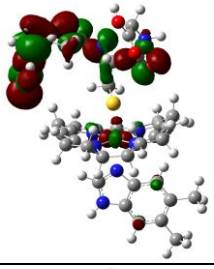
207	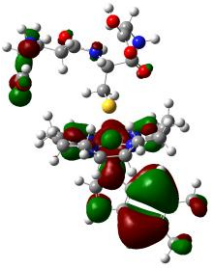

MO	
208	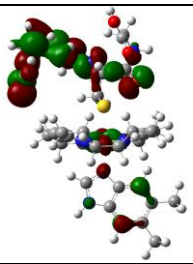
209	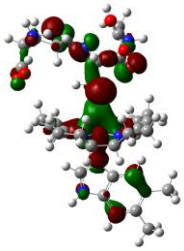
211	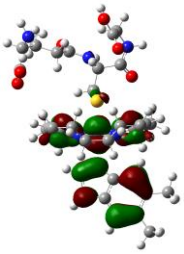
212	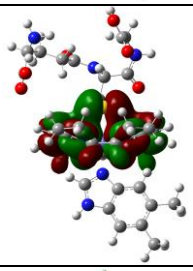
213	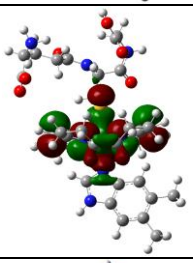
214	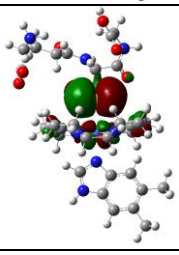

MO	
215	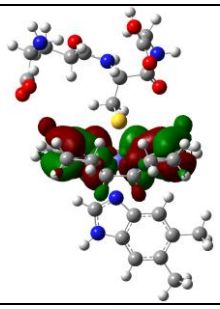
216	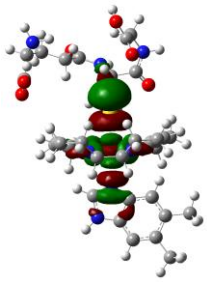
217	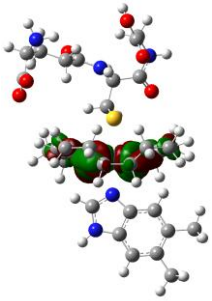
218	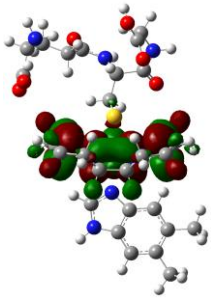
219	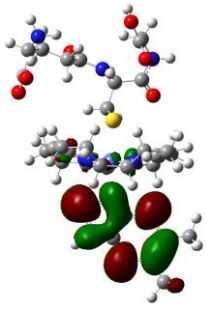

MO	
220	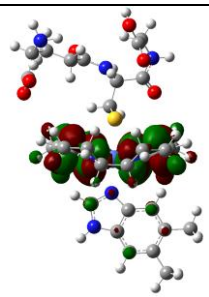
221	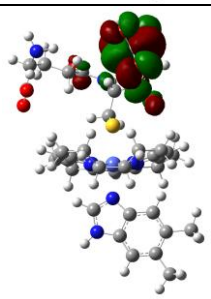
223	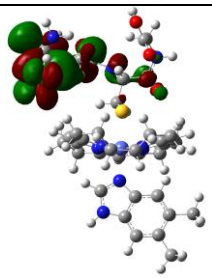
224	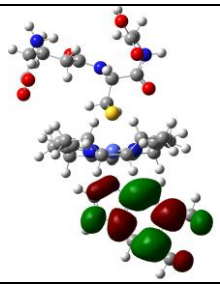

Appendix II

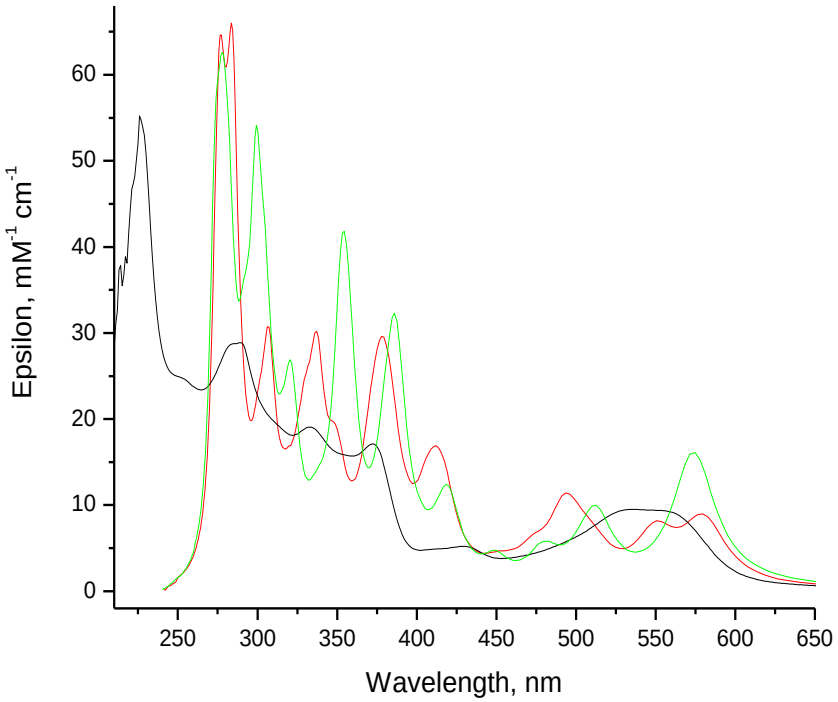

Figure A I. Comparison of absolute electronic absorption (extinction)) vs wavelength (nm) spectra with BP86/6-311G(d,p) (red) and B3LYP/6-311G(d,p) (green) from a GS-Co-corr-Bz aqueous model compared with the experimental spectra (black) at pH 5.00.

Apendix III Natiral Transitions orbital isosurfaces for GS-Co-corr-Bz^{+} at the BP86/6-311G(d,p) level with cpcm water solvent model.

State	Hole	Electron
S1	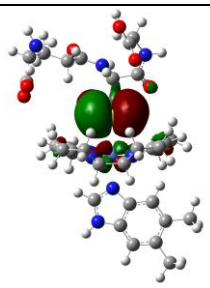	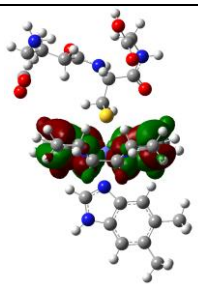
S3	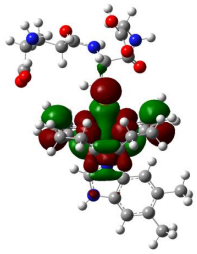	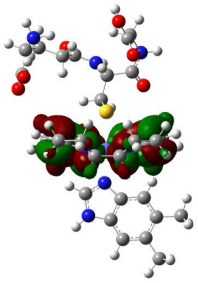
S4	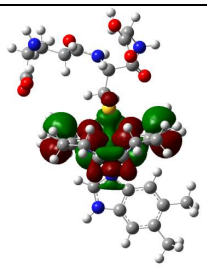	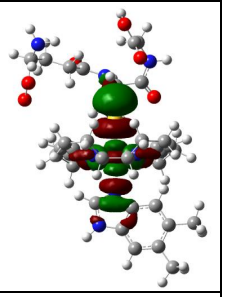
S6	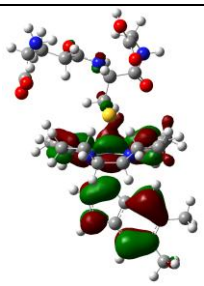	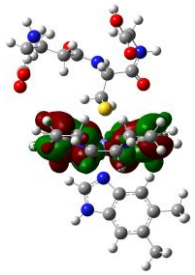
S8	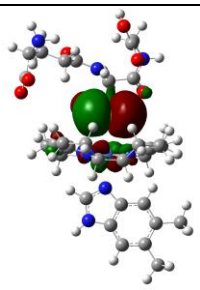	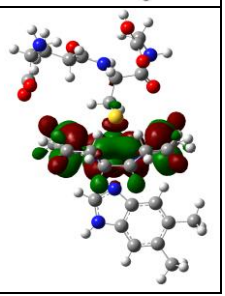

State	Hole	Electron
S9	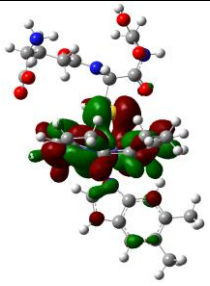	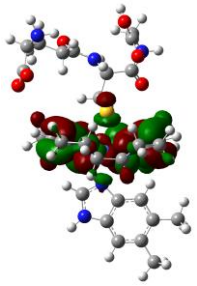
S10	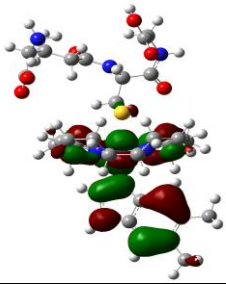	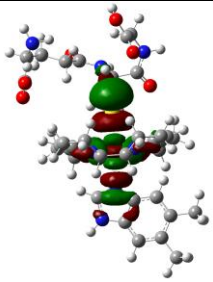
S12	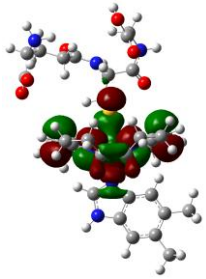	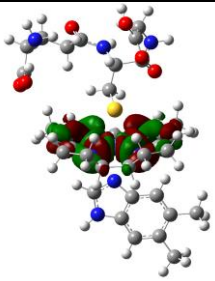
S18	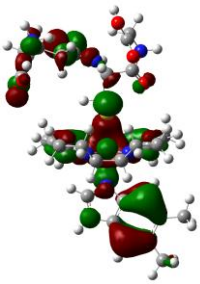	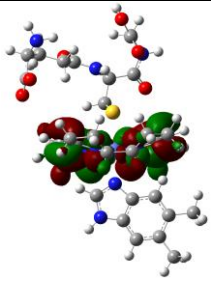
S20	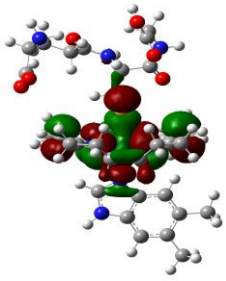	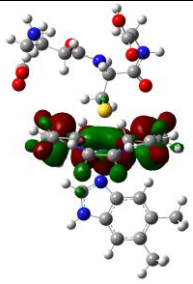

State	Hole	Electron
S21	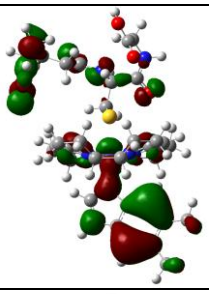	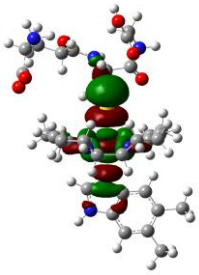
S24	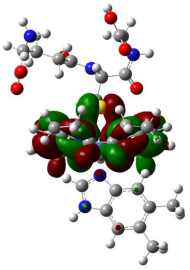	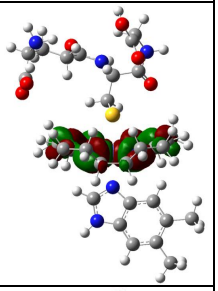
S25	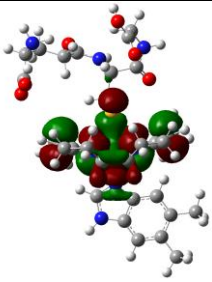	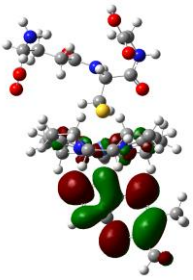
S26	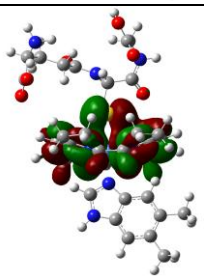	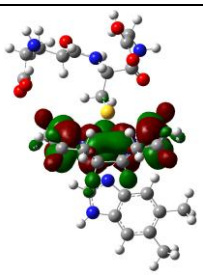
S27	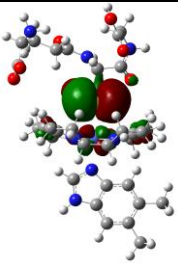	

State	Hole	Electron
S29		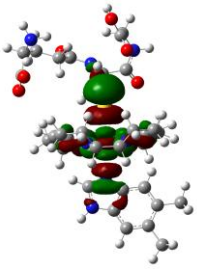
S31	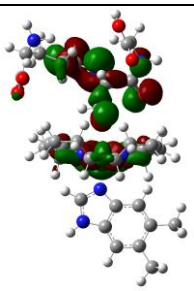	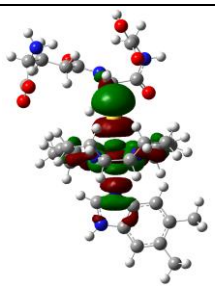
S37	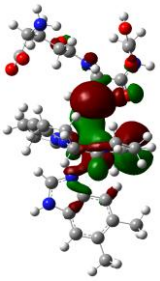	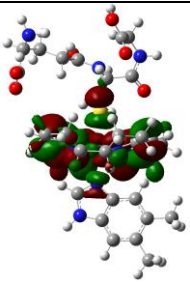
S40	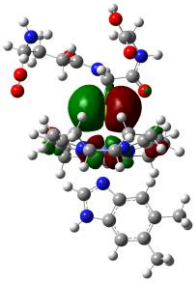	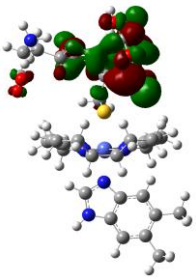
S46	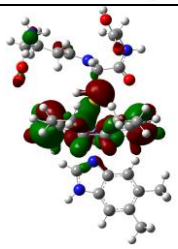	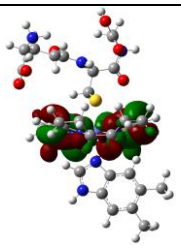

State	Hole	Electron
S52	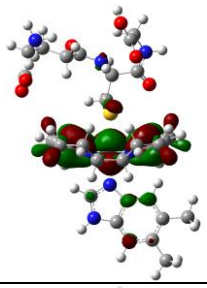	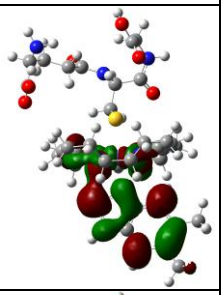
S64	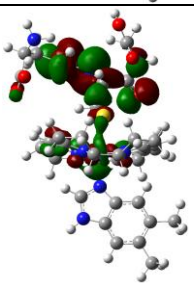	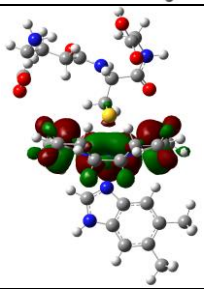
S66	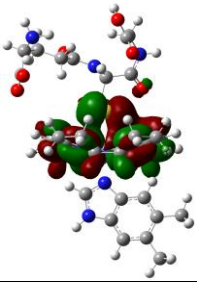	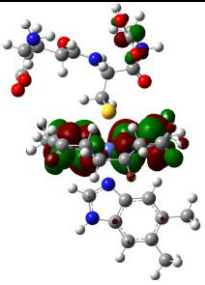
S67	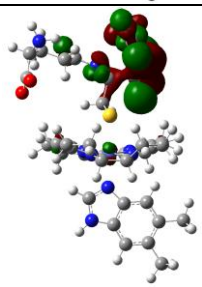	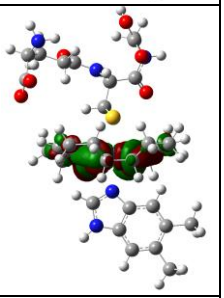
S71	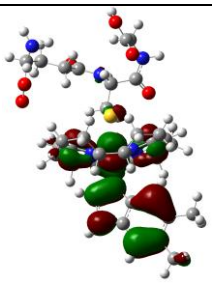	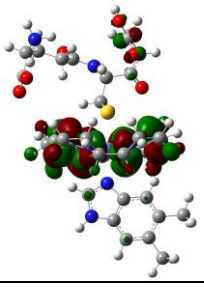

State	Hole	Electron
S85	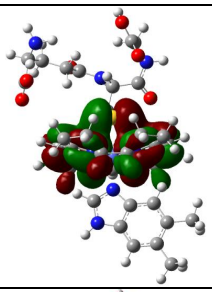	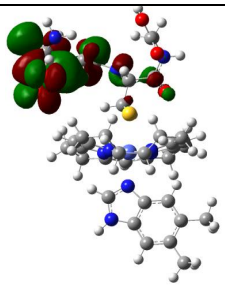
S88	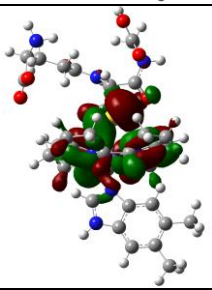	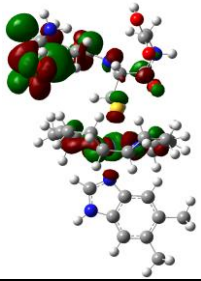
S89	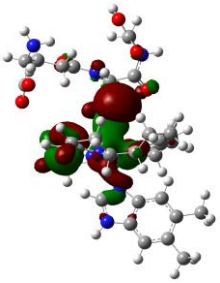	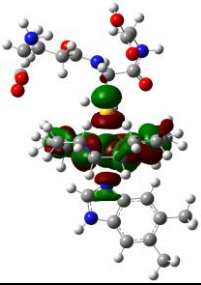
S90	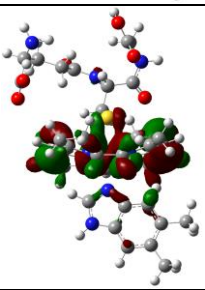	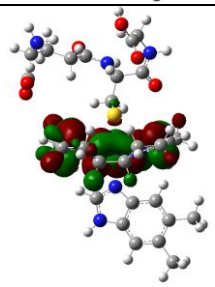
S93	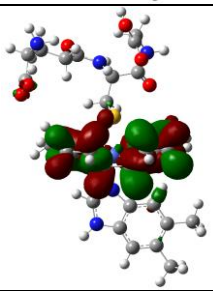	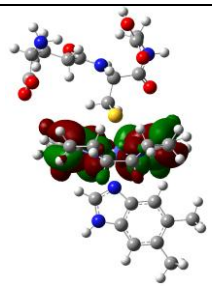

State	Hole	Electron
S96	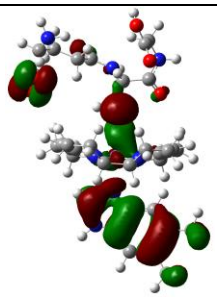	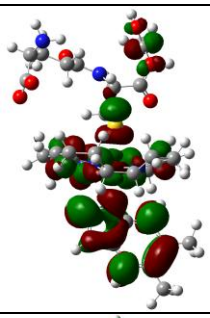
S97	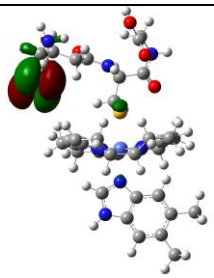	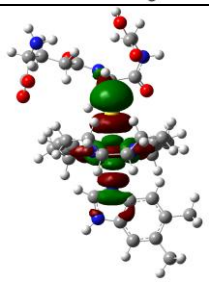
S99	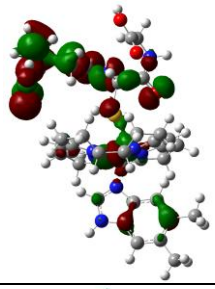	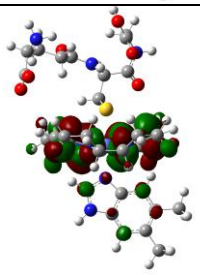
S100	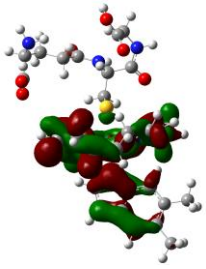	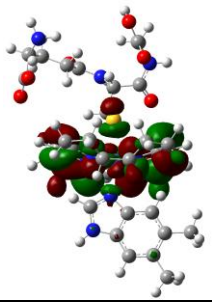

Appendix IV Excitation Calculations Results for GS-Co-corr-Bz^+ at the BP86/6-311G(d,p) level with cpcm water solvent model.

State	Energy	eV			λ (nm)		Oscillator Strength	
OMO #		MO#	OMO	UMO	coefficient	%	OMO description	UMO description
1	1.638	eV			756.9		0.001	
214	->	215	H	L	0.69761	97.33	Spy + σ (dyz +Neq)	dyz+π*corr
3	2.1358	eV			580.5		0.0337	
211	->	215	H-3	L	0.1108	2.46	dxz+ πcorr +πBzm	dyz+π*corr
213	->	215	H-1	L	0.6852	93.90	σ(dxz+Spz)+ πcorr +Nax*	dyz+π*corr
4	2.2562	eV			549.52		0.0257	
212	->	215	H-2	L	0.17809	6.34	π(dyz+Spy)+ πcorr	dyz+π*corr
213	->	216	H-1	L+1	0.65678	86.27	σ(dxz+Spz)+π+Nax*	dz2*+Spz*+Bm Npz
214	->	217	H	L+2	0.13574	3.69	Spy + σ (dyz +Neq)	dx2-y2*+π*corr+p*
6	2.4321	eV			509.79		0.0125	
211	->	215	H-3	L	0.4914	48.29	dxz+πcorr +πBzm	dyz+π*corr
212	->	216	H-2	L+1	-0.18575	6.90	π(dyz+Spy)+πcorr	dz2*+Spz*+P+Bm Npz
214	->	218	H	L+3	0.43976	38.68	Spy + σ (dyz +Neq)	dxz* + π*corr
8	2.4962	eV			496.7		0.0162	
211	->	215	H-3	L	-0.32558	21.20	dxz+πcorr+πBzm	dyz+π*corr
212	->	215	H-2	L	0.22393	10.03	π(dyz+Spy)+πcorr	dyz+π*corr
212	->	216	H-2	L+1	0.12552	3.15	π(dyz+Spy)+πcorr	dz2*+Spz*+P+Bm Npz
213	->	217	H-1	L+2	0.12703	3.23	σ(dxz+Spz)+πcorr+Nax*	dx2-y2*+π*corr+p*
214	->	218	H	L+3	0.52616	55.37	Spy + σ (dyz +Neq)	dxz* + π*corr
9	2.519	eV			492.2		0.025	
211	->	215	H-3	L	0.21599	9.33	dxz+πcorr+πBzm	dyz+π*corr
211	->	216	H-3	L+1	-0.24531	12.04	dxz+πcorr+πBzm	dz2*+Spz*+P+Bm Npz
212	->	215	H-2	L	0.5146	52.96	π(dyz+Spy)+πcorr	dyz + π*corr
213	->	216	H-1	L+1	-0.1458	4.25	σ(dxz+Spz)+πcorr+Nax*	dz2*+Spz*+P+Bm Npz
213	->	218	H-1	L+3	-0.20884	8.72	σ(dxz+Spz)+πcorr+Nax*	dxz* + π*corr
214	->	218	H	L+3	-0.14071	3.96	Spy + σ (dyz +Neq)	dxz* + π*corr
10	2.6228	eV			472.72		0.0128	
211	->	216	H-3	L+1	0.60447	73.08	dxz+πcorr+πBzm	dz2* + Spz* + p* + PBzn

212	->	215	H-2	L	0.23754	11.29	π(dyz+Spy)+πcorr	dyz+π*corr
213	->	218	H-1	L+3	-0.12212	2.98	σ(dxz+Spz)+πcorr+Nax*	dxz* + π*corr
214	->	217	H	L+2	-0.18303	6.70	Spy + σ (dyz +Neq)	dx2-y2*+π*corr+p*
12	2.7643	eV			448.53		0.0052	
207	->	215	H-7	L	-0.16331	5.33	π(dyz+Bm Npx)+π+πBzm	dyz+π*corr
213	->	217	H-1	L+2	0.66373	88.11	σ(dxz+Spz)+πcorr+Nax*	dx2-y2*+π*corr+p*
18	2.9705	eV			417.39		0.0283	
205	->	215	H-9	L	-0.14158	4.01	σ(dxz+Spz)+pglu+πglu	dyz+π*corr
206	->	215	H-8	L	0.40088	32.14	dxy +pglu	dyz+π*corr
207	->	215	H-7	L	0.45995	42.31	π(dyz+Bm Npx)+πcorr+πBzm	dyz+π*corr
209	->	215	H-5	L	-0.14407	4.15	π(dyz+Spy(45°)) + σ(dyz+ Nax(pz))	dyz+π*corr
212	->	218	H-2	L+3	-0.17352	6.02	π(dyz+Spy)+πcorr	dxz* + π*corr
213	->	217	H-1	L+2	0.11545	2.67	σ(dxz+Spz)+πcorr+Bm Npz	dx2-y2*+π*corr+p*
20	3.0084	eV			412.13		0.0266	
207	->	216	H-7	L+1	-0.25443	12.95	π(dyz+Bm Npx)+πcorr+πBzm	dz2*+Spz*+P+Bm Npz
212	->	215	H-2	L	0.1292	3.34	π(dyz+Spy)+πcorr	dyz+π*corr
212	->	217	H-2	L+2	0.39323	30.93	π(dyz+Spy)+πcorr	dx2-y2* + π*corr
213	->	218	H-1	L+3	0.46989	44.16	σ(dxz+Spz)+πcorr+Nax*	dxz* + π*corr
21	3.0531	eV			406.1		0.0167	
206	->	216	H-8	L+1	-0.18997	7.22	dxy +pglu	dz2*+Spz*+P+Bm Npz
207	->	216	H-7	L+1	0.59007	69.64	π(dyz+Bm Npx)+πcorr+πBzm	dz2*+Spz*+P+Bm Npz
208	->	216	H-6	L+1	0.14787	4.37	dxy + π glu + pglu	dz2*+Spz*+P+Bm Npz
209	->	216	H-5	L+1	0.13358	3.57	π(dyz+Spy(45°)) + σ(dyz+ Nax(pz))	dz2*+Spz*+P+Bm Npz
213	->	218	H-1	L+3	0.22255	9.91	σ(dxz+Spz)+πcorr+Bm Npz	dxz* + π*corr
24	3.2196	eV			385.09		0.0307	
203	->	215	H-11	L	-0.20997	8.82	σ(dyz + Spz+Neq) +pglu + πglu + πcorr	dyz+π*corr
204	->	215	H-10	L	0.22962	10.55	σ(dyz+Spx+Neq) +pglu + πglu+π	dyz+π*corr
209	->	216	H-5	L+1	0.11093	2.46	π(dyz+Spy(45°)) + σ(dyz+ Nax(pz))	dz2*+Spz*+P+Bm Npz
211	->	218	H-3	L+3	0.17487	6.12	dxz+π+πBzm	dxz* + π*corr
212	->	217	H-2	L+2	0.46772	43.75	π(dyz+Spy)+πcorr	dx2-y2*+π*corr+p*
213	->	218	H-1	L+3	-0.25609	13.12	σ(dxz+Spz)+π+Bm Npz	dxz* + π*corr
213	->	219	H-1	L+4	-0.11131	2.48	σ(dxz+Spz)+πcorr+Nax*	πBzm
25	3.2414	eV			382.5		0.0139	

212	->	218	H-2	L+3	-0.36075	26.03	π(dyz+Spy)+πcorr	dxz* + π*corr
213	->	219	H-1	L+4	0.56402	63.62	σ(dxz+Spz)+πcorr+Nax*	πBzm
26	3.2639	eV			379.86		0.0335	
205	->	215	H-9	L	0.13092	3.43	σ(dxz+Spz)+pglu+πglu	dyz+π*corr
207	->	215	H-7	L	0.10729	2.30	π(dyz+Bm Npx)+πcorr+πBzm	dyz+π*corr
211	->	217	H-3	L+2	-0.1153	2.66	dxz+πcorr+πBzm	dx2-y2*+π*corr+p*
212	->	218	H-2	L+3	0.47047	44.27	π(dyz+Spy)+πcorr	dxz* + π*corr
213	->	219	H-1	L+4	0.40433	32.70	σ(dxz+Spz)+πcorr+Nax*	πBzm
213	->	220	H-1	L+5	-0.15954	5.09	σ(dxz+Spz)+πcorr+Nax*	π(dx2-y2+Neq)+p
27	3.2756	eV			378.5		0.0154	
205	->	216	H-9	L+1	0.2925	17.11	σ(dxz+Spz)+pglu+πglu	dz2*+Spz*+P+Bm Npz
211	->	218	H-3	L+3	0.12069	2.91	dxz+π+πBzm	dxz* + π*corr
214	->	220	H	L+5	0.60668	73.61	Spy + σ (dyz +Neq)	π(dx2-y2+Neq)+p
29	3.301	eV			375.59		0.0338	
204	->	216	H-10	L+1	-0.10687	2.28	σ(dyz+Spx+Neq) +pglu + πglu+π	dz2*+Spz*+P+Bm Npz
205	->	216	H-9	L+1	0.4478	40.10	σ(dxz+Spz)+pglu+πglu	dz2*+Spz*+P+Bm Npz
209	->	216	H-5	L+1	0.15907	5.06	π(dyz+Spy(45^{o})) + σ(dyz+Nax(pz))	dz2*+Spz*+P+Bm Npz
211	->	217	H-3	L+2	-0.20485	8.39	dxz+πcorr+πBzm	dx2-y2*+π*corr+p*
211	->	218	H-3	L+3	0.2597	13.49	dxz+πcorr+πBzm	dxz* + π*corr
214	->	220	H	L+5	-0.31887	20.34	Spy + σ (dyz +Neq)	π(dx2-y2+Neq)+p
31	3.3527	eV			369.81		0.0316	
201	->	216	H-13	L+1	-0.13127	3.45	σ(dxz+Spz+Neq) +πcorr+ πglu +pglu + π(Bm Npz+dyz)	dz2*+Spz*+P+Bm Npz
205	->	216	H-9	L+1	0.38782	30.08	σ(dxz+Spz)+pglu+πglu	dz2*+Spz*+P+Bm Npz
206	->	216	H-8	L+1	0.10568	2.23	dxy +pglu	dz2*+Spz*+P+Bm Npz
207	->	216	H-7	L+1	0.13642	3.72	π(dyz+Bm Npx)+πcorr+πBzm	dz2*+Spz*+P+Bm Npz
208	->	216	H-6	L+1	-0.11841	2.80	dxy + π glu + pglu	dz2*+Spz*+P+Bm Npz
209	->	216	H-5	L+1	-0.21174	8.97	π(dyz+Spy(45^{o})) + σ(dyz+Nax(pz))	dz2*+Spz*+P+Bm Npz
211	->	217	H-3	L+2	0.1136	2.58	dxz+πcorr+πBzm	dx2-y2*+π*corr+p*
211	->	218	H-3	L+3	-0.33739	22.77	dxz+πcorr+πBzm	dxz* + π*corr
212	->	215	H-2	L	-0.11805	2.79	π(dyz+Spy)+πcorr	dyz + π*corr
212	->	217	H-2	L+2	0.18977	7.20	π(dyz+Spy)+πcorr	dx2-y2*+π*corr+p*
213	->	218	H-13	L+3	-0.126	3.18	σ(dxz+Spz)+πcorr+Nax*	dxz* + π*corr
37	3.5367	eV			350.56		0.021	
201	->	215	H-13	L	0.40199	32.3	σ(dxz+Spz+Neq) +πcorr+ πglu +pglu + π(Bm	dyz+π*corr

						2	Npz+dyz)	
203	->	215	H-11	L	-0.17326	6.00	σ(dyz + Spz+Neq) +pglu + πglu + πcorr	dyz+π*corr
203	->	216	H-11	L+1	0.28437	16.17	σ(dyz + Spz+Neq) +pglu + πglu + πcorr	dz2*+Spz*+P+Bm Npz
204	->	215	H-10	L	0.16389	5.37	σ(dyz+Spx+Neq) +pglu + πglu+π	dyz + π*corr
204	->	216	H-10	L+1	-0.23849	11.38	σ(dyz+Spx+Neq) +pglu + πglu+π	dz2*+Spz*+P+Bm Npz
207	->	217	H-7	L+2	-0.15343	4.71	π(dyz+Bm Npx)+π+πBzm	dx2-y2*+π*corr+p*
208	->	217	H-6	L+2	-0.11107	2.47	dxy + π glu + pglu	dx2-y2*+π*corr+p*
209	->	217	H-5	L+2	-0.21506	9.25	π(dyz+Spy(45^{o})) + σ(dyz+Nax(pz))	dx2-y2*+π*corr+p*
211	->	217	H-3	L+2	0.11316	2.56	dxz+π+πBzm	dx2-y2*+π*corr+p*
40	3.5632	eV			347.96		0.0111	
214	->	222	H	L+7	0.69168	95.68	σ (dyz +Neq) +Spy	p glu + π glu
46	3.6739	eV			337.47		0.071	
201	->	215	H-13	L	0.2242	10.05	σ(dxz+Spz+Neq) +π+ πglu +pglu + π(Bm Npz+dyz)	dyz+π*corr
203	->	215	H-11	L	0.28355	16.08	σ(dyz + Spz+Neq) +pglu + πglu + πcorr	dyz+π*corr
204	->	215	H-10	L	-0.24915	12.42	σ(dyz+Spx+Neq) +pglu + πglu+π	dyz+π*corr
206	->	217	H-8	L+2	-0.29862	17.83	dxy +pglu	dx2-y2*+π*corr+p*
208	->	216	H-6	L+1	0.11574	2.68	dxy + π glu + pglu	dz2*+Spz*+P+Bm Npz
208	->	218	H-6	L+3	0.1692	5.73	dxy + π glu + pglu	dxz* + π*corr
209	->	216	H-5	L+1	0.24222	11.73	π(dyz+Spy(45^{o})) + σ(dyz+Nax(pz))	dz2* + Spz* + p* + PBzn
209	->	218	H-5	L+3	-0.11161	2.49	π(dyz+Spy(45^{o})) + σ(dyz+Nax(pz))	dxz* + π*corr
212	->	217	H-2	L+2	0.10197	2.08	π(dyz+Spy)+πcorr	dx2-y2*+π*corr+p*
213	->	218	H-1	L+3	-0.13758	3.79	σ(dxz+Spz)+π+Nax*	dxz* + π*corr
52	3.7623	eV			329.54		0.0255	
200	->	215	H-14	L	-0.16239	5.27	σ(dxz+Spz+BzNpz)+π(dxy+cor N)	dyz+π*corr
203	->	216	H-11	L+1	0.12141	2.95	σ(dyz + Spz+Neq) +pglu + πglu + πcorr	dz2*+Spz*+P+Bm Npz
204	->	216	H-10	L+1	-0.11042	2.44	σ(dyz+Spx+Neq) +pglu + πglu+πcorr	dz2*+Spz*+P+Bm Npz
207	->	217	H-7	L+2	0.31519	19.87	π(dyz+Bm Npx)+πcorr+πBzm	dx2-y2*+π*corr+p*
207	->	218	H-7	L+3	0.16467	5.42	π(dyz+Bm Npx)+πcorr+πBzm	dxz* + π*corr
207	->	219	H-7	L+4	0.10687	2.28	π(dyz+Bm Npx)+πcorr+πBzm	πBzm
208	->	217	H-6	L+2	0.10532	2.22	dxy + π glu + pglu	dx2-y2*+π*corr+p*
209	->	217	H-5	L+2	0.13123	3.44	π(dyz+Spy(45^{o})) + σ(dyz+Nax(pz))	dx2-y2*+π*corr+p*
211	->	217	H-3	L+2	0.16006	5.12	dxz+πcorr+πBzm	dx2-y2*+π*corr+p*
211	->	219	H-3	L+4	0.45183	40.83	dxz+πcorr+πBzm	πBzm
213	->	220	H-1	L+5	-0.11833	2.80	σ(dxz+Spz)+πcorr+Nax*	π(dx2-y2+Neq)+p
64	4.0155	eV			308.76		0.0206	
205	->	218	H-9	L+3	0.58118	67.5	σ(dxz+Spz)+pglu+πglu	dxz* + π*corr

						5		
212	->	220	H-2	L+5	-0.16846	5.68	π(dyz+Spy)+πcorr	π(dx2-y2+Neq)+p
212	->	221	H-2	L+6	0.28227	15.94	π(dyz+Spy)+πcorr	p glu + π glu
66	4.0418	eV			306.75		0.0256	
197	->	215	H-17	L	-0.16408	5.38	π+π(dyz+corr N)	dyz+π*corr
200	->	215	H-14	L	0.10857	2.36	σ(dxz+Spz+BzNpz)+π(dxy+corr N)	dyz+π*corr
203	->	217	H-11	L+2	-0.12489	3.12	σ(dyz + Spz+Neq) +pglu + πglu + πcorr	dx2-y2*+π*corr+p*
204	->	217	H-10	L+2	-0.30265	18.32	σ(dyz+Spx+Neq) +pglu + πglu+π	dx2-y2*+π*corr+p*
205	->	218	H-9	L+3	0.18288	6.69	σ(dxz+Spz)+pglu+πglu	dxz* + π*corr
207	->	218	H-7	L+3	0.12408	3.08	π(dyz+Bm Npx)+π+πBzm	dxz* + π*corr
212	->	220	H-2	L+5	0.45874	42.09	π(dyz+Spy)+πcorr	π(dx2-y2+Neq)+p
213	->	223	H-1	L+8	0.19709	7.77	σ(dxz+Spz)+πcorr+Nax*	p glu + π glu
67	4.0442	eV			306.58		0.0164	
200	->	215	H-14	L	0.2677	14.33	σ(dxz+Spz+BzNpz)+π(dxy+cor N)	dyz+π*corr
203	->	217	H-11	L+2	0.34446	23.73	σ(dyz + Spz+Neq) +pglu + πglu + πcorr	dx2-y2*+π*corr+p*
203	->	218	H-11	L+3	-0.14833	4.40	σ(dyz + Spz+Neq) +pglu + πglu + πcorr	dxz* + π*corr
204	->	217	H-10	L+2	0.36581	26.76	σ(dyz+Spx+Neq) +pglu + πglu+πcorr	dx2-y2*+π*corr+p*
204	->	218	H-10	L+3	0.1461	4.27	σ(dyz+Spx+Neq) +pglu + πglu+πcorr	dxz* + π*corr
213	->	220	H-1	L+5	-0.14589	4.26	σ(dxz+Spz)+πcorr+Nax*	π(dx2-y2+Neq)+p
213	->	223	H-1	L+8	0.25033	12.53	σ(dxz+Spz)+πcorr+Nax*	p glu + π glu
71	4.1205	eV			300.89		0.0326	
211	->	220	H-3	L+5	0.64903	84.25	dxz+πcorr+πBzm	π(dx2-y2+Neq)+p
						0.00		
85	4.3481	eV			285.15		0.0842	
200	->	216	H-14	L+1	0.13528	3.66	σ(dxz+Spz+BzNpz)+π(dxy+corr N)	dz2*+Spz*+P+Bm Npz
201	->	216	H-13	L+1	-0.17132	5.87	σ(dxz+Spz+Neq) +π+ πglu +pglu + π(Bm Npz+dyz)	dz2*+Spz*+P+Bm Npz
201	->	218	H-13	L+3	0.19201	7.37	σ(dxz+Spz+Neq) +πcorr+ πglu +pglu + π(Bm Npz+dyz)	dxz* + π*corr
210	->	219	H-4	L+4	0.12965	3.36	πBzm	πBzm
210	->	220	H-4	L+5	0.17184	5.91	πBzm	π(dx2-y2+Neq)+p
212	->	223	H-2	L+8	0.55552	61.72	π(dyz+Spy)+πcorr	p glu + π glu
88	4.3554	eV			284.67		0.0505	
196	->	215	H-18	L	0.25918	13.43	pglu(not sulfur)	dyz+π*corr
200	->	216	H-14	L+1	-0.1392	3.88	σ(dxz+Spz+BzNpz)+π(dxy+corr N)	dz2*+Spz*+P+Bm Npz
201	->	216	H-13	L+1	0.12835	3.29	dxz(+45°) + σSpz +π+ πglu +pglu + πNpzBzm	dz2*+Spz*+P+Bm Npz
201	->	217	H-13	L+2	-0.20412	8.33	dxz(+45°) + σSpz +π+ πglu +pglu + πNpzBzm	dx2-y2*+π*corr+p*

201	->	218	H-13	L+3	-0.2397	11.49	dxz(+45°) + σSpz +π+ πglu +pglu + πNpzBzm	dxz* + π*corr
203	->	217	H-11	L+2	-0.16047	5.15	σ(dyz + Spz+Neq) +pglu + πglu + π	dx2-y2*+π*corr+p*
204	->	217	H-10	L+2	0.13665	3.73	σ(dyz+Spx+Neq) +pglu + πglu+π	dx2-y2*+π*corr+p*
210	->	220	H-4	L+5	-0.12794	3.27	πBzm	π(dx2-y2+Neq)+p
212	->	223	H-2	L+8	0.38562	29.74	π(dyz+Spy)+πcorr	p glu + π glu
89	4.3722	eV			283.57		0.0648	
195	->	216	H-19	L+1	0.11546	2.67	π + πBzm	dz2*+Spz*+P+Bm Npz
196	->	215	H-18	L	-0.17066	5.82	pglu(not sulfur)	dyz+π*corr
197	->	215	H-17	L	0.307	18.85	π+π(dyz+corr N)	dyz + π*corr
200	->	218	H-14	L+3	0.11676	2.73	σ(dxz+Spz+BzNpz)+π(dxy+cor N)	dxz* + π*corr
201	->	216	H-13	L+1	0.22926	10.51	σ(dxz+Spz+Neq) +π+ πglu +pglu + π(Bm Npz+dyz)	dz2*+Spz*+P+Bm Npz
201	->	217	H-13	L+2	0.25396	12.90	σ(dxz+Spz+Neq) +π+ πglu +pglu + π(Bm Npz+dyz)	dx2-y2*+π*corr+p*
201	->	218	H-13	L+3	-0.15306	4.69	σ(dxz+Spz+Neq) +πcorr + πglu+pglu+π(Bm Npz+dyz)	dxz* + π*corr
203	->	217	H-11	L+2	0.21588	9.32	σ(dyz + Spz+Neq) +pglu + πglu + π	dx2-y2*+π*corr+p*
204	->	217	H-10	L+2	-0.18528	6.87	σ(dyz+Spx+Neq) +pglu + πglu+π	dx2-y2*+π*corr+p*
212	->	223	H-2	L+8	0.15634	4.89	π(dyz+Spy)+πcorr	p glu + π glu
90	4.4213	eV			280.43		0.0426	
195	->	215	H-19	L	-0.16811	5.65	πcorr + πBzm	dyz+π*corr
200	->	215	H-14	L	0.1389	3.86	σ(dxz+Spz+BzNpz)+π(dxy+cor N)	dyz+π*corr
201	->	216	H-13	L+1	-0.13175	3.47	σ(dxz+Spz+Neq) +πcorr+ πglu +pglu + π(Bm Npz+dyz)	dz2*+Spz*+P+Bm Npz
203	->	218	H-11	L+3	0.30283	18.34	σ(dyz + Spz+Neq) +pglu + πglu + πcorr	dxz* + π*corr
204	->	218	H-10	L+3	-0.27091	14.68	σ(dyz+Spx+Neq) +pglu + πglu+πcorr	dxz* + π*corr
205	->	219	H-9	L+4	-0.2077	8.63	σ(dxz+Spz)+pglu+πglu	πBzm
208	->	220	H-6	L+5	0.16123	5.20	dxy + π glu + pglu	π(dx2-y2+Neq)+p
209	->	220	H-5	L+5	0.27035	14.62	π(dyz+Spy(45^{o})) + σ(dyz+Nax(pz))	π(dx2-y2+Neq)+p
213	->	220	H-1	L+5	-0.11732	2.75	σ(dxz+Spz)+πcorr+Nax*	π(dx2-y2+Neq)+p
93	4.46	eV			277.99		0.0341	
197	->	215	H-17	L	0.47694	45.49	πcorr	dyz+π*corr
201	->	217	H-13	L+2	-0.14507	4.21	σ(dxz+Spz+Neq) +πcorr+ πglu +pglu + π(Bm Npz+dyz)	dx2-y2* + π*corr
201	->	218	H-13	L+3	0.23806	11.33	σ(dxz+Spz+Neq) +πcorr+ πglu +pglu + π(Bm Npz+dyz)	dxz* + π*corr
203	->	217	H-11	L+2	-0.2133	9.10	σ(dyz + Spz+Neq) +pglu + πglu + πcorr	dx2-y2*+π*corr+p*
204	->	217	H-10	L+2	0.18645	6.95	σ(dyz+Spx+Neq) +pglu + πglu+πcorr	dx2-y2*+π*corr+p*
212	->	220	H-2	L+5	0.15142	4.59	π(dyz+Spy)+πcorr	π(dx2-y2+Neq)+p
96	4.4888	eV			276.21		0.105	
196	->	216	H-18	L+1	-0.33124	21.94	pglu(not sulfur)	dz2*+Spz*+P+Bm Npz

197	->	215	H-17	L	0.10842	2.35	π+π(dyz+corr N)	dyz+π*corr
201	->	216	H-13	L+1	-0.10352	2.14	σ(dxz+Spz+Neq) +πcorr+ πglu +pglu + π(Bm Npz+dyz)	dz2*+Spz*+P+Bm Npz
201	->	218	H-13	L+3	-0.2163	9.36	σ(dxz+Spz+Neq) +πcorr+ πglu +pglu + π(Bm Npz+dyz)	dxz* + π*corr
207	->	219	H-7	L+4	-0.12585	3.17	π(dyz+Bm Npx)+πcorr+πBzm	πBzm
209	->	220	H-5	L+5	-0.22168	9.83	π(dyz+Spy(45^o)) + σ(dyz+Nax(pz))	π(dx2-y2+Neq)+p
210	->	219	H-4	L+4	0.28822	16.61	πBzm	
210	->	220	H-4	L+5	-0.19359	7.50	πBzm	π(dx2-y2+Neq)+p
210	->	221	H-4	L+6	0.10465	2.19	πBzm	p glu + π glu
211	->	223	H-3	L+8	-0.19278	7.43	dxz+π+πBzm	p glu + π glu
211	->	224	H-3	L+9	0.16106	5.19	dxz+π+πBzm	πBzm* + pBzm*
97	4.4897	eV			276.15		0.0302	
196	->	216	H-18	L+1	0.62255	77.51	pglu(not sulfur)	dz2*+Spz*+P+Bm Npz
201	->	218	H-13	L+3	-0.12653	3.20	σ(dxz+Spz+Neq) +πcorr+ πglu +pglu + π(Bm Npz+dyz)	dxz* + π*corr
209	->	220	H-5	L+5	-0.127	3.23	π(dyz+Spy(45^o)) + σ(dyz+Nax(pz))	π(dx2-y2+Neq)+p
210	->	219	H-4	L+4	0.15717	4.94	πBzm	πBzm
210	->	220	H-4	L+5	-0.10524	2.22	πBzm	dx2-y2* + π*corr
						0.00		
99	4.5273	eV			273.86		0.0208	
195	->	215	H-19	L	0.36933	27.28	πcorr + πBzm	dyz+π*corr
201	->	216	H-13	L+1	0.10634	2.26	σ(dxz+Spz+Neq) +πcorr+ πglu +pglu + π(Bm Npz+dyz)	dz2*+Spz*+P+Bm Npz
201	->	218	H-13	L+3	0.15244	4.65	σ(dxz+Spz+Neq) +πcorr+ πglu +pglu + π(Bm Npz+dyz)	dxz* + π*corr
208	->	220	H-6	L+5	0.44218	39.10	dxy + π glu + pglu	π(dx2-y2+Neq)+p
210	->	219	H-4	L+4	0.1441	4.15	πBzm	πBzm
211	->	224	H-3	L+9	0.12413	3.08	dxz+π+πBzm	πBzm* + pBzm*
212	->	224	H-2	L+9	-0.16392	5.37	π(dyz+Spy)+πcorr	πBzm* + pBzm*
100	4.5313	eV			273.62		0.0408	
195	->	215	H-19	L	0.39137	30.63	πcorr + πBzm	dyz+π*corr
200	->	216	H-14	L+1	0.10044	2.02	σ(dxz+Spz+BzNpz)+π(dxy+cor N)	dz2*+Spz*+P+Bm Npz
200	->	217	H-14	L+2	0.13334	3.56	σ(dxz+Spz+BzNpz)+π(dxy+cor N)	dx2-y2*+π*corr+p*
201	->	216	H-13	L+1	-0.14607	4.27	σ(dxz+Spz+Neq) +πcorr+ πglu +pglu + π(Bm Npz+dyz)	dz2*+Spz*+P+Bm Npz
201	->	218	H-13	L+3	-0.19936	7.95	σ(dxz+Spz+Neq) +πcorr+ πglu +pglu + π(Bm Npz+dyz)	dxz* + π*corr
210	->	219	H-4	L+4	-0.17839	6.36	πBzm	πBzm
210	->	220	H-4	L+5	0.12785	3.27	πBzm	π(dx2-y2+Neq)+p
211	->	224	H-3	L+9	-0.14689	4.32	dxz+πcorr+πBzm	πBzm* + pBzm*
..	->	224	H-2	L+9	0.31108	19.35	π(dyz+Spy)+πcorr	πBzm* + pBzm*

Appendix V

Mechanism 1

```
* Icap Calc = n    * IR corr = n
* Initial Potential =  0.5000
* Switching Potential = -1.2000
* Final potential   =  0.5000
* Scan Rate =   0.0500
* Concentrations - normalized units
  1:   0.000    2:   0.000    3:   0.000    4:   0.987    5:   0.000    6:   0.000
* Diffusion Coefficients *  3.00000000000000E-0006
  1:   1.000    2:   1.000    3:   1.000    4:   1.000    5:   1.000    6:   1.000
* Electrode Reactions
  1 + e- <=> 2  E =   -0.050  khet=    0.0050000  Al =    0.5000
  2 + e- <=> 3  E =   -0.870  khet=    0.0010000  Al =    0.5000
  4 + e- <=> 5  E =   -0.890  khet=    0.0050000  Al =    0.6500
* Chemical Reactions
  5 + 0 = 3 + 6
* K-foward =    100.000    * K-Reverse =      1.000
* Area, Normal Conc, Cap and IR
    1.0E-0001     9.9E-0007
* Temperature = 298.150
* Number of time increments = 13600
* Number of space increments = 31
```

Mechanism 2

```
* Final potential   =  0.5000
* Scan Rate =   0.0500
* Concentrations - normalized units
  1:   0.000    2:   0.000    3:   0.000    4:   0.987    5:   0.000    6:   0.000    7:   0.000
* Diffusion Coefficients *  3.00000000000000E-0006
  1:   1.000    2:   1.000    3:   1.000    4:   1.000    5:   1.000    6:   1.000    7:   1.000
* Electrode Reactions
  1 + e- <=> 2  E =   -0.050  khet=    0.0050000  Al =    0.5000
  2 + e- <=> 3  E =   -0.870  khet=    0.0100000  Al =    0.5000
  4 + e- <=> 5  E =   -0.940  khet=    0.0050000  Al =    0.6500
  5 + e- <=> 6  E =   -0.940  khet=    0.0000800  Al =    0.5000
* Chemical Reactions
  6 + 0 = 3 + 7
* K-foward =    100.000    * K-Reverse =      1.000
* Area, Normal Conc, Cap and IR
    1.0E-0001     9.9E-0007
* Temperature = 298.150
* Number of time increments = 13600
* Number of space increments = 31
```

Simulation parameters for Figure 4.10

```
 * Icap Calc = n    * IR corr = n
 * Initial Potential = -0.6000
 * Switching Potential = -1.1500
 * Final potential   = -0.6000
 * Scan Rate =   0.0500
 * Concentrations - normalized units
   1:  0.000    2:  0.000    3:  0.000    4:  0.435    5:  0.000    6:  0.000    7:  0.000
 * Diffusion Coefficients *  3.00000000000000E-0006
   1:  1.000    2:  1.000    3:  1.000    4:  1.000    5:  1.000    6:  1.000    7:  1.000
 * Electrode Reactions
   1 + e- <=> 2  E =   -0.050  khet=    0.0050000  Al =    0.5000
   2 + e- <=> 3  E =   -0.890  khet=    0.0010000  Al =    0.5000
   4 + e- <=> 5  E =   -0.890  khet=    0.0050000  Al =    0.6500
   6 + e- <=> 7  E =   -0.100  khet=    0.0050000  Al =    0.6500
 * Chemical Reactions
   5 + 0 = 3 + 6
 * K-foward =    100.000    * K-Reverse =      0.000
 * Area, Normal Conc, Cap and IR
    1.0E-0001     4.4E-0007
 * Temperature = 298.150
 * Number of time increments = 4400
 * Number of space increments = 28
```

Appendix VI **Equilibrium constant derivation:**

$$K_{obs} = \frac{[Cbl - SG']}{[GSH'][Cbl(III)]} = \frac{[MX']}{[X'][M]}$$

Where [MX'] is sum of all forms of thiol complex
And [X'] is sum of all forms of uncomplexed glutathione
[M] is [Cbl(III)] aquocobalamin at λ=350nm

$A = \varepsilon_{MX'}[MX'] + \varepsilon_M[M]$ (1)
$c°_M$ is initial concentration of $[Cbl(III)]$
A is the absorbance at any point in the titration at 350 nm
A_0 is initial absorbance at 350 nm before any thiol is added.
A_∞ is final constant absorbance at 350nm after endpoint.

$c°_M = [MX'] + [M]$ (2)

$$\varepsilon_M = \frac{A_o}{c°_M} \quad (3)$$

$$\varepsilon_{MX'} = \frac{A_\infty}{c°_M} \quad (4)$$

Equation (3) and (4) into (1)

$$A = \frac{A_\infty}{c°_M}[MX'] + \frac{A_o}{c°_M}[M] \quad (5)$$

From (2) into (5) $[MX'] = c°_M - [M]$ (6)

(6) into (5)

$$A = \frac{A_\infty}{c°_M}(c°_M - [M]) + \frac{A_o}{c°_M}[M] \quad (7)$$

$$A = A_\infty - \frac{A_\infty}{c°_M}[M] + \frac{A_o}{c°_M}[M]$$

$$A = A_\infty + \frac{A_o - A_\infty}{c°_M}[M] \quad (8)$$

$$[M] = \frac{A - A_\infty}{A_o - A_\infty} c°_M \qquad (9)$$

$$K' = \frac{[MX']}{[X'][M']} \qquad (10)$$

Rearrange (10)

$$\frac{[M']}{[MX']} = \frac{1}{K'[X']} \qquad (11)$$

Now find [MX] in terms of [M]
i.e.
$[MX] = c°_M - [M]$ (2)

or using (9)

$$[MX'] = c°_M - c°_M \frac{A - A_\infty}{A_o - A_\infty}$$

$$[MX'] = c°_M \left[1 - \frac{A - A_\infty}{A_o - A_\infty} \right] = c°_M \frac{A_o - A}{A_o - A_\infty} \qquad (12)$$

So from equations (9), (11) + (12)

$$\left[c°_M \frac{A - A_\infty}{A_o - A_\infty} \right] \frac{A_o - A_\infty}{A_o - A} \frac{1}{c°_M} = \frac{1}{K_{obs}[X']}$$

Canceling gives

$$\frac{A - A_\infty}{A_o - A} = \frac{1}{K_{obs}[X']} \qquad (13)$$

Note [X'] is calculated from total GSH add (c_T) minus [MX'] or
c_T is total concentration of glutathione added to solution

$$[X'] = c_T - \left[c°_M \frac{A_o - A}{A_o - A_\infty} \right] \qquad (14)$$

When volume correction must be made

$\frac{A - A_\infty}{A_o - A}$ become A'

$$A' = \frac{A - A_\infty \frac{V_\infty}{V_i}}{A_o \frac{V_0}{V_i} - A} \qquad (15)$$

And [X'] becomes

$$[X'] = c_T - c°_M \left[\frac{\frac{V_0}{V_i} - A\infty \frac{V_\infty}{V_i}}{A_o - A_\infty \frac{V_0}{V_i}} \right] \qquad (16)$$

Chapter 1 References

1. Wagner, F.; Bernhauer, K. *Ann. N. Y. Acad. Sci.* **1964**, *112*, 580.

2. Alder, N.; Medwick, T.; Poznanski, T. J. *J. Am. Chem. Soc.* **1966**, *88*, 5018-5020.

3. (a) Pezacka, E.; Green, R.; Jacobsen, D. W. *Biochem. Biophys. Res. Commun.* **1990**, *169*, 443. (b) Pezacka, E. H.; Green, R.; Jacobsen, D. W. *FASEB J.* **1990**, *4*,A2126. (c) Pezacka, E. H.; Jacobson, D. W.; Luce, K.; Green, R. *Biochem. Biophys. Res. Commun.* **1992**, *184*, 832-839. (d) Pezacka, E. H. *Biochim. Biophys. Acta*, **1993**, *1157*, 167-177 and references therein.

4. Jacobsen, D. W.; Lee-Denison, C.; Luce, K.; Green, R. *Fed. Proc*. **1987**, *46*, 1005[1] a) Brasch, N. E.; Hsu, T. C.; Doll, K. M.; Finke, R. G. J. *Inorg. Biochem.***1999**, *76*, 197-209. (b) Suto, R. K.; Brasch, N. E.; Anderson, O. P.; Finke, R. G. *Inorg. Chem.* **2001**, *40*, 2686-2692. (c) L Xia, L; Cregan, A. G. ; L. A. Berben, L. A; Brasch, N. E. . *Inorg. Chem.* **2004**, *43*, 6848-6857.

5. (a) Zhao, R.; Lind, J.; Mere´nyi, G.; Eriksen, T. E. *J. Chem. Soc. Perkin Trans. 2* **1997**, 569 (b) Griffin, O. W. *Free Radical Biol. Med.* **1999**, *27(9-10)*, 922-935.

6. Brown, K. L.; Zou, X.; Savon, S. R.; Jacobsen, D. W. *Biochemistry* **1993**, *32*, 8421.

7. Scheuring, E. M.; Sagi, I.; Chance, M. R. *Biochemistry* **1994**, *33*, 6310.

8. Randaccio, L; Geremia, S; Nardin, G; Slouf, M, Srnova, *Inorg. Chem.* **1999**, *38*, 4087-4092.

9. Hannibal, L.; Smith, S.A.; Jacobsen, D.W. Inorganic Chem. 2010, 49, 9921-9927.

10. Suto, R. K.; Brasch, N. E.; Anderson, O. P.; Finke, R. G. *Inorg. Chem*. **2001**, *40*, 2686.

11. Hsu, T.-L. C.; Brasch, N. E.; Finke, R. G. *Inorg. Chem*. **1998**, *37*, 5109. (b) Brasch, N. E.; Hsu, T.-L. C.; Doll, K. M.; Finke, R. G. *J. Inorg. Biochem.* **1999**, *76*, 197. (c) Suarez-Moreira, E.; Hannibal, L., Smith, C. A., Jacobsen, Brasch, N. E,Dalton Trans. **2006**, 5269-5277.

12. Ngandu, L.; Robin, D.; El Kasmi, A.; Lexa, D. *Inorg. Chim. Acta* **1999**, *292*, 204.

13. Watson, P.; Munter, T.; Golding. B.T. *Chem. Res. Toxxicol*. **2004**, 17, 1562-1567.

14. Zheng, D.; Birke, R. L. *J. Am. Chem. Soc.* **2002**, 124, 9066-9067.

15. (a) Zheng, D.; Birke, R. L. *J. Am. Chem. Soc.* **2001**, 123, 4637-4638. (b) Wolak, M.; Zahl, A.; Schneppenensier, T.; Stochel, G.; van Eldik, R. . *Am. Chem. Soc.* **2001**, 123, 9780-9791.

16. (a) Wheately, C. *J. Nut.Environ. Med.* **2007**, 16,181-211. (b) Wheately, C. *J. Nut.Environ. Med.* **2007**, 16, 212-226.

17. Weinberg, J. B.; Chen, Y.; Jiang, N., Beasley, B. E.; Salerno, J. C.; Ghosh, D. K. *Free Radic. Biol. Med.* **2009**, 46, 1626-1632.

18. (a) Macaddon, A; Davies, G. ; Hudson, P.; andy, S. ; Cattel.H. Int. J. Geriatr Psychiatry. **1998**, 13, 235-239. (b) Clarke, R; Smith,A.D.; Jobst, K.; Refsum, H.; Sutton, L.; Ueland, P. M. *Arch. Neurol.* **1998**, 55, 1449-1455.

19. Macaddon, A; Regland, B.; Hudson, P., Davies, G. Neurology **2002**, 58, 1395-1399.

20. Birch, C. S. ; Brasch, N. E.; McCaddon, A.; Williams, *Free Radic. Biol. Med.* **2009**, 47, 184-188.

21. Firth, R. A.; Hill, H. A. O.; Pratt, J. M.; Williams, R. J. P. ; Jackson, W. R. *Biochemistry* **1967**, 6, 2178-2189

22. Pratt, J. M. *Inorganic Chemistry of Vitamin $B_{12;}$* , Academic Press, London, 1972, Ch 5, pp 44-67.

23. Pratt, J. M. *In Chemistry and Biochemistry of $B_{12;}$* , Banerjee, R. Ed. Wiley, New York, 1999, pp 113-164.

24. Salma, S. ; Spiro, T. G. *J. Raman Spectrosc.* , **1977**, 6, 57-60.

25. Stich, T. A.; Brooks, A. J.; Buan, N. R.; Brunold, T. C. *J. Am. Chem. Soc.* **2003**, 125, 5897-5914.

26. Solomon, E. I.; Gorelsky, S. I.; Dey, A. *J. Comput. Chem.* **2006**, 27, 1415-1428.

27. Day, P. *Theor. Chim. Acta* **1967,** 7, 328

28. Offenhartz, P. O.; Offenhartz, B. H.; Mel Fung, M. J. Am. Chem. Soc. **1970** , 92, 2966-2973.

29. Salem, L.; Eisenstein, O.; Anh, N.T.; Burgu, H.B.; Devaquet, A.; Segal, G.; Veillard, A. Nouv. J. Chim. **1977** , 1, 335.

30. Andruniow, T.; Zagierski, M.Z.; Kozlowski, P.K. J. Phys. Chem. B **2000**, 104, 10921-10927.

31. Andruniow, T.; Zagierski, M.Z.; Kozlowski, P.K. J. Am. Chem. Soc. **2001** 123, 2679-2680.

32. Jensen, P.; Ryde, U. J. Phys. Chem. A **2003** 107, 7539-7545.

33. Selcuki, C.; van Eldik, R.; Clark, T. Inorg. Chem. **2004** , 43, 2828-2833.

34. (a) Dolker, N.; Maseras, F.; Liedos, A. J. Phys. Chem. B **2001** 105, 7564.(b) Dolker, N.; Maseras, F.; Liedos, A. J. Phys. Chem. B **2003** 107, 306-315. (c) Jensen, P.; Ryde, U. J. Mol. Struct. **2002** , 585, 239-255.

35. Andruniow, T.; Zgierski, M.Z.; Kozlowski, P.K. Chem. Phys. Lett. **2000** , 331, 509-512.

36. Jensen, K.P.; Sauer, S.P.A.; Liljefors, T.; Norrby, P-O. Organometallics **2001** 20, 550-556.

37. (a) Andruniow, T.; Zgierski, M.Z.; Kozlowski, P.K. *Chem. Phys. Lett*. **2000 ,** 331, 502-518. (b) Andruniow, T.; Zgierski, M.Z.; Kozlowski, P.K. *J. Phys. Chem. A* **2002** ,106, 1365-1373.

38. Kozlowski, P.K. ; Andruniow, T.; Jarzecki, A. A. ; Zgierski, M.Z.; Spiro, T. G. . *Inorg. Chem*. **2006** , 45, 5585-5590.

39. Stich, T.A.; Buan, N. R.; Brunold, T.C. *J. Am. Chem. Soc.* **2004** ,126, 9735-9749

40. Liptak, M. D.; Fleisschacker, A. S.; Mathews, R. G.; Telser, J. ; Brunold T. C. *J. Phys. Chem. A* **2009** ,113, 5245-5254.

41. Jaworska, M.; Lodowski, P. *J. Mol. Struc. (TheoChem)* **2003** 631, 209-223

42. Jensen, K.P. J.Phys.Chem. B **2005** ,109, 10505-10512.

43. Liptak, M. D.; Brunold, T.C. *J. Am. Chem. Soc*. **2006** ,128, 9144-9156

44. Rovira, C.; Blarnés, X.; Kunc, K. *Inorg. Chem.* **2004** , 43, 6628-6632.

45. Randaccio, L.; Geremia, S.; Stener, M.; Tooffoli, D.; Zangrando, E. Eur. J. Inorg. Chem. **2002** , 93-103.

46. Kurmaev, E. Z.; Moewes, A.; Ouyang, L.; Randaccio, L.; Rulis, P.; Ching, W.Y. *Europhys. Lett.* **2003**, 62, 582-587.

47. Ouyang, L.; .; Randaccio, L.; Rulis, P.; Kurmaev, E. Z.; Moewes, A.; .; Ching, W.Y. *J. Mol. Stuct.* **2003**, 622, 221-227.

48. Ouyang, L.; Rulis, P.; Ching, W.Y.; Nardin, G,; Randaccio, L. *Inorg. Chem.* **2004** , 43, 1235-1241.

49. Andrunoiw; T; Koslowski, P. W. ; Zgierski *J. Chem. Phys.* ***2001***, 115 , 7522-7533.

50. Brooks, A. J.; Valsie, N. R.;Banerjee, R., Brunold, T. C. *J. Am. Chem. Soc.* **2004**, 126, 8167-8180.

51. Andrunoiw; T; Jaworska, M.; Lodowski, P ;; Zgierski, M. Z.; Dreos, R; Randaccio, L. ; Koslowski, P. W. *J. Chem. Phys.* **2008**, 129 , 085101-1-14.

52. Lodowski, P; Jaworska, M; Andrunoiw; T; Kumar, M.; Koslowski, P. W. *J. Phys. Chem. B* ***200*9**, 113 , 6898-6909.

Chapter 2 References

1. Gaussian 03, Revision C.02, M.J. Frisch, G.W. Trucks, H.B. Schlegel, G.E. Scuseria, M.A. Robb, J.R. Cheeseman, J.A. Montgomery Jr., T. Vreven, K.N. Kudin, J.C. Burant, J.M. Millam, S.S. Iyengar, J. Tomasi, V. Barone, B. Mennucci, M. Cossi, G. Scalmani, N. Rega, G.A. Petersson, H. Nakatsuji, M. Hada, M. Ehara, K. Toyota, R. Fukuda, J. Hasegawa, M. Ishida, T. Nakajima, Y. Honda, O. Kitao, H. Nakai, M. Klene, X. Li, J.E. Knox, H.P. Hratchian, J.B. Cross, V. Bakken, C. Adamo, J. Jaramillo, R. Gomperts, R.E. Stratmann, O. Yazyev, Austin, R. Cammi, C. Pomelli, J.W. Ochterski, P.Y. Ayala, K. Morokuma, G.A. Voth, P. Salvador, J.J. Dannenberg; V.G. Zakrzewski, S.

Dapprich, A.D. Daniels, M.C. Strain, O. Farkas, D.K. Malick, A.D. Rabuck, K. Raghavachari, J.B. Foresman, J.V. Ortiz, Q. Cui, A.G. Baboul, S. Clifford, J. Cioslowski, B.B. Stefanov, G. Liu, A. Liashenko, P. Piskorz, I. Komaromi, R.L. Martin, D.J. Fox, T. Keith, M.A. Al-Laham, C.Y. Peng, A. Nanayakkara, M. Challacombe, P.M.W. Gill, B. Johnson, W. Chen, M.W. Wong, C. Gonzalez, J.A. Pople. Gaussian, Inc., Wallingford CT, **2004**.

2. Gaussian 09, Revision **A.1**, Frisch, M. J.; Trucks, G. W.; Schlegel, H. B.; Scuseria, G. E.; Robb, M. A.; Cheeseman, J. R.; Scalmani, G.; Barone, V.; Mennucci, B.; Petersson, G. A.; Nakatsuji, H.; Caricato, M.; Li, X.; Hratchian, H. P.; Izmaylov, A. F.; Bloino, J.; Zheng, G.; Sonnenberg, J. L.; Hada, M.; Ehara, M.; Toyota, K.; Fukuda, R.; Hasegawa, J.; Ishida, M.; Nakajima, T.; Honda, Y.; Kitao, O.; Nakai, H.; Vreven, T.; Montgomery, Jr., J. A.; Peralta, J. E.; Ogliaro, F.; Bearpark, M.; Heyd, J. J.; Brothers, E.; Kudin, K. N.; Staroverov, V. N.; Kobayashi, R.; Normand, J.; Raghavachari, K.; Rendell, A.; Burant, J. C.; Iyengar, S. S.; Tomasi, J.; Cossi, M.; Rega, N.; Millam, N. J.; Klene, M.; Knox, J. E.; Cross, J. B.; Bakken, V.; Adamo, C.; Jaramillo, J.; Gomperts, R.; Stratmann, R. E.; Yazyev, O.; Austin, A. J.; Cammi, R.; Pomelli, C.; Ochterski, J. W.; Martin, R. L.; Morokuma, K.; Zakrzewski, V. G.; Voth, G. A.; Salvador, P.; Dannenberg, J. J.; Dapprich, S.; Daniels, A. D.; Farkas, Ö.; Foresman, J. B.; Ortiz, J. V.; Cioslowski, J.; Fox, D. J. Gaussian, Inc., Wallingford CT, 2009.

3. Tomasi, J.; Mennucci, B. .. Cammi, R. *Chem. Rev.*, **2005** 105 , 2999-3093.

4. Hay, P. J.; Wadt, W. R. *J. Chem. Phys.* **1984** , 82, 299

5. Becke, A. D. *J. Chem. Phys.* **1993** , 98, 5648.

6. Stephens, P. J. ; Devlin, F. J. ; Chabalowski, C. F. ; Frisch, M. J. *J. Phys. Chem.* **1994** , 98, 11623.

7. Becke, A. D. *Phys. Rev. A* **1988** , 38, 3098-3100

8. Perdew, J. P. *Phys. Rev. B* **1986** , 33, 8822-8824.

9. Gorelsky, S. I., AOMIX version 6,46; Department of Chemistry, York University; Toronto, ON, 2009; http:/www.sg-chem.net.

10. Rabenstein, D. L., *J. Am. Chem. Soc.* **1973**, 95 2797-2803.

11. Hannibal, L.; Smith, S.A.; Jacobsen, D.W. *Inorganic Chem*. **2010**, 49, 9921-9927.

12. Suto, R. K.; Brasch, N. E.; Anderson, O. P.; Finke, R. G. *Inorg. Chem*. **2001**, *40*, 2686.

13. Scheuring, E. M.; Sagi, I.; Chance, M. R. *Biochemistry* **1994**, *33*, 6310.

14. Brown, K. L., *Chem. Rev*. **2005**, 105, 2075-.

15. Randaccio, L. ; Geremia, S.; Nardin, G. ; Wurerges, J. *Coord. Chem. Rev*. 2006, 250, 1332-1350.

16. Solomon, E. I.; Gorelsky, S. I.; Dey, A. *J. Comput. Chem.* **2006**, 27, 1415-1428.

17. Brooks, A. J.; Valsie, N. R.;Banerjee, R., Brunold, T. C. *J. Am. Chem. Soc.* **2004**, 126, 8167-8180.

18. Kratky, C.; Färber, G.; Gruber, K; Wilson, K; Dauter, Z.; Nolting, H-F; Konrat, R., and Kräutler, B. *J.AmChem. Soc*. **1995**, 117, 4654-4670.

19. (a) Rossi, M.; Glusker, J.; Randaccio, L.; Summers, M.; Toscano, P.; Marzilli, J. *J. Am. Chem. Soc*. **1985**, 107, 1729-1738. (b) Luciana Hannibal, Clyde A. Smith, Jessica A. Smith, Armend Axhemi, Abby Miller, Sihe Wang, Nicola E. Brasch, and Donald W. Jacobsen, Inorg.Chem. **2009**, 48, 6615-6622.

20. Dapprich, S.; Frenking, G. *J. Phys. Chem.* **1995** , 99, 9352-9362.

21. Frenking, G; Fröhlich, N. *Chem. Rev.* 2000, 100, 717-774.

22. Gorelsky. S. I.; Ghosh, S.;Solomon, E. I. *J. Am. Chem. Soc.* **2006**, 128, 278-290.

23. Kitaura, K.; Morokuma, K . *Int. J. Quantum Chem.* **1976**, 10, 325-340.

24. Ziegler, T; Rauk, A *Theoret. Chim. Acta,* **1977,** 46 1-10.

25. Mayer, I. *Chem. Phys. Lett.* **1983**, 97, 270-274.

26. NBO 5.9. E. D. Glendening, J. K. Badenhoop, A. E. Reed,J. E. Carpenter, J. A. Bohmann, C. M. Morales, and F. Weinhold(Theoretical Chemistry Institute, University of Wisconsin, Madison, WI, 2009)

27. Weinhold, F.; Landis, C. *Valency and Bonding:A Natural Bond Orbital Donor-Acceptor Perspctive* , Cambridge Univ. Press, Cambridge, 2005

28. Reed, A. E.; Curtiss, L. A. ; Weinhold, F. *Chem. Rev.* **1988**, 88, 899-926.

29. Ballhausen, C. J. ; Gray, H. B. *Inorg. Chem.* **1962** , 1, 111-122.

30. Wiberg, K. B. *Tetrahedron* **1968**, 24, 1083.

Chapter 3 References

1. M. E. Casida, in *Recent Advances in Density Functional Methods*, edited by D. P. Chong,

(World Scientific Pub. Co., Singapore ,1995) Part I, Ch. 5, 155.

2. Hay, P. J.; Wadt, W. R. *J. Chem. Phys.* **1984** , 82, 299

3. Becke, A. D. *J. Chem. Phys.* **1993** , 98, 5648.

4. Stephens, P. J. ; Devlin, F. J. ; Chabalowski, C. F. ; Frisch, M. J. *J. Phys. Chem.* **1994** , 98, 11623.

5. Becke, A. D. *Phys. Rev. A* **1988** , 38, 3098-3100

6. Perdew, J. P. *Phys. Rev. B* **1986** , 33, 8822-8824.

7. Martin, R. L. *J. Chem. Phys*. **2003** , 118, 4775.

8. Stich, T. A.; Brooks, A. J.; Buan, N. R.; Brunold, T. C. *J. Am. Chem. Soc.* **2003**, 125, 5897-5914.

9. Lever. A. P. B. *Inorganic Electronic Spectroscopy* , 2nd. ed. ; Elsevier:Amsterdam/New York, 1984.

10. Stich, T. A.; Brooks, A. J.; Buan, N. R.; Brunold, T. C. *J. Am. Chem. Soc.* **2003**, 125, 5897-5914.

11. Polavarapu, P. *J. Phys. Chem. A* **2005** ,109, 7013-7023.

12. Varsano, D; Espinosa-Leal,L. A,; Anfrade, X.; Marques, M. A. L., de Felice, R,; Rubio, A. *Phys. Chem. Chem. Phys.* **2009** , 11, 4481-4489.

13. Hannibal, L.; Smith, S.A.; Jacobsen, D.W. *Inorganic Chem*. **2010**, 49, 9921-9927.

Chapter 4 References

1. Diehl, H. ; Haar, R. W. V. ; Sealock, R. R. *J Am. Chem. Soc.* **1950,** 72, 5312.

2. Hogenkamp, H. P. C. ; Holmes, *Biochemistry*, 1970, 9, 1886.

3. Birke, R. L. ; Brydon, G. ; Boyle, M. F. *J. Electroanal. Chem.* **1974,** 52, 237.

4. Amatore, C. ; Lexa, D ; Saveant, J. M. *J. Electroanal. Chem.* **1980,** 111, 81.

5. Lexa, D. Savent, J. M. *J. Am. Chem. Soc.* **1978,** 100, 3220.

6. Lexa, D. ;Saveant, J. M. ; Zickler, *J. Am. Chem. Soc.* **1980,** 102, 2654.

7. P. G. Swetik, J. W. I., *J. Electroanal. Chem.* **1974,** 51, 433.

8. Lexa , D. ; Savent, J. M. *Acc. Chem. Res.* , **1983**, 16 , 235.

9. Halpern, J. in "*B_{12} : Chemistry*" ,Vol.1. ,ed. D. Dolphin, Wiley, NY,1982, p. 513

10. Kenyhercz, T. M. ; Deangelis, T. P. ; Norris, B. J. ; Heineman, W. R. ; Mark, H. B. *J. Am. Chem. Soc.* **1976,** 98, 2469.

11. Lexa, D. Savent, J. M. *J. Am. Chem. Soc.* **1976,** 98, 2652

12. Lexa, D. ;Saveant, J. M. ; Zickler, *J. Am. Chem. Soc.* **1977,** 99, 2786.

13. de Tocconi, N ; Lexa, D. Savent, J. M. *J. Am. Chem. Soc.* **1979,** 101, 467.

14. Saveant J. M. ; de Tocconi, N. in "Vitamin B_{12} " eds. Zugalak and Friedrich, de Gruter,Berlin,1979, p.203

15. Zheng, D.; Lu , T. *J. Electroanal. Chem.* **1997**, 429, 61-65

16. Ngandu,L, Robin,D.; El Kasmi, A. ;Lexa, D. Inorg. Chim. Acta **1999, 204-212.**

17. Kim, M.-H. ; Birke , R. L. *J. Electroanal. Chem.* **1983** , 144, 331.

18. Martin, B. D ; Finke, R. G. *J. Amer. Chem. Soc*. 1**990**, 112 , 2419.

19. Finke R. G. ;. Martin, B. D. *J. Inorganic Biochem*. **1990**, 40, 19 .

20. Martin, B. D. Finke, ; R. G. *J. Amer. Chem. Soc*. **1990** , 114 , 585.

21. Birke, R. L.; Huang Q-D.; Spataru, T., Gosser Jr., D. K. *J. Amer. Chem. Soc*. **2006**, 128, 1922-1296.

22. Spataru, T; Birke, R. L. *J. Electroanal. Chem* **2006** , 593, 74-86.

23. Spataru, T; Birke, R. L. *J. Phys. Chem. A* , 2006, 110, 8599-8604.

24. Zho, D.-L ; Tinembart, O.; Scheffold, R.; Walder, L. *Helv. Chim. Acta*., **1990,** 73, 1469.

25. Birke, R. L .; Yau, J.; Kim, M.-H. . *Anal. Chem*., **1984** 56 , 1716.

26. Blackurn, R. ; Kyam, M.; Swallow, A. J. *J. Chem. Soc. Faraday Trans.* I,73, 250(1977)

27. Balasubramanian, P. N. ; Reed, J. W; Gould, E. S. *Inorg. Chem*.**1985** , 24 ,1794.

28. Balasubramanian, P. N. ; Gould, E. S. *Inorg. Chem*.**1984** , 23 , 825

29. J. Zagal, M. Paez, C. Paez, J. Electroanal. Chem., 237: 145, 1987.

30. J. Zagal, J. Sturm, Bol. Soc. Chil. Quim., 31: 103, 1986.

31. C. Paez, A. Prelle, J. Zagal. Bol. Soc. Chil. Quim., 35: 299, 1990

32. J. H. Zagal, M. J. Aguirre, C. G. Paroli, J. Electroanal. Chem., 374: 215, 1994.

33. Gosser, D., (1993). Cyclic voltammetry: Simulation and Analysis of Reaction Mechanisms. VCH, N.Y

35. Hsu, T.-L. C.; Brasch, N. E.; Finke, R. G. *Inorg. Chem*. **1998**, *37*, 5109.

36. Rabenstein, D. L. *J. Am. Chem. Soc*. **1973**, 2797-2803.